

NOVEL PHENOMENA IN OXIDE HETEROSTRUCTURES

By

SANJUKTA PAUL

PHYS05201204021

Saha Institute of Nuclear Physics, Kolkata

A thesis submitted to the

Board of Studies in Physical Sciences

In partial fulfillment of requirements

For the Degree of

DOCTOR OF PHILOSOPHY

of

HOMI BHABHA NATIONAL INSTITUTE

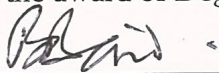
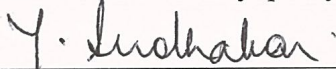
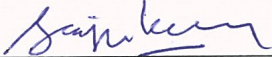
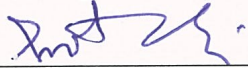
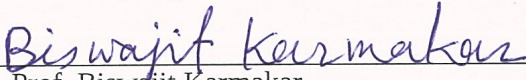


July, 2018

Homi Bhabha National Institute

Recommendations of the Viva Voce Committee

As members of the Viva Voce Committee, we certify that we have read the dissertation prepared by Sanjukta Paul entitled "Novel phenomena in oxide heterostructures" and recommend that it may be accepted as fulfilling the thesis requirement for the award of Degree of Doctor of Philosophy.

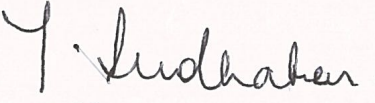
	02/11/2018
Chairman - Prof. Bilwadal Bandyopadhyay	Date:
	02/Nov/18
Guide / Convener - Prof. Sudhakar Yarlagadda	Date:
	2/11/2018
Examiner - Prof. Sanjeev Kumar	Date:
	02/11/2018
Member 1- Prof. Pradeep Kumar Mohanty	Date:
	02/11/2018
Member 2- Prof. Biswajit Karmakar	Date:

Final approval and acceptance of this thesis is contingent upon the candidate's submission of the final copies of the thesis to HBNI.

I hereby certify that I have read this thesis prepared under my direction and recommend that it may be accepted as fulfilling the thesis requirement.

Date: 2/Nov/18

Place: Kolkata


Guide

STATEMENT BY AUTHOR

This dissertation has been submitted in partial fulfillment of requirements for an advanced degree at Homi Bhabha National Institute (HBNI) and is deposited in the Library to be made available to borrowers under rules of the HBNI.

Brief quotations from this dissertation are allowable without special permission, provided that accurate acknowledgement of source is made. Requests for permission for extended quotation from or reproduction of this manuscript in whole or in part may be granted by the Competent Authority of HBNI when in his or her judgment the proposed use of the material is in the interests of scholarship. In all other instances, however, permission must be obtained from the author.

Sanjukta Paul

DECLARATION

I, hereby declare that the investigation presented in the thesis has been carried out by me. The work is original and has not been submitted earlier as a whole or in part for a degree / diploma at this or any other Institution / University.

Sanjukta Paul

LIST OF PUBLICATIONS ARISING FROM THE THESIS

Journal:

1. “Giant magnetoelectric effect in pure manganite-manganite heterostructures”
Sanjukta Paul, Ravindra Pankaj, Sudhakar Yarlagadda, Pinaki Majumdar, Peter B.
Littlewood.
[PhysRevB. 96, 195130 \(2017\).](#)
2. “Study of the ferromagnetic-insulator phase in manganites”
Sanjukta Paul, Sudhakar Yarlagadda.
[arXiv:1805.05172 \[cond-mat.str-el\].](#)

Sanjukta Paul

DEDICATION

To

Ma and Baba

for your incessant love and sacrifice in making me what I am!

and

Thappa, Dida and Dadu for all the values you have inculcated in me.

ACKNOWLEDGEMENTS

When it comes to acknowledgements you never know whether it is a beginning or the journey to another beginning! Please bear with me if I pour my heart out and you are absolutely welcome to skip this part! Choosing to look back at this moment, to relive the days of my first acquaintance with physics, I feel I get transported to a wonderland in school. On a lighter note, I remember how the image of a star or a nebula perked me up or how it left me clueless that the principle behind a magnet sticking to my iron almirah could be explained by this mysterious subject “physics”! These created an awe in me and allured me towards its diverse characters. After one and a half decades, here I am, still trying to make sense out of its miscellany and trying to sum up a little of what I could fathom. So above anything else, I am grateful to physics for being such a delightful companion for a large part of my life.

My journey as a Ph.D student started in 2012, when I knew nothing about research work. I am thankful to my supervisor Prof. Sudhakar Yarlagadda for introducing me to this vibrant field of oxides and for all those numerous discussions that gave me an insight into this field. Additionally, I have slowly learnt from him the importance of rechecking every minute detail of an accomplishment irrespective of whether it is a manuscript, the content of a mail or a simple official form, to help things get done in one go. For the next part, I was fortunate to work with not only a good scientist, but an extremely good human being- Prof. Pinaki Majumdar. My visits to HRI helped me strengthen my numerical simulation capabilities as even short discussions with him were greatly productive and easy-going. My work has also been enriched with valuable comments and constructive criticisms from my collaborator Prof. Peter B. Littlewood. Though a little later, I had the opportunity to

work with one of the finest people I have ever met, Prof. Bikas K. Chakrabarti. Within a few months of association with him, I learnt a lot from his vision towards free-minded, collaborative work; his smart ways of dealing with any kind of result and his believing in my efforts even when I had empty hands. I acknowledge the help from Prof. Kalpataru Pradhan and Prof. P.K. Mohanty for answering the simplest of my questions whenever I reached out to them. I would also like to thank Prof. Biladwal Bandyopadhyay and Prof. Biswajit Karmakar, my doctoral committee members other than P.K. sir for helping me in the renewals with their remarks. I thank Prof. Arti Garg for often motivating me to present my work outside and get an exposure. Most importantly, during the last few months, without the helping hand of Prof. Debades Bandyopadhyay it would have been impossible for me to submit my thesis on time.

Although inspirations and formal experiences do have a great impact on you, Ph.D is never like the abstract of a paper. It is a long process in which your peers, some of whom turn out to be life-long friends, live the highs and lows with you, sometimes run and most of the times stagger to make the way out and then suddenly grow up to face life! Three such people have been Sabyasachi da, Sudip and Amrita. Sabya da has been like a pivot in room 445 where he would academically pamper the other four people to such an extent that we stopped searching things on internet or books for clarification! Like a born teacher he has this out-of-the-world capability of explaining with utmost care, basic physics, advanced physics, simulations, computer terminal commands, building innovative and effective script files and whatever more one can think of as part of a Ph.D life! Apart from this, he has created in me a knack for keeping track of UFO news! I have had discussions with Sudip on very many different areas of physics and he would always end up educating me a little more about what more can be done, how to dream bigger and put your 200 % in your work, come what may. I will always remember the days when he constantly

motivated me and offered to collaborate with me at a point when I thought I was capable of doing little. I wish our travelling spree that has begun in 2014 continues for years and we explore more of India on our own. My discussions with Amrita began in Post-MSc. coursework itself, where I appreciated and closely observed her analytical skills and the art of making short notes out of any physics stuff. Most importantly, the bouts of laughter we had in 445 because of Sabya da, Sudip and Sourav da (for their incredible qualities of sharing silly jokes) will be a source of amusement for me forever!

MSA-II, my hostel can as well be used as a synonym for my Ph.D. period. It has been like a home away from home for me. From an impressionable age when I entered it to this date when I may be leaving sometime soon, the boarders have been witness to all my good and bad times. I fondly remember the cooks Shyamal kaku, Biswajit and Haran da for being so kind to me throughout, knowing my likes and dislikes very much like my mother and specially preparing food for me even at odd hours of the day. I am thankful to many other people like the security stuff Moloy da, Mandi da, Bahadur da and cleaning staff Birju da for all their kindness. I had some very good seniors like Sudip da, Nilu da, Rajani da, Atanu da and Biswanath da with whom I have interacted a lot and who have been a part of all the joyous Saraswati Puja, picnic, Holi, new year and birthday celebrations we had as mess members. Ravindra da, my group member, senior and collaborator has been that soulful person who always came up with solutions for my academic, personal as well as health problems. I am also grateful to our canteen stuff Nimai da, Nobo da and Pintu for their generosity. Coming to seniors who were not boarders of my hostel, I must say Aminul da has been very supportive in helping me with information about SINP just after my selection. I was lucky to have Soumyo da, Amit da, Arnab da, Atanu da, Souvik Priyam da, Dipankar da, Arijit da, Bijoy da and Gourab da as other seniors most of who formed a part of the once vibrant condensed matter physics division. Our system administrator

Kausik da has become one such senior, who has helped me fix anything and everything related to job submissions and computers. My bond with him turned out to be very special as his attachment with literature, his passion for reading books and his love for travel - everything was in sync with mine. I will cherish all the enlightening discussions with him and his advices to me in times of distress. Juniors have always been very loving to me and at times they have even showered on me the sibling-love I could never enjoy. Dipak and Aranya have been two such people, who, irrespective of whether I cared for them and whether I was unmindful of their help, have constantly been through my struggles and pushed me out of every little setback, as brothers would do! Bithika has always been that funny girl who always manages to revamp my mood with her humour. I fondly remember conversations with Mugdha, Amit, Susmita, Sukannya, Arghya, Suchismita and Rajkamal. From the toddler-batch, I grew very close to Upala for her simplicity and Promita, Rashika, Subhi and Anindita for their engaging attitude.

From the cake, slowly coming to the cream I do not think I can ever finish writing about my batchmates. It was a roller coaster ride with night-long birthday parties, picnics, random adda sessions, short trips, long tours, get-togethers, marriage functions, movie watching, food hunting, boatrides in the Princep Ghat and even iilish gulping sessions in our hostel! We had a bunch of insane people who believed in enjoying collectively and in the most mundane Bengali way. I will remember Suvankar for his protectiveness, programming skills and all his timely help; Binita for her questions and her cooking; Mily for her “u” ending self-generated words; Kumar for his perfectionist attitude and his love for ghosts; Kuntal Nayek for his passion for history; Kuntal Mondal for his delta phase moods; Sanjib for his “torey”; Achyut and Pankaj for being stand up comedians; Sabuj for his knowledge and relentless lectures; Ashim for his tour managing and badminton skills; Tapas for his flamboyance; Naosad for his childish smile; Anshu for his love for

astrophysics; Sukanta for his endless collection of movies ; Sayanee for her dance moves; Debajyoti for his jaw dropping stunts; Gouranga for his uber sense of humour and Satyajit for his calmness, to name a few and not all.

The three gems I left out would form a part of that intense phase of life in which I smiled, cried my heart out, shared the deepest of my secrets unabashedly and literally outgrew the primitiveness in me- Chiru, Tirtha and Aritra. I have learnt to look at life through various angles with Chiru's guidance, learnt to be liberal-minded and developed greater passion for literature being in touch with Tirtha and have gained insurmountable energy and positivity being close to Aritra. I have had my share of fights and heated debates with them but soon they melted into thin air and I realized that my love for them would always remain unfazed.

Aritra has been that crazy guy who has broken me up into pieces and then rebuilt the whole of it with his care. He has made me a much happier person by focussing my mind to the diversity life can offer - from listening to good music, watching world class cinema, handcrafting, relishing a football match and above all taking matters a little less seriously! I have always adored the unconventional ways in which he deals with problems and he has helped me adopt the same. He has even made valuable suggestions regarding this thesis.

Jadavpur University days are extremely close to my heart. I loved the place, loved the ambience and first started my life in a big city, staying away from home. I will fondly remember the love and care I received from Prof. Tapas Ranjan Middy, Prof. Sujata Tarafder, Prof. Sanjay Kumar and Prof. Golam Mostafa. I will always admire my friend Sukhi for her intelligence and simplicity and for the beautiful relationship we nurtured. Mampee, Papiya, Trisha and Bony - life would be incomplete with all the fun I had with you in my first ever mess-life.

There are people who cannot be accommodated in a single time frame. From a vul-

nerable lump of emotions to a far more matured and honest mind, Sutirtha has almost single-handedly shaped my character. He has been this infinite source of inspiration for me that has made me come back to the fore a million times when I thought I had already lost the battle. Right from my college days till the end of my Ph.D, he has been that one friend who would always find ways to make me smile even when everyone else turned their back. He has helped me with physics, with numerical ideas, with logic, with ways to deal with depression and health problems, infused in me love for food, love for street walks in Kolkata and most importantly provided me with a philosophy in life that nobody else could.

My days in college, though not very cheerful, have memories infested with friends like Swayam, Azhar, Ankita, Anita, Arpita and Yasin. Swayam has been that friend who would tolerate all my whims and talk to me as if we are always in touch. If there was a turning point in my life, it had to be Prof. Debasish Bhattacharyya's strong influence, being my physics tutor. DB sir has the brilliance in teaching the finer nuances of physics with ease and has always encouraged me to aim for learning more.

I have gradually come back to where I began, the best days of my life - in school! Mr. Kaushik Chakrabarty, my physics teacher first instilled in me the passion for physics. I am thankful to Sir Pushpenjit Bose for giving me an excellent training in computer programming that proved to be my bread and butter after so many years. I have always been that fangirl who would follow Mrs. Majilya, my english teacher for her unbelievable hold over the subject and her chiseled language skills. I would like to thank Anupam da, Mousom da, Nupur sir, Soumen Sir and Ratul sir for teaching me my subjects with all their patience. I cannot judiciously name all my friends, so dear to me, but I was lucky to have a life-long friend - Mousim. I know her for twenty years and she has been that same loving soul I have always known. We talk for hours even though we meet once in a year and she has always

been that well-wisher who would praise me even for my faults! I hope our exchange of books and letters continues for years to come, as they mean a lot to me.

Finally closing in, after all these accolades and achievements, I feel my family is what I truly have and possess. My parents have given me a life that they never enjoyed, have pushed me to limits they had deliberately sacrificed for me and mostly have lived their lives through my happiness and sorrows. It was predominantly my mother's dream and her unimaginable support and sacrifice to take me to a place where I stand today. My father has been that person who would always be content with whatever little I could achieve and shower his love on me. Life has never been the same for me after dealing with the greatest loss, my grandmother, "Thappa", as I would endearingly call her. She had been the second mother for me. She would go to any lengths for my well being and it was she who imbibed in me the love for old-world architecture, books, old movies and songs. Dida was the epitome of love and had constantly pampered me even in my twenties. Dadu, with his immense knowledge and wisdom, was my first teacher after my mother and was very affectionate to me. Apart from this core, I have an extended family of Babu, my little nephew who I absolutely love, Rini my cousin who has laughed with me on every silly thing on this earth, Tutul and Baban dada for being the good cousins, Bhadu didi, Budhan, Munni di and Mala masi who have almost become family members at various stages of my life.

Last but not the least, all the books in my shelf - you keep me alive!

Sanjukta Paul.

CONTENTS

Synopsis	ix
List of Figures	x
1 Introduction	1
1.1 Strongly correlated oxides	2
1.2 Superlattices, thin films and heterostructures of oxides	3
1.3 Introduction to manganites	8
1.4 Review of manganites	11
1.4.1 Crystal Structure	11
1.4.2 Tolerance factor	11
1.4.3 Crystal field splitting	13
1.4.4 The different degrees of freedom	15
1.4.4.1 Charge	15
1.4.4.2 Spin	15
1.4.4.3 Orbitals	15
1.5 Magnetic interactions	17

CONTENTS

1.5.1	Double exchange	18
1.5.2	Superexchange	21
1.6	Coulomb interaction	23
1.7	Electron-phonon interaction	26
1.8	Manganite phase diagram	28
1.8.1	Insulating A-AFM	29
1.8.2	Canted AFM	30
1.8.3	Ferromagnetic insulator	31
1.8.4	Ferromagnetic metallic region	31
1.8.5	A-AFM metal	32
1.8.6	C-AFM insulator	34
1.8.7	G-AFM insulator phase	34
1.9	Plan of the thesis	34
2	Magnetoelectric effect in pure manganite-manganite heterostructures	35
2.1	Introduction	35
2.2	General arguments for magnetoelectric effect in manganite heterostructures	39
2.3	Analytic treatment	42
2.3.1	Polaronic Hamiltonian	42
2.3.2	Charge Profile	45
2.3.3	Magnetization distribution	50
2.3.3.1	CMO side	51
2.3.3.2	LMO side	53
2.4	Numerical Approach	55
2.4.1	Model Hamiltonian	55

CONTENTS

2.4.2	Calculation procedure	58
2.4.3	Results and discussion	61
2.4.3.1	No electron-phonon interaction and $E_{\text{ext}} = 400 \text{ kV/cm}$	62
2.4.3.2	Symmetric 12×8 lattice with $g = 2.0$ and $E_{\text{ext}} = 300 \text{ kV/cm}$	65
2.4.3.3	Symmetric 12×8 lattice with $g = 2.2$ and $E_{\text{ext}} = 0$	68
2.4.3.4	Symmetric 12×6 lattice with $g = 2.2$ and $E_{\text{ext}} = 400 \text{ kV/cm}$	69
2.4.3.5	Asymmetric 12×8 system of 2 LMO layers and 6 CMO layers with $g = 2.0$ and $E_{\text{ext}} = 300 \text{ kV/cm}$	74
2.4.3.6	Asymmetric 12×8 system of 6 LMO layers and 2 CMO layers with $g = 2.0$ and $E_{\text{ext}} = 300 \text{ kV/cm}$	75
2.5	Conclusions	78
3	Study of the ferromagnetic-insulator phase in manganites	81
3.1	Introduction	81
3.2	Effective Hamiltonian	84
3.2.1	Three NN sites of the intermediate site are filled by electrons.	89
3.2.2	Any two of NN sites of the intermediate site is filled.	91
3.2.3	Any one of NN sites of the intermediate site has an electron.	93
3.2.4	All the NN sites of the intermediate site have holes.	94
3.3	Calculation procedure	96
3.4	Results and discussion	99
3.4.1	A-AFM background	99
3.4.1.1	$t=0.3 \text{ eV}$ case	102
3.4.1.2	$t=0.2 \text{ eV}$ case	103
3.4.2	G-AFM background, $t = 0.3 \text{ eV}$ case	105

CONTENTS

3.4.3 Fully FM background, $t = 0.3$ eV	106
3.5 Conclusions and perspectives	108
4 Summary	110
Bibliography	113

SYNOPSIS

Though the last few decades have witnessed a tremendous success for the semiconductor technology [1], yet oxides may be better poised than semiconductors to address the future technological challenges. The reasons for this are as diverse as the oxides being better suited for miniaturization of electronic devices, improvement of memory devices, dissipationless operation, data and energy storages, etc. [2–8]. Furthermore, oxides manifest more complex and richer phase diagrams, exhibit a wider range of phenomena such as superconductivity, charge-density-waves, spin-density-waves, orbital-density-waves, colossal magnetoresistance, multiferroicity, etc. [6, 9, 10]; these require a deeper understanding of the fundamentals of condensed matter physics. Low-dimensional oxides specifically present new opportunity where electronic, magnetic, orbital, and lattice properties can be optimized by engineering many-body interactions, geometries, fields, strain, disorder, etc. It is true that semiconductors can be fabricated into complex structures and modelling them is relatively easy and straightforward. On the other hand, the material chemistry for oxides is challenging and, although state-of-the-art fabrication techniques are slowly evolving, the overall development is still lagging behind that of the semiconductors. The tunability is however very high for oxides due to competing, close-in-energy, ordered phases; for

semiconductors tunability can only be moderately achieved by doping or electric fields. Miniaturization can be achieved in oxide devices because wave functions of charged particles are confined within few angstroms; whereas for semiconductors, wave functions are far more extended. Thus, to explore new physics and functionalities and also to put them to use, the field of oxides provides rich avenues of research, both for experimental and theoretical condensed matter physics.

Systems that are strongly correlated often exhibit properties that do not fit into the conventional band theoretic predictions. The reason behind this is attributed to the strong Coulomb repulsions (electron-electron) present in such systems, much higher in magnitude to the kinetic energy of the free electrons, leading to insulating properties in an otherwise metallic system. Such insulators are termed Mott insulators or Mott-Hubbard insulators since in the simplest possible way, the system is described by the non-degenerate Hubbard model [11–13]. The Mott insulators have characteristic features of electron localization, with one electron per site, if the electron density is 1 (i.e, we have a half-filled band). Thus, if we start with electrons that are non-interacting, i.e., a fully metallic system, and slowly increase the ratio of the electron-electron repulsion to the kinetic energy of the system, we should observe a metal-insulator transition called the Mott-transition. There exist many transition metals that exhibit Mott transition with partially filled d orbitals in place of a single electron per site for conventional Mott insulators. Along with these transitions there is change in crystal structure and magnetic ordering in the system. Regarding magnetic ordering, appearance of localized electrons immediately implies there must be localized spins or magnetic moments in the system. For a partially filled system of d orbitals in a transition metal (TM) and for strong Coulomb repulsions, it is well known that the ground state of such a Mott insulator is antiferromagnetic. Doping the Mott insulators essentially introduces strong interactions between the doped minority carriers and the background spin

configuration. Depending on the doping concentration, there can be a plethora of magnetic phases, namely, ferromagnetic state, various types of antiferromagnetic (AFM) order (such as A-type, C-type, CE-type, G-type, etc.), canted antiferromagnetic phase, ferromagnetic droplets in an antiferromagnetic background, phase separated states, etc. From isolated TM ions, moving over to TM ions placed in a crystal, we have bands for different d orbitals coming into the picture. Thus not only correlations for the charges and the spins but also the correlations for the orbitals starts to play a role. For large number of d electrons, we may end up having itinerant e_g electrons besides localized t_{2g} electrons in the system while filling various energy levels.

However, we generally deal with compounds of TM elements, such as oxides, halogenides, etc., which are Mott insulators but have a rich physics involved with them [14]. For undoped oxides or halogenides, we have hybridization between d electrons of TM and s or p electrons of the oxygen or halogen ion called the ligand ion. Depending on the orbital overlap, we may have either antiferromagnetic or ferromagnetic interactions between the spins, via oxygen atoms, termed the superexchange interaction. A doped Mott insulator, on the other hand, shows coupling of localized and itinerant electrons (due to large Hund's coupling) leading to double exchange interaction. Thus in TM oxides, which is broadly the topic of interest in this thesis, there is a very close interplay between the charge, spin and orbital degrees of freedom. In many oxides, a fourth degree of freedom called the lattice degree of freedom is also important in explaining the rich phase diagrams that they showcase. Oxides of the type ABO_3 showing a perovskite crystal structure have adjacent BO_6 octahedra that share oxygen atoms. Here 'A' represents a rare-earth ion and 'B' a TM ion. These octahedra undergo cooperative octahedral distortions that bring about strong electron-lattice interactions in the system. Apart from large electron-electron repulsions in strongly correlated systems, these cooperative electron-phonon interactions are closely in-

terlinked with the charge, spin, and orbital degrees of freedom and explain many emergent phenomena displayed by oxides.

Focusing specifically on manganites [15–18] in the oxide family, which show unique magnetic phase diagrams, we try to explore in this thesis novel phenomena associated with manganite heterostructures which do not have a counterpart in the already intriguing bulk systems. Although enough work has been done on bulk doped manganites [19], interface physics generated from heterostructures of two parent oxides has still much to offer, both for fundamental understanding as well as for technological advancement. There has been an upsurge of interest, both experimentally [20–27] as well as theoretically [28–33], in understanding novel aspects of conductivity, magnetism, ferroelectricity, and orbital order in pure manganite-manganite $\text{TMnO}_3/\text{DMnO}_3$ heterostructures where T refers to trivalent rare earth elements La, Pr, Nd, etc. and D refers to divalent alkaline elements Sr, Ca, etc. At low temperatures, the bulk TMnO_3 is an insulating A-type antiferromagnet (A-AFM); on the other hand, the bulk DMnO_3 is an insulating G-type antiferromagnet (G-AFM). Furthermore, the doped alloy $\text{T}_{1-x}\text{D}_x\text{MnO}_3$ is an antiferromagnet for $x > 0.5$; whereas for $x < 0.5$, it is a ferromagnetic insulator (FMI) at smaller values of x (i.e., $0.1 \lesssim x \lesssim 0.2$) [9, 10, 18] and is a ferromagnetic metal at higher dopings in $\text{La}_{1-x}\text{Sr}_x\text{MnO}_3$, $\text{La}_{1-x}\text{Ca}_x\text{MnO}_3$, $\text{Pr}_{1-x}\text{Sr}_x\text{MnO}_3$, and $\text{Nd}_{1-x}\text{Sr}_x\text{MnO}_3$. Representative studies of doped manganite-manganite heterostructures can be found in Ref. [34–36]. We exploit the fact that the different magnetic phases occurring in the phase diagram are very close in energy and hence small perturbations can cause transitions from one phase to the other. Cooperative electron-phonon interaction (CEPI) is shown to be an important component behind these physical phenomena, though a competition with various other interactions mentioned earlier decides the nature of the phase. We approach the two problems presented in this thesis by first constructing a Hamiltonian for the manganite het-

erostructure by considering all the relevant interactions (discussed earlier) in manganites. In the strong electron-phonon coupling limit, i.e., large g and in the non-adiabatic regime $t/\omega_0 \lesssim 1$, an effective polaronic Hamiltonian is derived, where g is the electron-phonon coupling strength, t is the hopping integral, and ω_0 is the optical phonon frequency. Here, an originally strong-coupling problem, with small parameter $\propto g\omega_0/t$, is mapped on to a weak-coupling problem with small parameter $\propto t/g\omega_0$. This strong-weak duality transformation is crucial in trying to solve the problem analytically using perturbation theory. Since we are using the cooperative effects of the electron-lattice interactions, a modified Lang-Firsov transformation is used to produce the transformed Hamiltonian for perturbation theory. Subsequently, with some algebra, we derive the effective Hamiltonian restricting it to second-order perturbation terms. In the first problem of this thesis, assuming a heterostructure of the form

(Insulator)/(LaMnO₃)_n/(CaMnO₃)_n/(Insulator) [37], we establish that a giant magnetoelectric (ME) effect occurs away from the interface utilizing the basic property of manganites that electric order (charge order) can control magnetic order (spin order) and vice versa. A lot of work has been reported earlier regarding ME effect [38–41] such as the coupling between the electric polarization of a ferroelectric and the magnetization of a ferromagnet due to proximity effect in a Ferroelectric-Ferromagnet heterostructure. Contrastingly, we have shown that in a heterostructure composed of a few layers of LaMnO₃ and CaMnO₃, both of which are antiferromagnetic insulators, charges leak from LaMnO₃ to CaMnO₃ causing a strong multiferroic effect; furthermore, a striking magnetoelectric effect ensues when electric fields are applied. We find that there exists an effective electron-hole attraction resulting from the CEPI in the system. Double exchange, when an electron at a site virtually jumps to its nearest-neighbor site and comes back, brings about ferromagnetic (FM) order in the system by producing magnetic polarons in the system. Hence,

production of minority carriers in the system, i.e., holes on the LaMnO_3 side and electrons on the CaMnO_3 side, accounts for both charge polarization (due to production of dipole moments in the system) perpendicular to the interface and ferromagnetic ordering (due to the combined effect of CEPI plus double exchange). We have worked out the problem both analytically and with greater accuracy also simulated it numerically to demonstrate the robustness of the ME phenomenon. For analytic treatment, charge profile is calculated based only on the effective polaronic Hamiltonian and the Coulomb interaction in the continuous approximation. There is a net positive charge on the LaMnO_3 side and a net negative charge on the CaMnO_3 side and the system acts like a capacitor. For a symmetric heterostructure comprised of an equal number of layers of LaMnO_3 and CaMnO_3 , the charge density of the interface layer is calculated to be 0.5, which is irrespective of the presence or absence of an electric field, and hence is perfectly ferromagnetic. For the magnetization calculations, we invoke superexchange interaction and assume negligible kinetic energy in the system. On the CaMnO_3 side (which, in the undoped case, is a G-AFM band insulator), using a FM domain percolating from the interface, the magnetization is shown to decay with distance from the totally FM interface. On the LaMnO_3 side (which, in the undoped case, is an A-AFM Mott insulator) however, starting with a few MnO_2 layers, we show that the magnetization changes away from the interface from being antiferromagnetic to fully ferromagnetic when a sufficiently strong electric field is applied. Numerically, we compute the charge densities and average magnetization of the layers by using exact diagonalization of the single particle total Hamiltonian (containing the charge and spin degrees of freedom together) and minimize the system energy to reach the ground state by classical Monte Carlo technique using Metropolis algorithm. For strong g , we have site-localized minority carriers in the system and charge density is found to be checkerboard type near the interface leading to ferromagnetic order. Away from the minority carriers,

the magnetic profile is still representative of the bulk, but in their vicinity magnetic polarons are formed in the system. A collection of interacting magnetic polarons forms the FMI region. Application of an external electric field above a cut-off creates greater number of minority carriers away from the interface and results in higher magnetic order due to the magnetic polarons coalescing to form larger ferromagnetic domains. Thus, the FMI region expands at the cost of the A-AFM region producing a giant ME effect as high as $\simeq 0.17/\text{site}$. We further demonstrate that this effect is persistent for larger values of g and yields a greater change in magnetization for symmetric heterostructures. We also show that this heterostructure/device can be used near helium liquefaction temperatures; on the other hand, the magnetoelectric function disappears before nitrogen liquefaction temperature is attained (possibly due to reduced dimensionality). Putting this work in perspective with other reported works in the literature, we observe that the FMI phase which is key to the ME effect is not captured in the phase diagram of the bulk LCMO reported in Ref. [32]; this is possibly because small values of $\lambda = 2E_{JT}/t$ (with E_{JT} being the Jahn-Teller energy) were chosen and cooperativity in the electron-phonon interaction was ignored. Inspired by the results of the first problem, we further probe the FMI region in the second problem of this thesis [42]—FMI phase being a generic feature in the phase diagrams of manganite heterostructures. The FMI phase is manifested in the wide-band manganite $\text{La}_{1-x}\text{Sr}_x\text{MnO}_3$ in the doping region $0.1 \leq x \leq 0.18$ [43], in the intermediate-bandwidth $\text{La}_{1-x}\text{Ca}_x\text{MnO}_3$ in the doping range $0.1 \leq x \leq 0.225$ [43, 44], and in the narrow-bandwidth $\text{Pr}_{1-x}\text{Ca}_x\text{MnO}_3$ in the region $0.1 \leq x \leq 0.3$ [43]. Understanding the coexistence of ferromagnetism and insulating behavior in manganites is an unsolved problem. Though in Ref. [45, 46] only a localized polaronic band is relevant and the upper wide band cannot overlap with the lower narrow polaronic band leading to an insulator, the ferromagnetism in the system has been described by a phenomenological polaronic energy term. In another work,

a simple type of phase separated state with ferromagnetic droplets (each containing one carrier) in an antiferromagnetic matrix was shown to be possible [47]. The mobility of these magnetic polarons is low and they are easily localized by disorder and Coulomb interactions. We propose a localized-band model involving effective intermediate-range electron- electron (electron-hole) repulsion (attraction) generated by cooperative electron-phonon interaction. As stated before, double exchange mechanism produces magnetic polarons in an antiferromagnetic environment; when these magnetic polarons coalesce and percolate the system, we get an FMI. Ferromagnetism gets more pronounced when the hole carrier concentration increases or when the ratio hopping/(polaronic-energy) dominates over superexchange-coupling/hopping. While considering cooperative effects in the system we keep track of occupancies of nearest neighbors of the intermediate site when a hole jumps from an originating site to its nearest-neighbor intermediate site. In doing so we involve next-to-next-nearest-neighbor (NNNN) and next-nearest-neighbor (NNN) interactions in the system. The temperature variation of the total magnetization of the system in the experimentally relevant doping regime of $0.1 \leq x \leq 0.3$ in bulk manganites indicates an almost fully FMI at $x=0.3$ for an intermediate-band width manganite in two dimensions (2D) and for temperatures low enough compared to superexchange energies. This is in agreement with the percolation picture described in Ref. [48]. For lower hole dopings, the system of holes remains non-interacting and, by virtue of ferromagnetic superexchange interaction along columns, yields a low magnetization. Increased carrier concentrations bring forth first NNNN and then NNN interactions that aid in forming larger spin polarons in the system. A competition between the temperature and the antiferromagnetic superexchange interactions is visible from the crossover region at moderate dopings where magnetization curves for different temperatures intersect, after which percolation effects completely set in. Lastly, comparative studies of the low-bandwidth A-AFM manganites

with the moderate-bandwidth G-AFM managnites helps in understanding the reason for wider crossover regimes, importance of antiferromagnetic superexchange interactions in producing frustrations in the system, and finally in suspecting the possible occurrence of a superspin glass phase at lower temperatures in tune with the experimental findings in Ref. [49]. In summary this thesis presents a yet unobserved giant ME effect in the pure manganite-managnites heterostructures; it also acts as a theoretical guide for the experimentalists to realize this ME effect in the laboratory. That there is a scope for future device fabrication, if this effect is properly established experimentally, makes the work noteworthy. Apart from having a technological importance, the study of the FMI region, captured through our theoretical modeling and complying with available experimental evidences, helps in adding to the current understanding and resolution of this unexplained generic phase in the complex phase diagram of manganites as well as manganite heterostructures.

LIST OF FIGURES

1.1	Schematic diagram showing the various degrees of freedom (such as charge, spin and orbital degrees) that are interrelated to each other and the various symmetries that can be engineered at oxide interfaces (From Hwang <i>et al.</i> , Nature Materials 11 ,103113 (2012)).	4
1.2	Different types of spin orderings in manganites.	10
1.3	The perovskite structure of $A_{1-x}B_xO_3$, where A implies trivalent rare-earth (RE) elements (such as La, Pr, Nd, etc.) and B refers to divalent alkaline-earth elements (Sr, Ca, etc.).	12
1.4	The MnO_6 octahedra with p orbitals of the oxygen atoms pointing towards the Mn-O-Mn bonds.	12

- 1.5 Mn ion in a crystal field. On the left we have the 5 different d orbitals, that form the higher energy e_g doublet and the lower energy t_{2g} triplet. On the right, the actual energy level scheme shows the mechanism of crystal field splitting. $10Dq \sim 1\text{eV}$ is the energy gap between the two crystal-field split sets of orbitals. The t_{2g} electrons form the $S = 3/2$ core spin (both in Mn^{3+} and Mn^{4+}), while the e_g electron is itinerant. The lone e_g electron in Mn^{3+} further splits the e_g doublet. 14
- 1.6 The various relevant normal modes: (a) Q_3 JT mode where movement of the in-plane oxygen atoms is opposite to that of the out-of-plane atoms; (b) Q_2 JT mode where only the in-plane oxygens move; O atoms move inward in one direction (say, along x direction) and move outward in the perpendicular direction (i.e., along y direction); (c) Q_1 breathing mode where the movement of oxygen atoms mimic the breathing process, i.e., all of them either move inward or move outward. 18
- 1.7 An MnO_6 octahedra indicating the displacements of the oxygens, from their equilibrium positions, along the three axes. (From Dagotto *et al.* Phys. Rep., **344** 1-153 (2001)). 27
- 1.8 Phase diagram of $\text{La}_{1-x}\text{Ca}_x\text{MnO}_3$. FM: ferromagnetic metal; FI (or FMI): ferromagnetic insulator; AF: antiferromagnet; CAF: canted antiferromagnet; CO: charge/orbital order. (From S.-W. Cheong *et al.*, in Colossal Magnetoresistive Oxides, edited by Y. Tokura, Gordon and Breach, Amsterdam (2000)). 29

- 1.9 The magnetic and electronic phases in (a) $\text{La}_{1-x}\text{Sr}_x\text{MnO}_3$, (b) $\text{Nd}_{1-x}\text{Sr}_x\text{MnO}_3$, and (c) $\text{Pr}_{1-x}\text{Ca}_x\text{MnO}_3$. PI, PM, and CI stand for paramagnetic insulator, paramagnetic metal, and spin-canted insulator, respectively. FI (or FMI), FM, AFM, and AFI denote ferromagnetic insulator, ferromagnetic metal, antiferromagnetic metal, and antiferromagnetic insulator, respectively (From Tokura *et al.*, J. Magn. Magn. Mater. **200**, 1, (1999)). 30
- 1.10 Colossal magnetoresistance (CMR) behaviour for the $\text{La}_{0.67}\text{Ca}_{0.33}\text{MnO}_3$ single crystal. (From Y. Tokura, Rep. Prog. Phys., **69**, 797 (2006)) The resistivity of the manganite is plotted as a function of temperature for different strengths of magnetic fields varying from 0T to 7T. The resistivity peak gets suppressed with the increase in magnetic field, thus accounting for the large change in magnetoresistance. 32
- 1.11 The different kinds of spin and orbital orderings in manganites that constitute the various phases in their phase diagrams. (a) The $d_{3x^2-r^2}$ or $d_{3y^2-r^2}$ orbitals are antiferromagnetically coupled in a plane but ferromagnetically connected in between the planes ; spins are ferromagnetically coupled in a plane with antiferromagnetic coupling in between the planes (b) Both linear combinations of $d_{3z^2-r^2}$ and $d_{x^2-y^2}$ orbitals and spins are ferromagnetically connected to each other (c) Alternate arrangement of holes and orbitals ($d_{3x^2-r^2}$ or $d_{3y^2-r^2}$) in a zigzag chain; ferromagnetic arrangement of spins on zigzag chains with different chains being antiferromagnetically coupled (d) Ferromagnetic arrangement of $d_{x^2-y^2}$ orbitals with spins being ferromagnetically coupled in a plane but antiferromagnetically coupled in between the planes (e) Ferromagnetic arrangement of $d_{3z^2-r^2}$ orbitals; ferromagnetic chains of spins antiferromagnetically aligned (e) Antiferromagnetic arrangement of spins throughout. 33

2.1	Schematic showing the relationship between ferromagnetic (FM), the ferroelectric (FE), multiferroic (MF) and magnetoelectric (ME) materials.(Adapted from Eerenstein <i>et al.</i> , Nature 442 , 759-765 (2006)).	36
2.2	Schematic showing the symmetric manganite-manganite heterostructure (Insulator)/(LaMnO ₃) _N /Interface/(CaMnO ₃) _N /(Insulator). Each of the labeled N layers on both LMO (LaMnO ₃) and CMO (CaMnO ₃) sides contain manganese-oxide (MO) layers.	44
2.3	Electronic charge density $n(z_N)$ and per-site magnetization $m(z_N)$ (of t_{2g} spins normalized to unity) in various manganese-oxide layers of a (Insulator)/(LaMnO ₃) ₂ /Interface/(CaMnO ₃) ₂ /(Insulator) heterostructure for $a = 4$ Å, $\epsilon = 20$, and $C_1 = 0.24$. Figures are for (a) $n(E_{\text{ext}} = 0 \text{ kV/cm})$; (b) $\Delta n = n(E_{\text{ext}} = 300/400 \text{ kV/cm}) - n(E_{\text{ext}} = 0 \text{ kV/cm})$; and (c) $m(z_N)$ at $E_{\text{ext}} = 0 \text{ kV/cm}$, 300 kV/cm , and 400 kV/cm . MO layer 1 on the LMO side undergoes spin reversal when $E_{\text{ext}} = 400 \text{ kV/cm}$ is applied.	49
2.4	Electronic charge density $n(z_N)$ and per-site magnetization $m(z_N)$ (of normalized-to-unity t_{2g} spins) in various manganese-oxide layers of a (Insulator)/(LaMnO ₃) ₂ /Interface/(CaMnO ₃) ₂ /(Insulator) heterostructure for $a = 4$ Å, $\epsilon = 20$, and $C_1 = 0.31$. Plots pertain to (a) $n(E_{\text{ext}} = 0 \text{ kV/cm})$; (b) $\Delta n = n(E_{\text{ext}} = 100 \text{ kV/cm}) - n(E_{\text{ext}} = 0 \text{ kV/cm})$; and (c) $m(z_N)$ at $E_{\text{ext}} = 0 \text{ kV/cm}$ and $E_{\text{ext}} = 100 \text{ kV/cm}$. The LMO side becomes completely ferromagnetic when $E_{\text{ext}} = 100 \text{ kV/cm}$ is applied.	50

- 2.5 Layer-averaged charge density $\langle n(I) \rangle$ and layer-averaged per-site magnetization $\langle m(I) \rangle$ (of t_{2g} spins normalized to unity) for a symmetric 12×8 LMO-CMO lattice when electron-phonon interaction is zero; $J_z = 0.01t$ and $J_{xy}/J_z = 1.39$; $T = 0.001t$; and when (a) external electric field $E_{\text{ext}} = 0$ and (b) $E_{\text{ext}} = 400 \text{ kV/cm}$ 62
- 2.6 Layer-averaged charge density $\langle n(I) \rangle$ and layer-averaged per-site magnetization $\langle m(I) \rangle$ (of t_{2g} spins normalized to unity) for a symmetric 12×8 LMO-CMO lattice when electron-phonon interaction $g = 0$; superexchange $J_z = 0.02t$ and coupling ratio $J_{xy}/J_z = 1.39$; $T = 0.001t$; and when (a) $E_{\text{ext}} = 0$ and (b) $E_{\text{ext}} = 400 \text{ kV/cm}$ 63
- 2.7 Layer-averaged charge density $\langle n(I) \rangle$ and layer-averaged per-site magnetization $\langle m(I) \rangle$ (of normalized-to-unity t_{2g} spins) for a symmetric 12×8 LMO-CMO lattice when $g = 0$; $J_z = 0.01t$ and $J_{xy}/J_z = 1.39$; enhanced temperature $T = 0.01t$; and when (a) $E_{\text{ext}} = 0$ and (b) $E_{\text{ext}} = 400 \text{ kV/cm}$ 64
- 2.8 In a 12×8 symmetric lattice, when electron-phonon interaction strength $g = 2.0$, (a) when external electric field $E_{\text{ext}} = 0$, layer-averaged profiles of charge density $\langle n(I) \rangle$ and magnetization $\langle m(I) \rangle$ (of the t_{2g} spins normalized to unity); (b) when external electric field $E_{\text{ext}} = 0$, schematic occupation-number representation of ground state charge configuration in the lattice; (c) when a large external electric field $E_{\text{ext}} = 300 \text{ kV/cm}$ is applied, modified layer-averaged charge density $\langle n(I) \rangle$ and layer-averaged magnetization $\langle m(I) \rangle$ (of the t_{2g} spins normalized to unity) for various layers in the lattice; and (d) when $E_{\text{ext}} = 300 \text{ kV/cm}$, reorganized ground state charge configuration. 66
- 2.9 Charge modulation due to Coulomb interaction H_{coul} in a one-dimensional symmetric LMO-CMO lattice. The number of neutral layers/sites is x 67

- 2.10 Total magnetization as a function of temperature for various E_{ext} in a 12×8 lattice when electron-phonon coupling $g = 2.0$. Figure shows that an enhancement in magnetization occurs for electric fields $E_{\text{ext}} \gtrsim 300$ kV/cm; whereas below this threshold value, total magnetization does not change from its value at $E_{\text{ext}} = 0$ kV/cm. The magnetoelectric effect is reasonably large at temperatures below $0.5te^{-g^2}$ (~ 10 K). 68
- 2.11 Result of enhanced electron-phonon coupling $g = 2.2$ and zero electric field, in a symmetric 12×8 lattice, on (a) layer-averaged charge density $\langle n(I) \rangle$ and layer-averaged magnetization $\langle m(I) \rangle$ (of the t_{2g} spins normalized to unity); and (b) ground state charge configuration. 69
- 2.12 In a symmetric 12×6 lattice, for enhanced coupling $g = 2.2$, (a) at zero electric field, layer-averaged charge density $\langle n(I) \rangle$ and layer-averaged magnetization $\langle m(I) \rangle$ of t_{2g} spins normalized to unity; (b) at $E_{\text{ext}} = 0$, ground state configuration; (c) at strong external electric field $E_{\text{ext}} = 400$ kV/cm, layer-averaged charge density $\langle n(I) \rangle$ and layer-averaged magnetization $\langle m(I) \rangle$ of t_{2g} spins normalized to unity; and (d) at $E_{\text{ext}} = 400$ kV/cm, charge configuration in the ground state. 70

- 2.13 In a symmetric 12×6 lattice, for reduced coupling $g = 2.0$ and for the heterostructure $\text{Ins.}/(\text{LaO-MnO}_2)_n/(\text{La}_{1/2}\text{Ca}_{1/2}\text{O})/(\text{MnO}_2\text{-CaO})_n/\text{Ins.}$ with $Z_j = 0.75$ ($Z_j = 0.25$) for the layer adjacent to interface on the LMO (CMO) side, (a) at zero electric field, layer-averaged charge density $\langle n(I) \rangle$ and layer-averaged magnetization $\langle m(I) \rangle$ of t_{2g} spins normalized to unity; (b) at $E_{\text{ext}} = 0$, ground state configuration; (c) at strong external electric field $E_{\text{ext}} = 400 \text{ kV/cm}$, layer-averaged charge density $\langle n(I) \rangle$ and layer-averaged magnetization $\langle m(I) \rangle$ of t_{2g} spins normalized to unity; and (d) at $E_{\text{ext}} = 400 \text{ kV/cm}$, charge configuration in the ground state. 72
- 2.14 In asymmetric heterostructure defined on a 12×8 lattice with 2 layers of LMO and 6 layers of CMO, when coupling $g = 2.0$, (a) at $E_{\text{ext}} = 0$, layer-averaged charge density $\langle n(I) \rangle$ and layer-averaged magnetization $\langle m(I) \rangle$ of normalized-to-unity t_{2g} spins; (b) at $E_{\text{ext}} = 0$, ground state configuration; (c) at $E_{\text{ext}} = 300 \text{ kV/cm}$, layer-averaged charge profile $\langle n(I) \rangle$ and layer-averaged magnetization profile $\langle m(I) \rangle$ of normalized-to-unity t_{2g} spins; and (d) at $E_{\text{ext}} = 300 \text{ kV/cm}$, ground state configuration. 75
- 2.15 In asymmetric 12×8 lattice with 6 layers of LMO and 2 layers of CMO, when electron-phonon interaction $g = 2.0$, (a) at external electric field $E_{\text{ext}} = 0$, layer-averaged electron density $\langle n(I) \rangle$ and layer-averaged magnetization $\langle m(I) \rangle$ of t_{2g} spins normalized to unity; (b) at $E_{\text{ext}} = 0$, ground state electronic configuration; (c) at $E_{\text{ext}} = 300 \text{ kV/cm}$, layer-averaged electron density $\langle n(I) \rangle$ and layer-averaged magnetization $\langle m(I) \rangle$ of t_{2g} spins normalized to unity; and (d) at $E_{\text{ext}} = 300 \text{ kV/cm}$, ground state. 76

- 3.1 Schematic diagram for a 2D cooperative breathing mode (CBM) system. Hopping sites for holes are represented by blue solid circles, in-plane oxygen atoms (participating in the CBM) by black empty circles, and non-cooperative out-of-plane oxygen atoms by solid black circles. 85
- 3.2 Schematic diagram for the four possibilities of a hole, at an originating site (i, j) , hopping to its NN site (the intermediate site) and coming back (when three NN sites of the intermediate site are occupied by electrons): (A) hole at (i, j) hops to its right NN at $(i + 1, j)$ and comes back; (B) hole at (i, j) jumps to its left NN at $(i - 1, j)$ and returns back; (C) hole at (i, j) jumps to its downward NN at $(i, j - 1)$ and comes back; (D) hole at (i, j) hops to its upper NN at $(i, j + 1)$ and returns. A hole is represented by a blue solid circle and a particle (i.e., electron) by a blue empty circle. All lattice sites that are not relevant to the consideration are represented by black solid circles. 90
- 3.3 Schematic diagram for a hole at an originating site (i, j) hopping to its NN site (the intermediate site) and returning back (when any two of the NN sites of the intermediate site are occupied by electrons). Representation of a hole at (i, j) jumping to its right NN at $(i + 1, j)$ and coming back when holes occupy (a) right and downward NNs of the intermediate site; (b) right and upward NNs of the intermediate site; (c) upward and downward NNs of the intermediate site. A hole is depicted by a blue solid circle and a particle by a blue empty circle. All lattice sites that are not relevant to the consideration are represented by black solid circles. 91

- 3.4 Schematic diagram for a hole at an originating site (i, j) hopping to its NN site (the intermediate site) and coming back (when any one of the NN sites of the intermediate site is occupied by an electron). Depiction of a hole at (i, j) jumping to its right NN at $(i + 1, j)$ and coming back when a particle occupies (a) downward NN of the intermediate site; (b) right NN of the intermediate site; (c) upward NN of the intermediate site. A hole is represented by a blue solid circle whereas a particle by a blue empty circle. All lattice sites that are not relevant to the consideration are indicated by black solid circles. 93
- 3.5 Schematic diagram for a hole at an originating site (i, j) hopping to its NN site (the intermediate site) and coming back (when all the other three NN sites of the intermediate site are occupied by electrons). Representation of a hole at (i, j) jumping to its right NN at $(i + 1, j)$ and coming back. A hole is represented by a blue solid circle and a particle by a blue empty circle. All lattice sites irrelevant to the analysis are represented by black solid circles. . . . 95
- 3.6 Averaged per-site magnetization $\langle m_i \rangle$ (of spins normalized to unity) as a function of hole doping x for two different lattices (6×12 and 12×12) and for a fixed $T = 0.001t$ 100
- 3.7 Charge configurations in the ground state of a 6×12 lattice. An arbitrarily chosen degenerate ground state, involving 72 sites, for (a) 12 holes, (b) 14 holes, (c) 16 holes, (d) 18 holes, (e) 22 holes, (f) 24 holes (diagonal stripe order), (g) 32 holes, and (h) 36 holes. 101
- 3.8 Averaged per-site total magnetization $\langle m_i \rangle$ (of spins normalized to unity) as a function of the number of holes doped for a 6×12 lattice and for various temperatures (expressed in units of hopping parameter t). The background spin configuration is A-AFM type and hopping $t = 0.3$ eV. 103

3.9	Averaged per-site total magnetization $\langle m_i \rangle$ (of spins normalized to unity) as a function of the number of holes doped for a 6×12 lattice and for various temperatures (in units of hopping t). The background spin configuration is A-AFM and $t = 0.2$ eV.	104
3.10	Averaged per-site total magnetization $\langle m_i \rangle$ (of spins normalized to unity) as a function of the number of holes doped for a 6×12 lattice and for various fixed temperatures (in units of hopping parameter t). The background spin configuration is G-AFM type and $t = 0.3$ eV.	106
3.11	Averaged per-site total magnetization $\langle m_i \rangle$ (of spins normalized to unity) as a function of the number of holes doped for a 6×12 lattice and for various fixed temperatures (in units of hopping parameter t). The background spin configurataion is fully FM and $t = 0.3$ eV.	107

CHAPTER 1

INTRODUCTION

Unveiling the physics behind the Strongly Correlated Electronic (SCE) materials has garnered the interest of most condensed matter physicists for a long time. For SCE materials, which harbor non-trivial electron-electron correlations, the independent electron approximation (i.e., treating the electrons as non-interacting) turns out to be invalid and model Hamiltonians are used to study their exotic properties. The model Hamiltonians may be very simple to write with electron-electron or Coulomb interactions, Coulomb-lattice interactions and tunneling of electrons between various atomic sites (or lattice sites) dictated by tight-binding hopping integrals, but solving them analytically may often become quite demanding. Though scientifically sound approximations may help in a little advancement in this respect, very often absence of small parameters makes the expansion of the many-body SCE Hamiltonian next to impossible. Computational measures therefore become indispensable in solving the SCE systems, the primary aim being finding the many-body ground state of the system. Furthermore in SCE systems, the surprising co-existence of myriads of phases that closely compete and show non-linear responses when subjected to

small perturbations like magnetic field, electric field, strain, disorder etc., calls for the study of the excited states of the SCE systems also. Although understanding the behavior of SCE materials is hard, the wide range of technological applications that they present is quite exciting and useful.

1.1 Strongly correlated oxides

Among the different SCE systems, oxides have gained considerable importance because of the various fundamental and application oriented phenomena displayed by them. The cuprate family of superconductors brought forth by Bednorz and Müller [50] challenged the applicability of the BCS (Bardeen-Cooper-Schrieffer) picture [51] incorporating simple mean-field descriptions and involving Cooper pairs of larger size. In this new “high- T_c ” superconductors, Cooper pairs were found to be comparable to inter-carrier distances, mean-field theoretic approaches were rendered inapplicable and phase competition became unavoidable leading to different *inhomogeneous* patterns of carriers giving rise to stable states. Attention is also being given to doped bismuthates, specifically Pb or K doped BaBiO_3 , which show metal-semiconductor phase transitions with change in doping concentration and temperature, charge-density-wave ordering and superconductivity with moderately high T_c [52]. Nickelates find applications in the study of artificial neuromorphic devices; SmNiO_3 , that shows a metal-insulator (MI) transition in the bulk form, has been used to produce a synaptic transistor to imitate the working of neural synapses [53]. MI transitions are typical of rare-earth nickelates, the study of which remains one of the most sought after phenomena in solid state physics [54]. Titanates, such as BaTiO_3 , on the other hand are very good ferroelectrics [55]. They form the base material for the construction of monolithic ceramic multilayer capacitors that find applications in semiconductor

circuits [56]. Single-layer perovskite cobaltates are finding relevance in the SCE family since, much like the high- T_c cuprates [57], they produce the hourglass excitation spectrum. The incommensurate magnetic peaks in $\text{La}_{5/3}\text{Sr}_{1/3}\text{CoO}_4$ may be indicative of charge stripes which directly connect to the hourglass shaped spectrum [58].

1.2 Superlattices, thin films and heterostructures of oxides

The interest in finding new collective states slowly digressed from single crystals or naturally occurring compounds of TMOs (transition metal oxides) to surfaces and interfaces formed by structurally and chemically dissimilar materials [6, 59]. This revival aimed at exploring physics similar to that exhibited by junctions of two different semiconductors (SCs) to which fractional quantum Hall effect [60, 61], spin-Hall effect [62] and other such phenomena owe their discovery. In semiconductor interfaces, differences in work functions are responsible for charge transfer across the junction which ultimately make the chemical potentials of both the sides to be equal. Initially the idea was simply to have a better version of semiconductor junctions since oxides were found to have (1) carrier densities $\sim 10^{22} \text{ cm}^{-3}$, orders of magnitude greater than SCs; (2) much shorter Thomas-Fermi screening lengths so that charges could be confined within 1-2 nm unlike in SCs which have length scale confinements of $\sim 10 \text{ nm}$ [63, 64]. Present day endeavors are however mostly focused in utilizing the oxide heterostructures as SCE systems, engineering and controlling charge, spin, lattice, and orbital properties to tailor states at the interface not achievable or obtained in bulk.

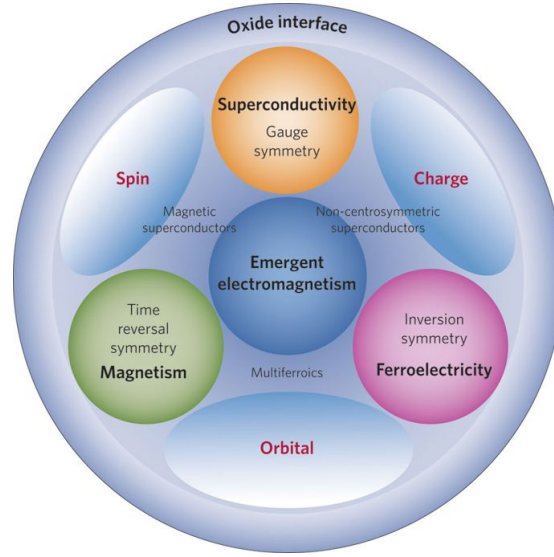


Figure 1.1: Schematic diagram showing the various degrees of freedom (such as charge, spin and orbital degrees) that are interrelated to each other and the various symmetries that can be engineered at oxide interfaces (From Hwang *et al.*, Nature Materials **11**,103113 (2012)).

As compared to the bulk doped oxides where volume effects are operative, if we zero in on surfaces of bulk materials, thin films and consequently interfaces of TMO oxides, we find a complete change in the correlated behavior, transport and electronic properties and opening of new paradigms of device fabrication possibilities. This is mostly due to the two-dimensional character of the surfaces or interfaces, breaking of translational and inversion symmetries, change in lattice periodicity due to mismatch in lattices of the two parent TMOs and also reduced kinetic energy effects in the system. For example, breaking inversion symmetry implies appearance of non-trivial ferroelectric and compatible magnetic states arising at the interface. Then, lattice parameter matching is important as a mismatch denotes possible changes in interatomic distances across the interfaces and consequent changes in hopping probability t . Hopping t may also change due to structural reconstruction and relaxations that may eventually occur due to rearrangement of the whole lattice

structure. Again quite naively it can be understood that a reduction in the number of nearest neighbors when we move from a bulk three dimensional oxide to a surface layer directly reduces the effective bandwidth of the system to $W = 2z^*t$ from being $2zt$, z and z^* being the coordination numbers in bulk and surfaces respectively. This effective lowering of the kinetic energy of the electrons in the system thus renders possible insulating behaviors in the electronic states at the interface. A good example would be that of a nickelate LaNiO_3 , which in the bulk is metallic but when made into thin films or layered structures remains insulating for a certain number of layers. [65].

Control of orbital polarization at the interface has also been attempted for the case of rare-earth nickelates. A substrate seems to play a significant role because the strain it provides can suppress lattice distortions that favors a particular orbital ordering. The contribution of superexchange [66] to orbital ordering may also change and give rise to new magnetic orderings. In NdNiO_3 films, strain controls the metal-insulator transition (MIT) effectively [67,68] and it has been found that orbital polarization under compressive strain produces metallicity when quantum confinement is at the atomic level but causes a MIT when polarization is reduced [69]. In VO_2 thin films also, orbital polarization is seen to play a role in decreasing the MIT temperature [70].

Orbital reconstruction is also noticed when $\text{La}_{1-x}\text{Ca}_x\text{MnO}_3$, a colossal magnetoresistance (CMR) manganite, is placed in proximity to a high- T_c cuprate $\text{YBa}_2\text{Cu}_3\text{O}_7$ [71,72]. Charge transfer across the junction from Mn to Cu is found to be the cause behind this major reconstruction at the hetero-interface. Experiments have revealed that the superconducting transition temperature is curbed and so is the Curie temperature related to ferromagnetism arising from the manganite layers [73–75]. Nemes and co-workers have found evidences of superconductivity supporting parallel alignment of spins under an applied magnetic field [76] which may find applications in spintronics.

Perhaps the most studied hetero-interface till date, that of $\text{LaAlO}_3/\text{SrTiO}_3$, has received a huge attention because the interface is metallic although the bulk parent materials are wide gapped insulators [6,59,77,78]. Depending on the kind of layer terminations, there can be two kinds of interfaces: $\text{AlO}_2\text{-LaO-TiO}_2$ which is conducting and $\text{AlO}_2\text{-SrO-TiO}_2$ that is found to be insulating. As is understood, the layers in the SrTiO_3 side, $\text{Ti}^{4+}\text{O}_2^{2-}$ and $\text{Sr}^{2+}\text{O}^{2-}$ are charge neutral whereas in the LaAlO_3 side, $\text{Al}^{3+}\text{O}_2^{2-}$ layers have charge = -1 and $\text{La}^{3+}\text{O}^{2-}$ have charge = +1 per unit cell. Thus there is an excess unbalanced charge at the interface and the electrostatic potential of such a system is found to grow linearly with the thickness of the heterostructure. At a certain thickness, the potential drop may even exceed the energy gap E_g of the system, making it unstable. This instability due to the diverging potential, called the polarization catastrophe, is overcome by electronic reconstruction by which half a charge is transferred from the upper surface to the bottom layer. Thus the upper layer of two insulators is expected to be metallic, though of course there is a critical thickness for obtaining this metallic conductivity. One can never rule out possible formation of oxygen vacancies as part of non-stoichiometric changes in the system supplying the free carriers in the system and accounting for the metallic behavior; this is under study. This two-dimensional electron gas (2DEG), that shows up at the interface, is also reported to show 2D superconductivity with $T_c \simeq 0.2\text{K}$ [79] which may have its origin in the electron doping of the SrTiO_3 surface. In some cases, however, there can be phase separated superconducting and ferromagnetic states aided by the oxygen vacancy formation [80,81].

Magnetic states at the interface can be manipulated by placing say an antiferromagnetic insulator in the vicinity of a paramagnetic metal as in $\text{CaMnO}_3/\text{CaRuO}_3$ heterostructures [82–84]. With moderate electron-doping, the interface shows ferromagnetism although the magnitude of leaked charges is quite small. Moetakef *et al.* have discovered an insulat-

ing phase [85], not quite the usual Mott phase typical of TM ions in $\text{GdTiO}_3/\text{SrTiO}_3$ heterostructures, naming it the “Mott-dimer” phase [86].

Up till a few years ago, the celebrated quantum hall effect had been observed in traditional semiconductor junctions such as $\text{AlGaAs}/\text{GaAs}$ only. Oxide heterostructures of $\text{Mg}_x\text{Zn}_{1-x}\text{O}/\text{ZnO}$ have proved to be excellent systems in demonstrating quantum Hall effect [87–89] with high carrier mobilities, strong correlation effects, large magnetic susceptibilities, formation of quantum Hall ferromagnetic states, realization of the coveted $\nu = 1/3$ fractional quantum Hall state, and lastly an ionized impurity free system where orbital character and spin polarization can both be tuned. Charge accumulation at the interface (in the narrow bandgap ZnO), much akin to that of the LAO/STO system, happens to arise as a need to compensate the mismatch in piezoelectric properties of the two compounds and thus helps in the realization of this emergent interface phenomena.

It is needless to say that a lot of other TMO oxide superlattices, thin films, and atomically controlled heterostructures are being prepared artificially to study various interface effects, comprehensive studies of which can be found in a growing body of literature [6,90].

Keeping in view the various other TMOs and their heterostructures that can also offer interesting emergent physics and technological promise, this thesis tries to explore special kind of oxides called manganites and focuses on the novel properties that their heterostructures can exhibit. One such important phenomena in manganite heterostructures is the magnetoelectric effect which will be studied in detail along with the associated ferromagnetic insulating properties. Before getting into it, we will revisit below a few of the efforts dedicated to the study of manganite multilayers to illustrate the vast possibilities they offer.

Strain-driven phase transitions including orbital order are very common for example in $(\text{LMO})_1/(\text{SMO})_1$ superlattices; here, the ground state can be tuned based on the c/a ratio, where a is the lattice constant in the xy plane and c is that in the z direction. The

system stabilizes, for $c \simeq a$ showing FM order; for $a > c$, A-AFM order; and for $a < c$, C-AFM [91]. It should be noted that C-AFM phase does not appear in bulk LSMO around 0.5 electron density. Density Functional Theory (DFT) studies by Nanda and Satpathy [30] also captured similar phases in this superlattice. Biaxial strain, depending on being tensile or compressive in nature, has shown evidence of metallic behavior with strong ferromagnetism or insulating behavior with weak ferromagnetism [92, 93]. Although SMO has a robust G-AFM spin order, (LMO)₁/(SMO)₃ superlattices showed various interfacial magnetic arrangements such as A-AFM, FM, and C-AFM [30].

In (LMO)_{2n}/(SMO)_n superlattices, $n = 1$ samples resembled the bulk counterparts in terms of low resistivities, precisely stating $n \leq 2$ samples are metallic (see Ref. [20]). In fact, one expects the A/B cation disorder to be less in well prepared (LMO)₂/(SMO)₁ superlattices compared to the bulk counterpart (or alloy) La_{2/3}Sr_{1/3}MnO₃. Next, the $n > 3$ state has much larger resistivities giving rise to an insulating state.

1.3 Introduction to manganites

The first work that reported the importance of manganites was the renowned paper by Jonker and Van Santen in 1950 [94] in which they studied doped systems such as La_{1-x}Ca_xMnO₃, La_{1-x}Sr_xMnO₃, and La_{1-x}Ba_xMnO₃ and recorded the existence of ferromagnetism in them. In their paper, manganites appear as A_{1-x}B_xMnO₃ with A a trivalent rare-earth ion such as La³⁺, B a divalent alkali metal ion such as Ca²⁺, and x the fraction of Mn sites that are Mn⁴⁺. The manganites were noticed to crystallize in a perovskite structure with the oxygens surrounding the Mn-site ion building up an octahedral cage. A subsequent paper by them [95] was about the conductivity of manganites with anomalies reported at the Curie temperature. Jonker also studied lattice parameters in the system as a function of

hole doping and tried to explain the different levels of distortions at different carrier concentrations, indicative of the role Jahn-Teller effect plays in manganites [96]. Subsequently in 1954, Volger tried measuring changes in resistance of the compound $\text{La}_{0.8}\text{Sr}_{0.2}\text{MnO}_3$ in presence of magnetic fields and at different temperatures [97]. He commented that “manganites, when in the ferromagnetic state, show a notable decrease of resistivity in the magnetic fields”, though the now well-known colossal magnetoresistance effect was noticed much later in the 90’s. The most noted work on manganites from the earlier days is the neutron diffraction measurement done by Wollan and Koehler in the year 1955 [98]; they detected many rich antiferromagnetic phases in $\text{La}_{1-x}\text{Ca}_x\text{MnO}_3$ in addition to the ferromagnetic phase described by Jonker and Van Santen. Their studies revealed (which phase diagrams of modern day manganites also contain) the different kinds of antiferromagnetic phases such as the A-type (ferromagnetic planes of spins antiferromagnetically connected) near $x = 0$, the G-type (antiferromagnetic planes of spins antiferromagnetically connected) near $x = 1$, C-type (chains of ferromagnetic spins antiferromagnetically connected) around $x = 0.75$ or $x = 0.80$, and also B-type (ferromagnetic spins in all three directions) in fully ferromagnetic regions as shown in Fig. 1.2. The fact that the phases also depicted a concomitant charge order with spin orders is convincingly expressed in the CE-type phase (see Fig. 1.11) that Wollan and Koehler pointed out as the mixture of C-type and E-type structures with an intrinsic charge ordering. Thereafter in 1979, Jirák and co-authors [99] and in 1982 Pollert and his co-workers [100] analyzed the structural and magnetic properties of $\text{Pr}_{1-x}\text{Ca}_x\text{MnO}_3$ (PCMO). PCMO was found to be structurally distorted at various fillings and the resultant charge orders and magnetic phases were very different from the ferromagnetic phases in other manganites.

Dramatic changes in resistivity of manganites on application of magnetic fields started

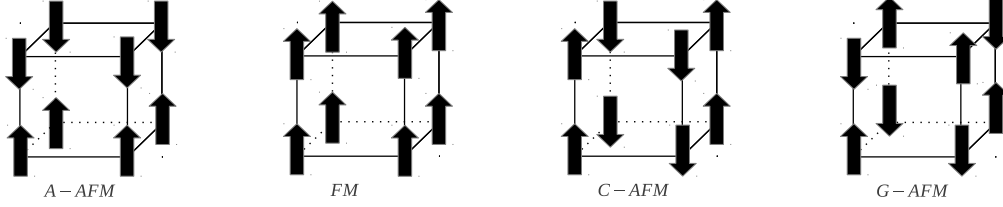


Figure 1.2: Different types of spin orderings in manganites.

to be observed by various groups studying $\text{Nd}_{0.5}\text{Pb}_{0.5}\text{MnO}_3$ [101], thin films of $\text{La}_{2/3}\text{Ba}_{1/3}\text{MnO}_3$ at room temperature [102], thin films of $\text{La}_{1-x}\text{Ca}_x\text{MnO}_3$ at $x = 0.25$ [103] and films of $\text{La}_{1-x}\text{Sr}_x\text{MnO}_3$ at room temperature [104]. Nevertheless, truly “colossal” magnetoresistance ratios were first recorded in 1994 by Jin *et al.* [105] in $\text{La}_{0.67}\text{Ca}_{0.33}\text{MnO}_3$ to be around 1500% when temperature is cooled down to 200K and still larger ratios of 100,000% at 77K. Later Xiong [106] observed even higher MR ratios of 1,000,000% in thin films of $\text{Nd}_{0.7}\text{Sr}_{0.3}\text{MnO}_3$ near 60K and with 8T magnetic field. This CMR effect generated tremendous interest due to the exotic fundamental physics and significant potential application in spintronics. Slowly it became clear that there was more to the field of manganites than the CMR effect. From $x = 0.3$, attention got shifted to other densities, such as $x < 0.2$ or $x > 0.5$, initially to probe further into other magnetic and charge ordered phases that were crucial to explain CMR. Later on, understanding the origin of these phases itself proved to be non-trivial from the viewpoints of fundamental physics and device potential. More works were devoted towards understanding the interplay of various degrees of freedom leading to those exotic phases. Phase competition and its manipulation by weak perturbations became a widely studied subject in strongly correlated manganites. The clean systems already revealed different closely coexisting energy

states. Tendencies of phase separation and disorder effects further led to inhomogeneous states [107].

1.4 Review of manganites

1.4.1 Crystal Structure

The structure of $A_{1-x}B_x\text{MnO}_3$ is very near to being a cubic perovskite (see Fig. 1.3). Manganites have a simple cubic space lattice. The coordinates of the various ions in the cubic lattice are: A/B ion at (0,0,0), Mn ion at (1/2,1/2,1/2), and three O ions at (0,1/2,1/2), (1/2,0,1/2), and (1/2,1/2,0). Now, we have AMnO_3 at zero doping in which A has +3 charge and O_3 has -6 charge; thus, Mn has to have a valency of +3 to maintain charge neutrality. We have BMnO_3 at 100% doping in which B has +2 charge, O_3 has -6 charge, thus changing the valence of Mn to +4. For the doped compound, we have a mixed-valence state of Mn as $A_{1-x}^{3+}B_x^{2+}\text{Mn}_{1-x}^{3+}\text{Mn}_x^{4+}\text{O}_3^{2-}$. We can also imagine the structure of AMnO_3 as stacking of AO planes over MnO_2 planes. The Mn ions are surrounded by oxygen atoms forming an octahedral arrangement. The p orbitals of the oxygen atoms point towards the Mn-O-Mn bonds as shown in Fig. 1.4.

1.4.2 Tolerance factor

The tolerance factor is a geometrical factor defined as $\Gamma = \frac{d_{\text{C-O}}}{\sqrt{2}d_{\text{Mn-O}}}$, where $d_{\text{C-O}}$ is distance between the trivalent A or divalent B cation at the vertices of the cube and the nearest neighbor oxygen ion and $d_{\text{Mn-O}}$ is the shortest distance of the Mn ion at the center of the cube from the oxygen ions at the face centers of the cube. With no distort-

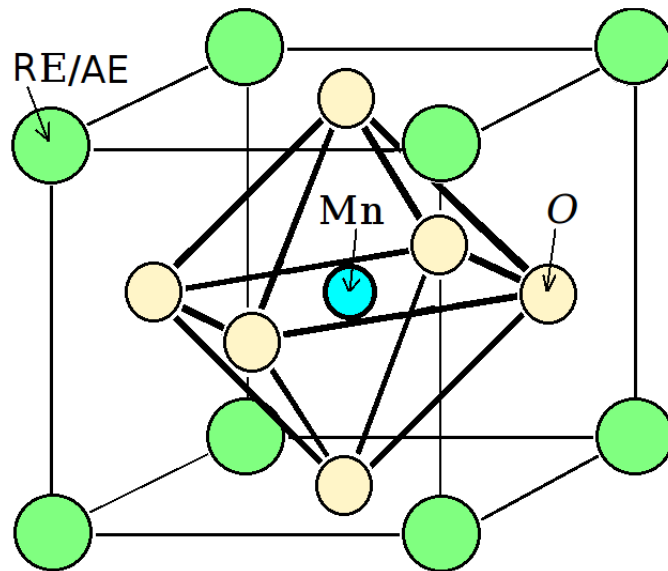


Figure 1.3: The perovskite structure of $A_{1-x}B_xO_3$, where A implies trivalent rare-earth (RE) elements (such as La, Pr, Nd, etc.) and B refers to divalent alkaline-earth elements (Sr, Ca, etc.).

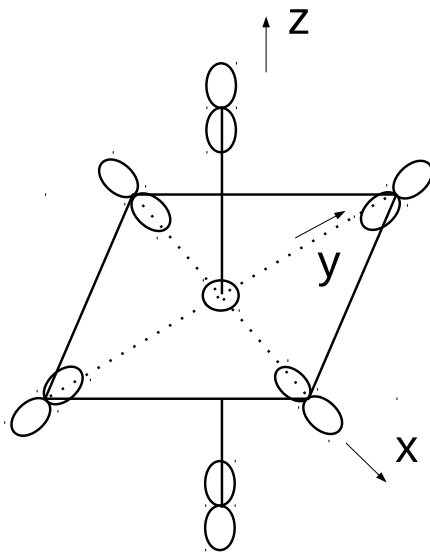


Figure 1.4: The MnO_6 octahedra with p orbitals of the oxygen atoms pointing towards the Mn-O-Mn bonds.

tions, ideally the face diagonal, C-O-C, equals $\sqrt{2}$ times the cube edge, O-Mn-O, i.e., $2r_C + 2r_O = \sqrt{2}(2r_{Mn} + 2r_O)$, r_C denotes the radius of the A/B cation; r_{Mn} and r_O the radii of Mn and O ions, respectively. At times, if the radius of the A/B ions is too small, the oxygens tend to move more towards the Mn ions; hence, d_{C-O} reduces and consequently d_{Mn-O} also changes. This makes $\Gamma < 1$ and correspondingly the Mn-O-Mn bond angle θ to be less than 180 degrees. As the hopping amplitude for charges (to move from one Mn site to the nearest Mn site) depends on $\cos \theta$ (as will be described in detail later), a reduction in tolerance factor ultimately reduces this hopping probability. Thus localization tendencies in the system increases. It is to be noted that, if we consider a doped manganite, we have two possible cations A and B and hence the density-weighted average of the individual tolerance factors are considered.

1.4.3 Crystal field splitting

The 3d transition metals (TMs) in the periodic table have active d-shells containing five degenerate orbitals (angular momentum quantum number $l = 2$; $l_z = 2, 1, 0, -1, -2$). Each orbital is actually an electronic wave function with pear-shaped lobes. Three of them lie in the xy, yz and xz planes, respectively, and are therefore called the d_{xy} , d_{yz} , and d_{xz} orbitals. The fourth one has its lobes along the x and y axes and is called the $d_{x^2-y^2}$ orbital. The last orbital (i.e., $d_{3z^2-r^2}$ orbital) is a bit different from the rest in that it not only has pear-shaped lobes symmetrical in the z direction but also a torus encircling it in the middle. When isolated, there is degeneracy in the five orbitals due to presence of spherical symmetry (or rotational invariance) present in the $l = 2$ sector, that is to say, all the crystal axes are equivalent. When placed inside a crystal with other ions in their surrounding, full rotational invariance is lost and the structure of the crystal determines the resultant local symmetry.

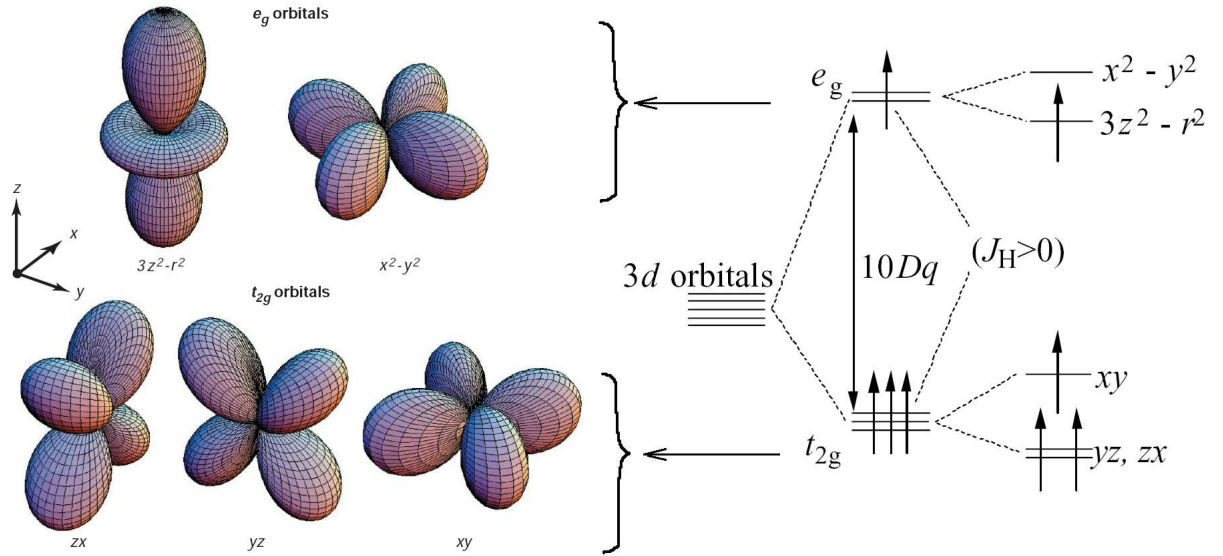


Figure 1.5: Mn ion in a crystal field. On the left we have the 5 different d orbitals, that form the higher energy e_g doublet and the lower energy t_{2g} triplet. On the right, the actual energy level scheme shows the mechanism of crystal field splitting. $10Dq \sim 1\text{eV}$ is the energy gap between the two crystal-field split sets of orbitals. The t_{2g} electrons form the $S = 3/2$ core spin (both in Mn^{3+} and Mn^{4+}), while the e_g electron is itinerant. The lone e_g electron in Mn^{3+} further splits the e_g doublet.

Thus the fivefold degeneracy breaks into a lower t_{2g} triplet and an upper e_g doublet in the cubic crystal field, with six oxygen ions (also called the ligand ions) surrounding the Mn ion forming an octahedron.

Due to symmetry considerations, d_{xy} , d_{yz} and d_{xz} should be affected in a similar way as the three crystal axes are equivalent; they form the triplet. On the other hand, $3z^2 - r^2$, which can be written as $(z^2 - x^2) + (z^2 - y^2)$, can be understood to be symmetrically equivalent to $(x^2 - y^2)$ and hence $d_{x^2-y^2}$ and $d_{3z^2-r^2}$ are degenerate. While the wave functions of the $d_{x^2-y^2}$ and d_{z^2} orbitals are extended along the direction of the Mn-O-Mn bonds, those of the d_{xy} , d_{yz} and d_{xz} orbitals are not. Hence, since overlap of wave functions of the d orbitals

and the oxygen ions is considerably more for the former case, Coulombic repulsions with the negatively charged oxygen ions are greater. The doublet has thus a higher energy than the triplet, the energy gap being ~ 1 eV.

1.4.4 The different degrees of freedom

1.4.4.1 Charge

The electronic configuration of Mn is $3d^5 4s^2$; thus, Mn^{3+} is $3d^4$ and Mn^{4+} is $3d^3$. Thus the 3 three t_{2g} levels are filled with 3 of the electrons in both Mn^{3+} and Mn^{4+} ; the higher energy e_g level has 1 electron in Mn^{3+} and 0 electron in Mn^{4+} giving rise to $t_{2g}^3 e_g^1$ and $t_{2g}^3 e_g^0$ configurations, respectively. The itinerant e_g electron determines the net charge of the system with undoped $\text{A}^{3+}\text{Mn}^{3+}\text{O}_3^{2-}$ having electron density 1 and the doped compound $\text{A}_{1-x}^{3+}\text{B}_x^{2+}\text{Mn}_{1-x}^{3+}\text{Mn}_x^{4+}\text{O}_3^{2-}$ (being richer in holes) having electron density less than 1.

1.4.4.2 Spin

As the overlap integral between t_{2g} and oxygen p orbital is small compared to that between e_g and p orbitals, the three t_{2g} spins can be treated as a large localized classical spin with $S = 3/2$. Due to strong Hund's coupling in manganites, the e_g spin is always parallel to the spin-polarized t_{2g} sector. This is how the itinerant charge is connected to the core t_{2g} spins in the system and various arrangements of these localized core spins generate different magnetic orders in the system.

1.4.4.3 Orbitals

Due to the crystal-field splitting of the 5 different d orbitals into e_g and t_{2g} levels, electrons are filled starting from the lower energy t_{2g} levels following Hund's rules. For Mn^{3+} , since

we have four d electrons, the t_{2g} subshell will be half-filled with three parallel spin electrons; the remaining one electron with a parallel spin can be placed in any one of the two degenerate e_g levels or a linear superposition of them. So in addition to the spin degeneracy, in which the spin of the electron can be either up or down, we encounter an orbital degeneracy (i.e., an extra double degeneracy). However, nature does not favor the orbital degeneracy of the electronic ground state of a non-linear molecule [108]. Hence, there is an instability to ensure lowering of the system energy, i.e., the non-linear molecule undergoes a geometrical distortion spontaneously. In case of manganites [109, 110], the only degeneracy that is allowed is the spin degeneracy that is related to the time reversal symmetry and can only be broken by an external magnetic field or by some magnetic ordering. Now, readjustments of the oxygen ions around the TM ion, creating an asymmetry in the different directions, essentially lifts the orbital degeneracy. That the system symmetry is unstable with respect to the distortions in the MnO_6 octahedra, thus leading to lifting of the degeneracy to reach a lower energy state, is the essence of the Jahn-Teller effect. We can clearly see that Mn^{4+} has no e_g electron and hence is not a Jahn-Teller (JT) active cation [109, 110]. A small calculation shows that the energy gain due to lattice distortions grows as square of the distortions while that due to energy splitting is linear, hence getting overcompensated by the former. Thus, after the JT effect, electrons occupy specific orbitals. So orbital ordering and JT effect occur simultaneously and are inter-related. Now, from isolated JT ions, moving over to concentrated systems where we have a large number of JT ions present (practically one in each unit cell of a cubic lattice), it is natural that there will be interactions among the distortions making neighboring JT active ions also interacting. The very fact that two adjacent MnO_6 octahedra share a common oxygen implies coupling of their distortions and also leads to coupling of orbital occupations on the adjacent centers. Thus the different octahedra do not undergo independent distortions any

more and the whole crystal becomes unstable due to this interlinking effect. This is called cooperative Jahn-Teller effect (CJTE). This also leads to cooperative orbital orderings.

In the octahedra, we have 7 atoms and thereby $(7 \times 3) = 21$ degrees of freedom (DOF). Since motion of the center of mass of the system is not considered, 3 DOF are subtracted. Rotation of the octahedra is also not considered, hence 3 more DOF get subtracted. So in all we have 15 DOF and hence 15 independent modes of vibration. Out of this, only 3 normal modes (i.e., 2 JT modes and 1 breathing mode) contribute to our picture; the other modes allow movements of oxygen atoms which would result in buckling of the Mn-O-Mn bond and reduce the hopping amplitudes of the electrons. The relevant modes are the Q_1 , Q_2 and Q_3 modes as shown in Fig. 1.6. In the Q_1 mode, the oxygen atoms along all the three axes either move outwards together or move inwards toward the Mn atom thereby imitating the breathing process. In the Q_2 mode (which is a JT mode) there is no movement of the oxygen atoms in the z-direction (see Figs. 1.4 and 1.6). The O atoms move outward in the x direction and move inward in the y direction or vice versa. So we have two long bonds, two short bonds, and two unchanged bonds. In the Q_3 mode (which also is a JT mode), we have O atoms along z direction moving outward and those along x and y directions moving inwards or vice versa. Thus we have two long and four short bonds or vice versa.

1.5 Magnetic interactions

Magnetic interactions in the manganites is governed not singly by the d orbital physics of the Mn ions. Due to the presence of ligand oxygen ions in the system and Mn-O-Mn bonds, there occurs a strong hybridization between the d orbitals of the Mn ions and the oxygen p orbitals directed towards the Mn ions. The direct overlap between adjacent Mn ions is small and different hopping mechanisms are thus mediated by the intervening

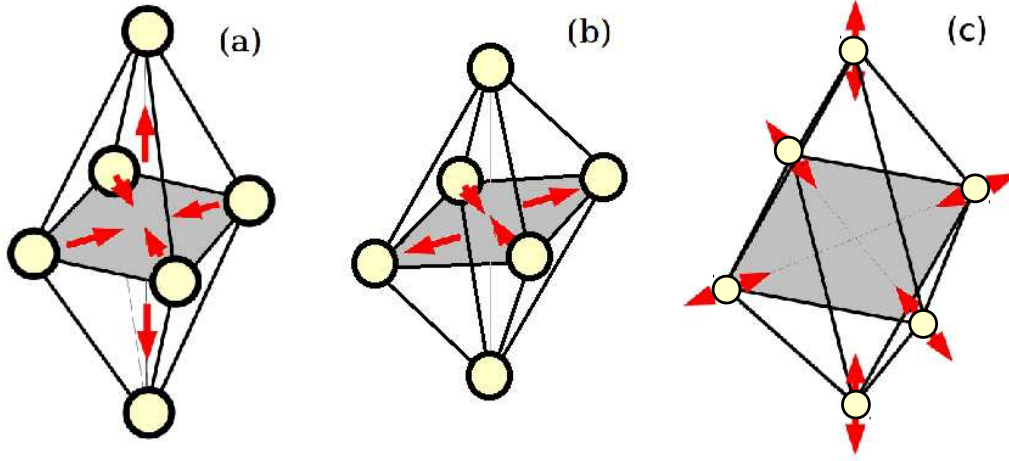


Figure 1.6: The various relevant normal modes: (a) Q_3 JT mode where movement of the in-plane oxygen atoms is opposite to that of the out-of-plane atoms; (b) Q_2 JT mode where only the in-plane oxygens move; O atoms move inward in one direction (say, along x direction) and move outward in the perpendicular direction (i.e., along y direction); (c) Q_1 breathing mode where the movement of oxygen atoms mimic the breathing process, i.e., all of them either move inward or move outward.

oxygen atoms. Depending on these processes, different magnetic interactions are present in manganite systems: the most important being double exchange and superexchange.

1.5.1 Double exchange

Ferromagnetism observed in various experimental findings in the 1950's stimulated theoretical understanding of its origin by Zener in 1951 in three of his important papers [111–113]. In his first paper, though Zener has not explicitly talked about manganites, he has attributed ferromagnetism to an indirect coupling between the “incomplete d shells” by means of “conducting electrons” in the system. It is obvious that in the manganite language, the polarized t_{2g} spins denote the incomplete d shells and the conducting elec-

trons represent the e_g electrons. Zener proposed the idea that for the e_g electrons to move throughout the crystal from one Mn site to the other, it is favorable for the background t_{2g} spins to be parallel, otherwise there is an energy cost equal to the Hund's exchange. This leads to ferromagnetism in the system. In a later work, Zener mentioned that transfer of the electron from one Mn site to the other is mediated by the in-between oxygen atoms. This idea of Zener was subsequently improved upon by Anderson and Hasegawa [114] and by de Gennes [115] who put forward the definition of an effective hopping $t_{\text{eff}} = t \cos \theta/2$ with θ being the angle between two nearest-neighbor t_{2g} spins.

We will now outline the essence of de Gennes approach [115]. The Hamiltonian for double exchange can be written as the sum of the kinetic energy and the on-site Hund's coupling between the e_g electrons and the core t_{2g} spins.

$$H_{DE} = \sum_{\langle i,j \rangle} t a_{i\sigma}^\dagger a_{j\sigma} - 2J_H \sum_i \vec{s}_i \cdot \vec{S}_i, \quad (1.1)$$

where $a_{i\sigma}^\dagger$ and $a_{j\sigma}$ are the creation and annihilation operators for the e_g electrons; s_i is the spin of the electron and S_i is that of the t_{2g} spin at site i ; σ represents the spin index of the e_g electron; and J_H is the Hund's coupling constant. The Hund's coupling term $-2J_H \vec{s} \cdot \vec{S}$ leads to eigen values $-J_H S$ and $J_H(S+1)$. Now, we consider two directions, given by spins \vec{S}_1 and \vec{S}_2 (at atoms 1 and 2, respectively), with an angle θ between them. For the direction of \vec{S}_1 (\vec{S}_2) as the axis of quantization, let the electronic spin state vector be given as $\alpha|\uparrow\rangle + \beta|\downarrow\rangle$ ($\alpha'|\uparrow\rangle + \beta'|\downarrow\rangle$). For the rotation operator being given by $\mathcal{U} = \exp\left(\frac{-i\vec{\theta} \cdot \vec{s}}{\hbar}\right)$, we can express α and β in terms of α' and β' as follows:

$$\begin{pmatrix} \alpha \\ \beta \end{pmatrix} = \begin{pmatrix} \cos \frac{\theta}{2} & \sin \frac{\theta}{2} \\ -\sin \frac{\theta}{2} & \cos \frac{\theta}{2} \end{pmatrix} \begin{pmatrix} \alpha' \\ \beta' \end{pmatrix}. \quad (1.2)$$

Let the electronic eigenstates of atom 1, referred to direction of \vec{S}_1 as the axis of quantization, be $|d_{1,\sigma}\rangle$ and $|d_{1,-\sigma}\rangle$; those of atom 2, referred to direction of \vec{S}_2 as the axis of quantization, be $|d_{2,\sigma'}\rangle$ and $|d_{2,-\sigma'}\rangle$. Now,

$$\langle d_{1,\sigma} | H_{DE} | d_{2,\sigma} \rangle = t, \quad (1.3)$$

$$\langle d_{1,\sigma} | H_{DE} | d_{2,-\sigma} \rangle = 0, \quad (1.4)$$

$$\langle d_{1,\sigma} | H_{DE} | d_{2,\sigma'} \rangle = t \cos \frac{\theta}{2}, \quad (1.5)$$

$$\langle d_{1,\sigma} | H_{DE} | d_{2,-\sigma'} \rangle = t \sin \frac{\theta}{2}, \quad (1.6)$$

$$\langle d_{1,\sigma} | H_{DE} | d_{1,\sigma} \rangle = -J_H S, \quad (1.7)$$

and

$$\langle d_{1,-\sigma} | H_{DE} | d_{1,-\sigma} \rangle = J_H (S + 1). \quad (1.8)$$

Then, the matrix representation of H_{DE} can be written as follows:

$$\begin{pmatrix} -J_H S & 0 & t \cos \frac{\theta}{2} & t \sin \frac{\theta}{2} \\ 0 & J_H(S+1) & -t \sin \frac{\theta}{2} & t \cos \frac{\theta}{2} \\ t \cos \frac{\theta}{2} & -t \sin \frac{\theta}{2} & -J_H S & 0 \\ t \sin \frac{\theta}{2} & t \cos \frac{\theta}{2} & 0 & J_H(S+1) \end{pmatrix}. \quad (1.9)$$

Next, when we solve the characteristic equation $|H_{DE} - EI| = 0$, we get the solutions as

$$E = \frac{J_H}{2} \pm \left\{ \left[J_H \left(S + \frac{1}{2} \right) \pm t \cos \frac{\theta}{2} \right]^2 + t^2 \sin^2 \frac{\theta}{2} \right\}^{\frac{1}{2}}. \quad (1.10)$$

For $J_H \gg t$ (as is true for manganites), we get the lowest eigen value of the system or the double exchange energy to be

$$E_{DE} = -J_H S \pm t \cos \frac{\theta}{2}. \quad (1.11)$$

1.5.2 Superexchange

Another coupling between two neighboring Mn^{3+} (well separated by the lattice constant $\simeq 4\text{\AA}$) is mediated by the virtual hopping of e_g electrons. It is infact an interaction between two magnetic ions via an intermediate non-magnetic/diamagnetic ion. If the two magnetic ions and the intermediate diamagnetic ion are arranged along one axis, the interaction between the magnetic ions is antiferromagnetic when only one orbital is considered for the magnetic ions and may be ferromagnetic or antiferromagnetic when two orbitals are

involved. Bonding and antibonding orbitals are formed due to the mixture of the d orbitals of Mn ions and the p orbitals of the oxygen ions. Thus the wavefunction of localized d spins extends over the neighboring negative ions. This is the reason why the exchange coming out of this is termed superexchange [116].

Now, consider the following bonding and antibonding states:

$$\psi_b \equiv \psi_{\text{bonding}} \simeq \psi_{p\sigma} + \lambda \psi_{d_{3z^2-r^2}}, \quad (1.12)$$

and

$$\psi_{ab} \equiv \psi_{\text{antibonding}} \simeq \psi_{d_{3z^2-r^2}} - (\lambda + O_I) \psi_{p\sigma}, \quad (1.13)$$

where $\lambda \ll 1$ and O_I is the overlap integral as will be shown below. Now,

$$\begin{aligned} \langle \psi_b | \psi_{ab} \rangle &= 0, \\ \implies \langle \psi_{p\sigma} | \psi_{d_{3z^2-r^2}} \rangle - (\lambda + O_I) + \lambda &= 0, \\ \implies O_I &\simeq \langle \psi_{p\sigma} | \psi_{d_{3z^2-r^2}} \rangle. \end{aligned} \quad (1.14)$$

Now, ψ_b is lower in energy than ψ_{ab} . Furthermore, ψ_{ab} extends over the negative ion and has the spin of the magnetic ion whereas the two original p_σ electrons of O^{2-} are in ψ_b . Hence, by considering ψ_{ab} , we eliminate the role of the intervening O^{2-} . Then, the total Hamiltonian is expressed as $H = H_0 + H_1$ where H_0 is the Hubbard U term and H_1 is the hopping term. To carry out perturbation theory, we invoke the following canonical

transformation:

$$\tilde{H} = e^T H e^{-T} \quad (1.15)$$

$$= H_0 + H_1 + [H_0 + H_1, T] + \frac{1}{2} [[H_0 + H_1, T], T] + \dots \quad (1.16)$$

To eliminate first order in H_1 , we set $H_1 + [H_0, T] = 0$. Thereafter, following standard Hubbard model calculations [117], we can arrive at the equation

$$\tilde{H} = -P_S \frac{H_1 H_1}{U} P_S = \frac{4t^2}{U} P_S [\vec{S}_2 \cdot \vec{S}_1 - \frac{1}{4} \hat{n}_2 \hat{n}_1] P_S, \quad (1.17)$$

where P_S is the projection operator for single occupancy of electrons; \vec{S}_2 and \vec{S}_1 are two nearest-neighbour spins; and n_i is the number density operator at site i . The superexchange energy coefficient is thus given by $J_{AF} = \frac{4t^2}{U}$.

1.6 Coulomb interaction

Since we have e_g electrons or holes in the system, electron-electron, hole-hole, or electron-hole interactions will come into play. Electrons hop from one atomic site to the other through various Wannier states that are localized at those sites. So, for a usual system of interacting electrons, we can write the Hamiltonian as

$$\begin{aligned} H &= T + V \\ &= \int d^3r \psi^\dagger(r) H_0 \psi(r) + \frac{1}{2} \int \int d^3r d^3r' \psi^\dagger(r) \psi^\dagger(r') V(r, r') \psi(r') \psi(r), \end{aligned} \quad (1.18)$$

where the kinetic energy operator $H_0(r) = -\hbar^2/2m\nabla^2$ and $V(r, r')$ is the interaction energy between two electrons with position coordinates r and r' . Now, expanding the

wave function of the particle in terms of Wannier basis we get

$$\psi(r) = \sum \phi_{i\gamma}(r) c_{i\gamma\sigma}. \quad (1.19)$$

Here, $\phi_{i\gamma}(r)$ is the Wannier function at site i and orbital γ ; $c_{i\gamma\sigma}$ is the electronic destruction operator at site i , orbital γ and with spin σ .

Thus, the kinetic energy of the electrons is found to be

$$T = \sum_{j,j',\gamma,\gamma',\sigma} t_{jj'}^{\gamma\gamma'} c_{j\gamma\sigma}^\dagger c_{j'\gamma'\sigma}, \quad (1.20)$$

where the hopping amplitude is defined to be

$$t_{jj'}^{\gamma\gamma'} = \int dr^3 \phi_{j\gamma}^*(r) H(r) \phi_{j'\gamma'}(r). \quad (1.21)$$

As the Wannier functions are reasonably localized at the different sites considered for hopping, the hopping amplitude is commonly restricted within nearest-neighbor sites only. However, larger hopping processes also become important under certain specific conditions. The above interaction term comprising four wave functions, although calls for a summation over four lattice indices, can be reduced to a summation over only a single lattice index. The realistic assumption is to consider that screening and polarization effects reduce the strength of the Coulomb interaction within electrons that are near to an ion. Denoting the Wannier states ($\phi_{i\gamma}(r)$) now by atomic orbitals only and ignoring the site index, we have the potential energy part as

$$V = 1/2 \sum_i \sum_{\gamma\beta\gamma'\beta'} \sum_{\sigma\sigma'} U(\gamma\beta;\gamma'\beta') c_{i\gamma\sigma}^\dagger c_{i\beta\sigma'}^\dagger c_{i\beta'\sigma'} c_{i\gamma'\sigma} \quad (1.22)$$

where

$$U(\gamma\beta;\gamma'\beta') = \int \int d^3r d^3r' \phi_\gamma(r) \phi_\beta(r') V(r, r') \phi_{\gamma'}(r) \phi_{\beta'}(r'). \quad (1.23)$$

Here, out of the large number of matrix elements $U(\gamma\beta;\gamma'\beta')$, we have the following independent elements: (i) the intraband Coulomb interaction $U = U(\gamma\gamma;\gamma\gamma)$; (ii) the interband Coulomb interaction $U' = U(\gamma\beta;\gamma\beta)$ where $\gamma \neq \beta$; (iii) the interband exchange interaction $J = U(\gamma\beta;\beta\gamma)$; and (iv) the pair-hopping amplitude between different orbitals $J' = U(\gamma\gamma;\beta\beta)$. However J' is not an extra parameter and it can be shown that $J = J'$. Furthermore, with some calculation, a relation between the other three parameters can be obtained to be $U = U' + 2J$. Hence, in the most generalized form, we can rewrite the Coulomb interaction in the following manner:

$$\begin{aligned} \hat{V} = & \frac{U}{2} \sum_i \sum_{\gamma, \sigma \neq \sigma'} n_{i\gamma\sigma} n_{i\gamma\sigma'} + \frac{U'}{2} \sum_i \sum_{\sigma, \sigma', \gamma \neq \gamma'} n_{i\gamma\sigma} n_{i\gamma'\sigma'} \\ & + \frac{J}{2} \sum_i \sum_{\sigma, \sigma', \gamma \neq \gamma'} c_{i\gamma\sigma}^\dagger c_{i\gamma'\sigma'}^\dagger c_{i\gamma\sigma'} c_{i\gamma'\sigma} + \frac{J'}{2} \sum_i \sum_{\sigma \neq \sigma', \gamma \neq \gamma'} c_{i\gamma\sigma}^\dagger c_{i\gamma\sigma'}^\dagger c_{i\gamma'\sigma'} c_{i\gamma'\sigma}. \end{aligned} \quad (1.24)$$

In the above equation, the first term represents electronic repulsion between electrons of opposite spin in the same site and orbital. The second term represents the Coulombic repulsion between electrons in the same ionic site but belonging to different orbitals. The third term actually represents the Hund's coupling where electrons in different orbitals are forced to be ferromagnetic to reduce the energy of the system. The fourth term represents hopping of pairs of electrons between two different orbitals of the same site. The interaction energy U , being the largest energy in manganites, suppresses double occupancy and hence makes the fourth term negligible. Further details can be found in Ref. [17].

1.7 Electron-phonon interaction

In the initial research works on manganites, double-exchange models were extensively used to describe ferromagnetism [111, 114, 118]. However, that double exchange alone is not enough to shed light on various parts of the phase diagram of manganites became evident from the studies by Millis, Littlewood, and Shraiman [119]. An estimation of the Curie temperature T_c , using a model that had a large Hund's coupling as the only interaction, led to values between 0.1 eV and 0.3 eV which were orders of magnitude higher than experimentally reported T_c values. A one-orbital model with $J_H = \infty$ used by Calderon [120] also led to metallicity both below and above T_c . All these findings only hinted at the fact that Jahn-Teller phonons had a role in determining the mixed-phase tendencies of manganites and in solving the anomalies regarding T_c and resistivity. In fact, the large Hund's coupling and strong electron-phonon interaction collude to produce kinetic energy reduction and consequent ferromagnetism in the system especially in the regime of low hole fillings [10]. Coupling lattice distortions to e_g electrons, Kanamori had first written down the basic Hamiltonian [121] for Jahn-Teller distortion at a site i as follows:

$$H_i^{JT} = -2G(Q_{2i}T_i^x + Q_{3i}T_i^z) + (k_{JT}/2)(Q_{2i}^2 + Q_{3i}^2), \quad (1.25)$$

where G is the electron-phonon coupling constant; Q_{2i} and Q_{3i} are JT modes of vibration of the oxygen octahedra; k_{JT} is the spring constant for the Jahn-Teller mode distortions. The pseudospin operators are defined as $T_i^x \equiv \sum_{\sigma} (d_{ia\sigma}^{\dagger} d_{ib\sigma} + d_{ib\sigma}^{\dagger} d_{ia\sigma})$ and $T_i^z \equiv \sum_{\sigma} (d_{ia\sigma}^{\dagger} d_{ia\sigma} - d_{ib\sigma}^{\dagger} d_{ib\sigma})$. For symmetry reasons, a T_i^y term does not appear in the expression for H_i^{JT} .

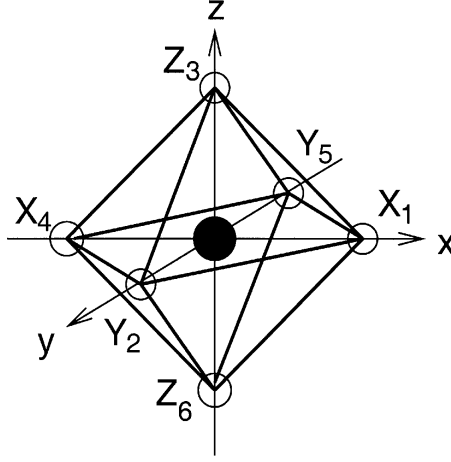


Figure 1.7: An MnO_6 octahedra indicating the displacements of the oxygens, from their equilibrium positions, along the three axes. (From Dagotto *et al.* Phys. Rep., **344** 1-153 (2001)).

Now, the JT distortions are expressed as follows:

$$Q_{2i} = \frac{1}{\sqrt{2}}(X_{1i} - X_{4i} - Y_{2i} + Y_{5i}), \quad (1.26)$$

and

$$Q_{3i} = \frac{1}{\sqrt{6}}(2Z_{3i} - 2Z_{6i} - X_{1i} + X_{4i} - Y_{2i} + Y_{5i}), \quad (1.27)$$

where $X_{\mu j}$, $Y_{\mu j}$, $Z_{\mu j}$ are displacements of the oxygens, from their equilibrium positions, along the three axes as depicted in Fig. 1.7. The ground state energy is found to be $E_{JT} = G^2/2k_{JT}$. Though the breathing mode does not remove the e_g orbital degeneracy of the system, it is an essential part of the electron-phonon interaction as this thesis will later emphasize. The breathing-mode energy is expressed as

$$H_i^{br} = gQ_{1i}\rho_i + 1/2k_{br}Q_{1i}^2, \quad (1.28)$$

with ρ_i being the local electron density to which the breathing-mode distortion Q_{1i} is coupled. Q_{1i} is given by

$$Q_{1i} = \frac{1}{\sqrt{2}}(X_{1i} - X_{4i} + Y_{2i} - Y_{5i} + Z_{3i} - Z_{6i}). \quad (1.29)$$

From Eq. (1.28), it can be understood that the breathing-mode-distortion energy increases as ρ_i (or the number of e_g electrons) increases; on the other hand, the JT distortion modes produce energy gain only if there is a single electron per site. The total electron-phonon interaction energy is expressed through $H_{el-ph} = \sum_i (H_i^{JT} + H_i^{br})$. It is important to recognize that cooperative treatments of the electron-phonon interaction utilize $X_{\mu j}$, $Y_{\mu j}$ and $Z_{\mu j}$ directly while non-cooperative electron-phonon couplings deal with Q 's.

1.8 Manganite phase diagram

We have manganites that have large bandwidth (such as $\text{La}_{1-x}\text{Sr}_x\text{MnO}_3$), intermediate bandwidth (such as $\text{La}_{1-x}\text{Ca}_x\text{MnO}_3$), and narrow bandwidth (such as $\text{Pr}_{1-x}\text{Ca}_x\text{MnO}_3$). Depending on the bandwidth variation, we have different phase diagrams (see Figs. 1.8 and 1.9). Since in this thesis work we will be primarily interested in intermediate- and narrow-bandwidth manganites, a brief overview of the general phase diagram of manganites is worth discussing [10, 122]. The tolerance factor described earlier is a measure of the bandwidth of a manganite, which is again directly proportional to the A/B cation radius r_C . Larger the value of r_C , the larger is the tolerance factor and also larger are the Mn-O-Mn bond angle and the hopping amplitude (or bandwidth). As large-bandwidth manganites have larger kinetic energy, they have predominant ferromagnetic and metallic tendencies. As tolerance factor decreases, the bandwidth reduces and concomitantly JT interactions

become more prominent [123]; furthermore, insulating behavior also gets enhanced. It is the combination of the effects of bandwidth, double exchange, JT distortion, and superexchange that lead to diverse magnetic, charge, and orbital ordered states in the phase diagram. It is quite interesting to note that the $x < 0.5$ and $x > 0.5$ regions in the phase diagrams are highly asymmetrical; the asymmetry is possibly due to the JT effect. In spite of the basic differences that exist between various bandwidth manganites, some common phases are manifested by some of them and we will point these out briefly.

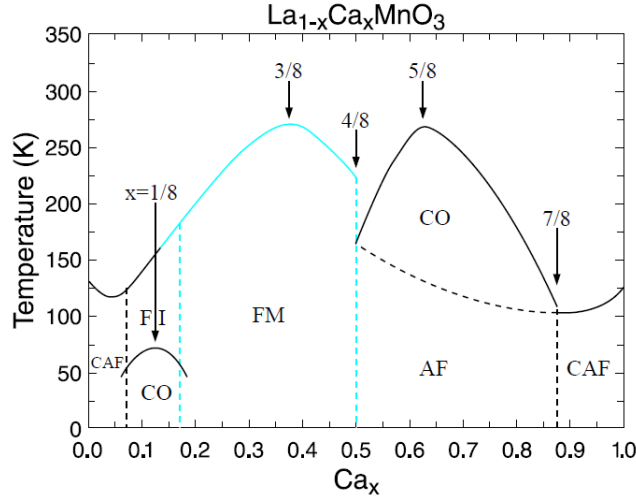


Figure 1.8: Phase diagram of $\text{La}_{1-x}\text{Ca}_x\text{MnO}_3$. FM: ferromagnetic metal; FI (or FMI): ferromagnetic insulator; AF: antiferromagnet; CAF: canted antiferromagnet; CO: charge/orbital order. (From S.-W. Cheong *et al.*, in *Colossal Magnetoresistive Oxides*, edited by Y. Tokura, Gordon and Breach, Amsterdam (2000)).

1.8.1 Insulating A-AFM

At zero hole doping, i.e., at $x = 0$, all the ions in the system are Mn^{3+} and hence are JT active. It can be shown that a linear combinations of the $d_{3z^2-r^2}$ and the $d_{x^2-y^2}$ orbitals give

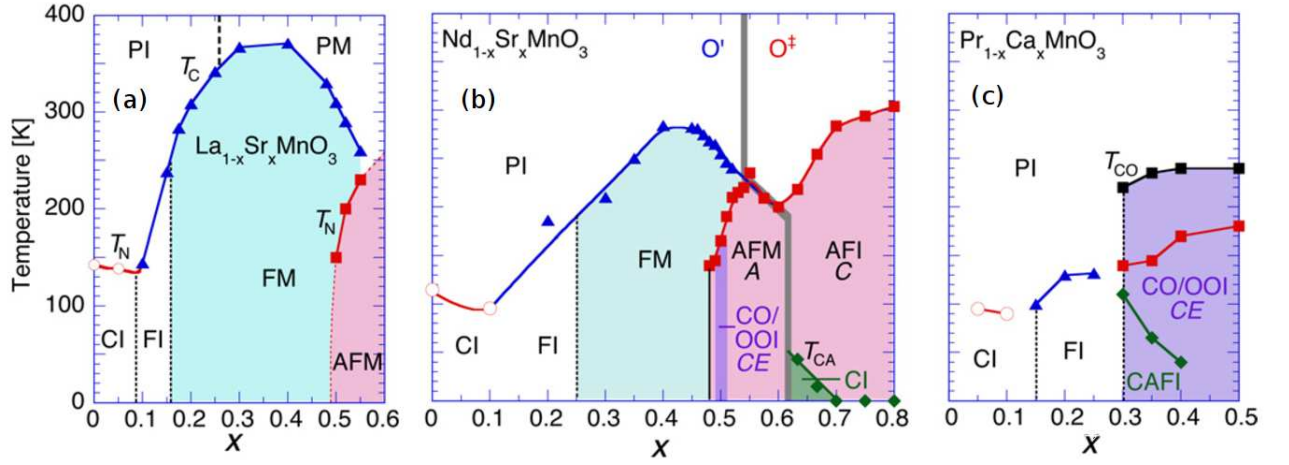


Figure 1.9: The magnetic and electronic phases in (a) $\text{La}_{1-x}\text{Sr}_x\text{MnO}_3$, (b) $\text{Nd}_{1-x}\text{Sr}_x\text{MnO}_3$, and (c) $\text{Pr}_{1-x}\text{Ca}_x\text{MnO}_3$. PI, PM, and CI stand for paramagnetic insulator, paramagnetic metal, and spin-canted insulator, respectively. FI (or FMI), FM, AFM, and AFI denote ferromagnetic insulator, ferromagnetic metal, antiferromagnetic metal, and antiferromagnetic insulator, respectively (From Tokura *et al.*, J. Magn. Magn. Mater. **200**, 1, (1999)).

rise to orbital states that extend along the x and y axes in the xy plane and produce Q_2 JT distortion. As a result there is an effective FM coupling of spins in the plane, while they are stacked antiferromagnetically in the z direction. This A-AFM phase is thus a 2D layered ferromagnet with a zero effective magnetization. Due to JT effects, electrons are localized in the various Mn^{3+} sites and we get an insulator. Hotta *et al.* [124] have reported that a small J_{AF} leads to A-AFM provided JT effects are properly incorporated in the model.

1.8.2 Canted AFM

At very low hole dopings in the system, addition of few Mn^{4+} ions in place of Mn^{3+} results in itinerant holes. Then, a competition between double exchange and antiferromagnetic superexchange ensues leading to a canting of the spins. However, there are controversies

regarding the canted phase; many works claim a phase separated state, involving AFM and FM phases, to be more stable than the canted state (see, for example, Ref. [47]).

1.8.3 Ferromagnetic insulator

A ferromagnetic insulating phase is obtained (at $T < T_c$ as shown in Figs. 1.8 and 1.9) for higher doping values $0.1 \lesssim x \lesssim 0.15$ in large- and intermediate-bandwidth manganites and for dopings extending to $x \sim 0.3$ in narrow-bandwidth manganites. For $T > T_c$, a paramagnetic insulator results; explanation for the PI phase is still missing. Quite importantly, the mechanism for the ferromagnetic insulating phase is not well understood; investigating the ferromagnetic insulator forms a significant aspect of this thesis.

1.8.4 Ferromagnetic metallic region

This is by far the most studied doped region in the phase diagram (of large- and intermediate-bandwidth manganites) and deals with the CMR phenomena that is potentially technologically important. At $x < 0.5$, there are sufficiently large number of holes in the system; double exchange processes are quite operational leading to ferromagnetic alignment of the spins so as to minimize the kinetic energy. However, as pointed out earlier, only the DE mechanism is not enough to predict the FM region since this leads to overestimation of MI transition temperatures. Hence, JT electron-phonon coupling should also be included in understanding the CMR phenomenon. In the CMR regime, the paramagnetic to ferromagnetic transition coincides with a maxima in the resistivity (ρ). Upon the application

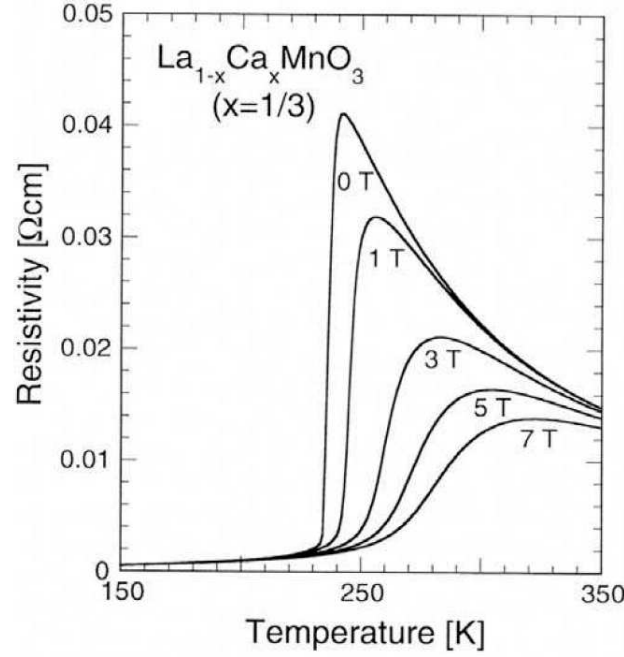


Figure 1.10: Colossal magnetoresistance (CMR) behaviour for the $\text{La}_{0.67}\text{Ca}_{0.33}\text{MnO}_3$ single crystal. (From Y. Tokura, Rep. Prog. Phys., **69**, 797 (2006)) The resistivity of the manganite is plotted as a function of temperature for different strengths of magnetic fields varying from 0 T to 7 T. The resistivity peak gets suppressed with the increase in magnetic field, thus accounting for the large change in magnetoresistance.

of a magnetic field H , there is a large change in ρ , i.e., $(\rho(H) - \rho(0)) / \rho(H)$ is colossal as shown in Fig. 1.10; hence, this phenomenon is termed colossal magnetoresistance effect.

1.8.5 A-AFM metal

At large dopings, the electron number decreases sizeably. In $\text{La}_{1-x}\text{Sr}_x\text{MnO}_3$ and $\text{Nd}_{1-x}\text{Sr}_x\text{MnO}_3$, at $0.5 \lesssim x \lesssim 0.6$, as shown in Fig. 1.9, A-AFM metallic state is realized. This state is actually FM in the xy planes and AF in the z direction. Within each plane, only the $d_{x^2-y^2}$ orbitals are occupied as depicted in Fig. 1.11 (d).

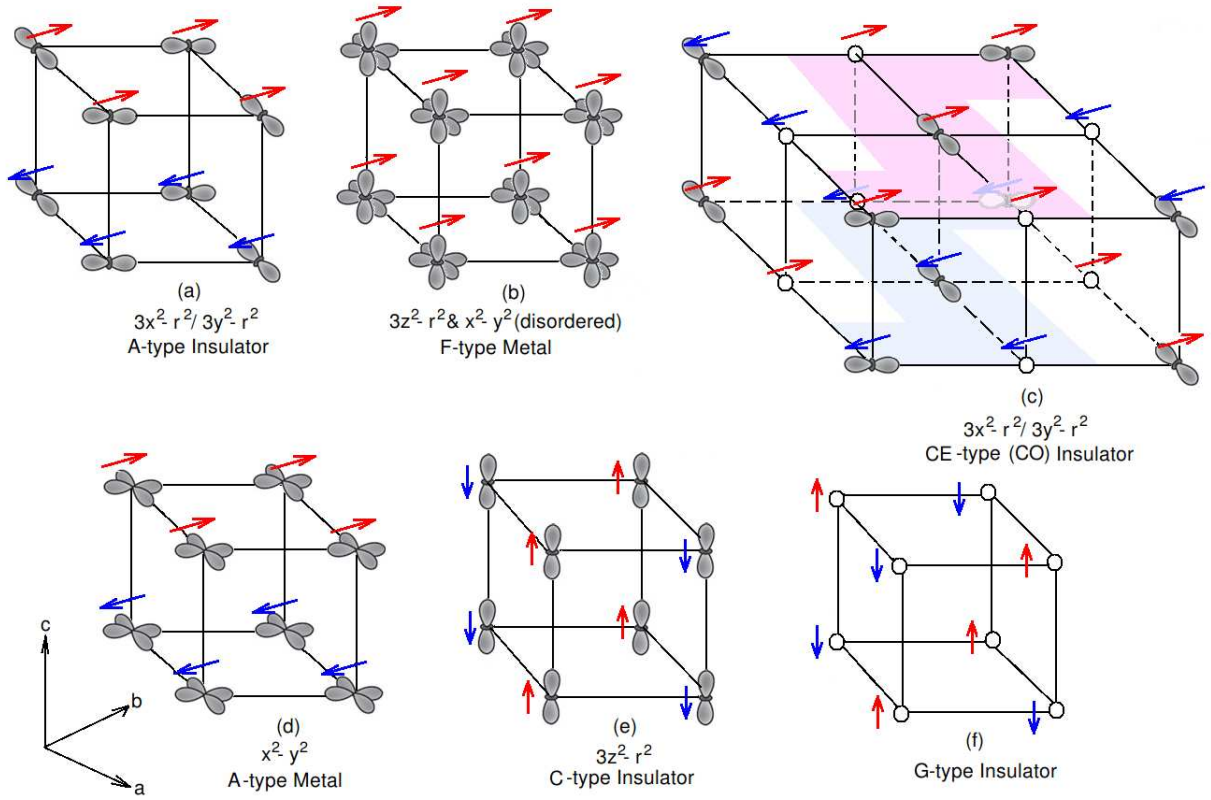


Figure 1.11: The different kinds of spin and orbital orderings in manganites that constitute the various phases in their phase diagrams. (a) The $d_{3x^2-r^2}$ or $d_{3y^2-r^2}$ orbitals are antiferromagnetically coupled in a plane but ferromagnetically connected in between the planes ; spins are ferromagnetically coupled in a plane with antiferromagnetic coupling in between the planes (b) Both linear combinations of $d_{3z^2-r^2}$ and $d_{x^2-y^2}$ orbitals and spins are ferromagnetically connected to each other (c) Alternate arrangement of holes and orbitals ($d_{3x^2-r^2}$ or $d_{3y^2-r^2}$) in a zigzag chain; ferromagnetic arrangement of spins on zigzag chains with different chains being antiferromagnetically coupled (d) Ferromagnetic arrangement of $d_{x^2-y^2}$ orbitals with spins being ferromagnetically coupled in a plane but antiferromagnetically coupled in between the planes (e) Ferromagnetic arrangement of $d_{3z^2-r^2}$ orbitals; ferromagnetic chains of spins antiferromagnetically aligned (e) Antiferromagnetic arrangement of spins throughout.

1.8.6 C-AFM insulator

Jahn-Teller effects produce an in-plane compressive strain that favors occupancies of the $d_{3z^2-r^2}$ orbitals and results in insulating C-AFM at very large dopings (see Figs. 1.9 (b) and 1.11 (e)). Here, ferromagnetic chains are antiferromagnetically coupled with the nearest-neighbors. The out-of-plane (z direction) double exchange is enhanced and the in-plane (xy plane) one gets suppressed.

1.8.7 G-AFM insulator phase

At $x = 1$, the e_g electron density is zero; the spin coupling between nearest neighbors is only due to the t_{2g} electrons and is hence fully AFM (see Fig. 1.11 (f)). The resulting state involves only Mn^{4+} ions and is insulating.

1.9 Plan of the thesis

The aim of this thesis is to show the importance of strong cooperative electron-lattice interactions (present in manganites) in bringing about the magnetoelectric effect and the ferromagnetic insulator phase in manganites. In chapter 2, we demonstrate in detail the occurrence of a giant magnetoelectric effect, invoking both analytical and numerical approaches. Next, chapter 3 deals with a localized-band model calculation that depicts the ferromagnetic-insulator phase in intermediate- and narrow-bandwidth manganites. Finally, chapter 4 summarizes the essential work done in manganite heterostructures in this thesis.

MAGNETOELECTRIC EFFECT IN PURE MANGANITE-MANGANITE HETEROSTRUCTURES

2.1 Introduction

In 1959, Dzyaloshinskii and Moriya described the mechanism behind the development of weak magnetism in antiferromagnets by the breaking of inversion symmetry [125,126]; this effect, known as the linear magnetoelectric (ME) effect, was observed in Cr_2O_3 . Thereafter, in the 1970's and 1980's, a large number of materials were discovered that showed ME effect, i.e., electric field producing a magnetization and magnetic field yielding an electric polarization. Furthermore, systems where both ferromagnetism and ferroelectricity coexisted, even in the absence of any external stimuli, were also detected. These materials belong to a class of materials that came to be known as multiferroics (MF), i.e., materials

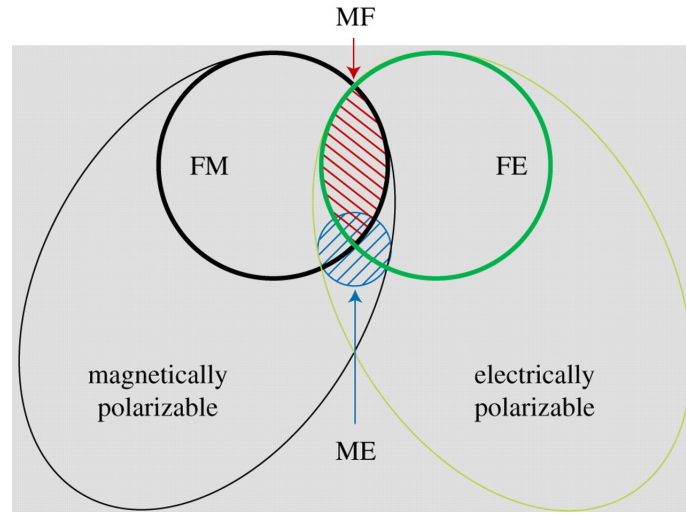


Figure 2.1: Schematic showing the relationship between ferromagnetic (FM), the ferroelectric (FE), multiferroic (MF) and magnetoelectric (ME) materials.(Adapted from Eerenstein *et al.*, Nature **442**, 759-765 (2006)).

where various ferroic orders such as ferroelectricity, ferromagnetism, ferroelasticity, and ferrotoroidicity co-existed. However, interest in this field took a backseat probably because the linear ME couplings, that the Dzyaloshinskii-Moriya effect predicted, were very small and very few MFs were found in nature. More so, still fewer materials were found that were both ME and MF as depicted in Fig. 2.1 .

There has been a revival in multiferroic research partly due to improved technology, discovery of new compounds (such as YMnO_3 , TbMn_2O_5), need for devices with strong magnetoelectric effect, etc [19]. Majority of the multiferroics studied are bulk materials where it is not yet fully clear why the magnetic and electric polarizations coexist poorly [127]. Nicola Spaldin specifically tried to reason why perovskite oxides did not show simultaneous occurrence of ferromagnetism and ferroelectricity. A phenomenological explanation would be that ferromagnetism in oxides resulted from the double exchange process (as mentioned in Sec. 1.5.1) that is essentially an itinerant-electron mechanism. Ferroelec-

tricty, on the other hand, occurs because of bound charges in the system since presence of free carriers would screen the charges thereby leading to a vanishing polarization. A more subtle way of looking at it in oxides would be that ferroelectricity in them is usually caused by the bonding of empty d^0 orbitals (in transition metal ions) with p orbitals (of nearby oxygens) leading to insulating behavior; ferromagnetism arises from non-zero electrons in the d orbitals (also in transition metal ions) and thus results in metallicity. With the advent of improved molecular-beam-epitaxy technology one can now grow oxide heterostructures with atomic-layer precision and explore the possibility of strong multiferroic phenomena as well as large interplay between ferroelectricity and magnetic polarization [128]. Oxides are a favorite choice to produce heterostructures because they exhibit different complex magnetic orderings in the bulk (see Sec. 1.5); furthermore, space inversion symmetry is already broken at the interface, which is the usual requirement for the occurrence of ferroelectricity.

Coupling between the charge and spin degrees of freedom is fascinating both from a fundamental viewpoint as well as from an applied perspective. Instead of employing currents and magnetic fields, controlling and manipulating magnetism with electric fields holds a lot of promise as the electric fields are easier to use in smaller dimensions and can potentially lower energy consumption in systems. There are numerous mechanisms for magnetoelectric effect; reviews for these can be found in Refs. [38–41, 129]. At the interface of a magnetic oxide and a ferroelectric/dielectric oxide, magnetoelectric effect of electronic origin has been predicted by some researchers. Upon application of an external electric field, not only the magnitude of moments can be changed [130, 131], but in some cases the very nature of magnetic ordering can be changed [132].

In spite of considerable efforts towards control of magnetization through electric fields in multiferroic bulk materials and heterostructures, obtaining strong magnetoelectric cou-

plings continues to be a challenge. Here, in this chapter, we predict a novel giant magnetoelectric effect, not at the interface, but away from it, in a pure manganite-manganite heterostructure (see Fig. 2.2). We present a plausible multiferroic phenomenon in manganite heterostructures and point out the associated unnoticed striking magnetoelectric effect. Cooperative electron-phonon interaction is shown to be key to understanding both multiferroicity and magnetoelectric effect in our oxide heterostructure. Here, we exploit the fact that manganites have various competing phases that are close in energy and that by using an external perturbation (such as an electric or a magnetic field) the system can be induced to alter its phase. We show that there is a charge redistribution (with a net electric dipole moment perpendicular to the interface) due to the optimization produced by the following two competing effects: (i) energy cost to produce holes on the LaMnO_3 (LMO) side and excess electrons on the CaMnO_3 (CMO) side; and (ii) energy gain due to electron-hole attraction (or electron-electron repulsion) on nearest-neighbor Mn sites induced by electron-phonon interaction. The charge polarization is akin to that of a pn-junction in semiconductors although the governing equations are different. The minority carriers, which leak across the interface of the heterostructure, produce ferromagnetic domains due to the ferromagnetic coupling (generated by electron-phonon interaction and double-exchange) between an electron-hole pair on adjacent sites. Since ferroelectricity and ferromagnetism have a common origin [i.e., minority carriers or holes (electrons) on LMO (CMO) side], there is a striking interplay between these two polarizations; consequently, when an external electric field is applied to increase the minority carriers, a giant magnetoelectric effect results.

2.2 General arguments for magnetoelectric effect in manganite heterostructures

We will argue that a large magnetoelectric effect is possible in LMO-CMO heterostructures by presenting below cohesive general theoretical points which take into account the essential features of manganites without invoking any particular model.

1) Kinetic energy (KE) is quite small because bare hopping is small (caused by lower tolerance factor [123], cation disorder, and compatibility of distortions [133]), electron-phonon coupling is strong, and system is quasi-two-dimensional (q2D).

2) Potential energy [from Coulomb interaction and nearest-neighbor (NN) particle-particle repulsion due to cooperative electron-phonon interaction] is much larger than KE; this leads to solid-type formation with electrons being rendered essentially immobile. Then, in each layer parallel to the interface (see Fig. 2.2), a solid with close-to-crystalline symmetry is formed with electrons being essentially site localized. The ground state is classical with number density at each site either 1 or 0 and the state of the system can be expressed by a single state in the occupation number basis. Due to strong cooperative electron-phonon interaction (CEPI) and not due to a sizeable KE, there is a propensity for electrons to migrate from the LMO side to the CMO side; this leads to a density gradient in the direction perpendicular to the interface (z-direction).

The fact that electrons are essentially site localized also follows when the treatment in Ref. [45, 46] is extended to our q2D system; then, only a localized polaronic band is relevant and the upper wide band cannot overlap with the lower narrow polaronic band. Additionally, the insulating behavior reported in Ref. [20] for $(\text{LaMnO}_3)_{2n}/(\text{SrMnO}_3)_n$ superlattice (when $n > 2$) further justifies the picture of negligible KE with the potential

energy determining the charge and spin order.

3) Because of Coulomb interaction between charges and strong CEPI, checkerboard-type crystal occurs in layers with densities close to 0.5 (based on point 2); due to symmetry considerations, checkerboard arrangement (including in the z-direction) is expected in layers next to the interface. This checkerboard feature is different from bulk manganites where charge and orbital stacking in z-direction occurs [and leads to the CE-type antiferromagnet (CE-AFM)]; this type of charge order was missed in works such as Ref. [32] because CEPI was not considered. Strong electron-phonon interaction produces NN electron-hole pair and produces between the pair a strong ferromagnetic interaction $[t^2 \cos^2(\theta/2)/E_{JT}]$ with E_{JT} being the cooperative Jahn-Teller energy, t the hopping term between the NN sites, and θ the angle between the core spins of the NN sites]. Hence, a ferromagnetic state is produced in the checkerboard. CE-type spin order is not supported because charge does not stack up in the z-direction; consequently, zigzag ferromagnetic chains in adjacent layers of the checkerboard will not be formed as such chains cannot be stacked up to produce between them magnetic coupling (such as antiferromagnetic) which is essential to the CE-type magnetism.

4) The model for magnetic interaction pertains to LMO-CMO heterostructure with localized holes. The CEPI retains essentially the same orbital texture as in LMO in regions away from the holes. Consequently, on the LMO side, the magnetic interaction is A-AFM in regions without holes; this interaction is generated through virtual hopping by localized electrons between NN sites that are Jahn-Teller compatible. When holes are present, since they are site localized, they only virtually hop to NN site and back and produce ferromagnetic coupling with NN electrons; this coupling is much stronger than A-AFM coupling. To go beyond the above picture (as was done rigorously in Ref. [134] for LaMnO_3), involves the daunting task of taking into account coupling between t_{2g} spins $[J_{t_{2g}}]$, two-band

model, Hubbard U , long-range Coulomb interaction, realistic Hund's coupling J_H ($< U$), and cooperative Jahn-Teller energy E_{JT} in a sizeable system (i.e., a lattice with about 100 sites or more) with LMO side being at finite hole density. We are not aware of such a comprehensive approach being reported.

5) Presence of site localized holes on the LMO side, produces FMI clusters due to formation of magnetic polarons. A hole will polarize nearest-neighbor electrons (and realistically speaking, next-nearest-neighbor and next-to-next-nearest-neighbor electrons as well) through virtual hopping, thereby producing a magnetic polaron. A collection of interacting magnetic polarons will produce a FMI region. This picture is in tune with FMI region being a generic feature of manganites at moderate dopings ($0.1 \lesssim x \lesssim 0.2$); see Ref. [45, 46] for a similar FMI picture in the bulk. It should be noted that FMI regions are present in moderately-doped manganites that are narrow band ($\text{Pr}_{1-x}\text{Ca}_x\text{MnO}_3$), intermediate band ($\text{La}_{1-x}\text{Ca}_x\text{MnO}_3$) and wide band ($\text{La}_{1-x}\text{Sr}_x\text{MnO}_3$). Increasing the number of holes on the LMO side, using a fairly large electric field, increases the number of aligned FMI clusters, thereby producing a large magnetoelectric effect. It is important to note that the applied electric field changes the magnetization sizeably in the bulk of LMO away from the interface while leaving the polarization at the interface essentially unaltered. Here, it should be noted that the FMI phase, which is key to the magnetoelectric effect, is not captured in the phase diagram of the bulk LCMO reported in Fig. 2 of Ref. [32]; this is possibly because small values of $\lambda = \sqrt{2E_{JT}/t}$ were chosen and cooperativity in the electron-phonon interaction was ignored.

2.3 Analytic treatment

We will begin our treatment of the pure manganite-manganite heterostructure by considering a simple analytic picture in this section and leave a more detailed numerical approach to the next section. Our (Insulator)/(LaMnO₃)_n/Interface/(CaMnO₃)_n/(Insulator) heterostructure is depicted in Fig. 2.2; the treatment in this section involves odd number of MnO₂ planes. The MnO₂ plane, contained in the Interface at the center, has LaO on one side and CaO on the other side. The MnO₂ plane in the center has 0.5 electron per Mn site. The arrangement of the heterostructure is as follows: Ins./(LaO-MnO₂)_n/(LaO-MnO₂-CaO)/(MnO₂-CaO)_n/Ins. where (LaO-MnO₂-CaO) represents the Interface. The above arrangement will not lead to polar catastrophe (see Sec 1.2) as any excess charge at the Ins./LaO interface can be neutralized by a gate potential. Alternately, the Ins./LaO interface on the left-hand side can be replaced by Ins./(La_{1/2}Ca_{1/2}O) interface; then, no excess charge results.

2.3.1 Polaronic Hamiltonian

In our heterostructure depicted in Fig. 2.2, due to charge leaking across the LMO-CMO interface, we expect different states of the phase diagram of La_{1-x}Ca_xMnO₃ (LCMO) at different cross-sections perpendicular to the growth direction. Since far from the LMO-CMO interface the material properties must be similar to those in the bulk, we expect the $x = 0$ phase at the Insulator-LMO interface and the $x = 1$ phase at the other end involving CMO-Insulator interface. Considering majority of the LCMO phase diagram (including the end regions near $x = 0$ and $x = 1$) is taken up by insulating phases, since band width is significantly diminished at strong electron-phonon coupling, and because the heterostruc-

tures are q2D, we expect that there is no effective transport in the direction normal to the oxide-oxide interface (i.e., the z-direction). Then, for analyzing the charge distribution normal to the interface, the starting polaronic Hamiltonian is assumed to comprise of localized electrons and have the following phenomenological form:

$$H_{\text{pol}} \sim - \sum_{j,\delta} \left[\gamma_{\text{ep}}^1 g^2 \omega_0 + \frac{\gamma_{\text{ep}}^2 t_{j,j+\delta}^2}{g^2 \omega_0} \right] n_j (1 - n_{j+\delta}), \quad (2.1)$$

where the first coefficient $\gamma_{\text{ep}}^1 g^2 \omega_0$ is due to electron-phonon interaction and represents nearest-neighbor electron-electron repulsion brought about by incompatible distortions of nearest-neighbor oxygen cages surrounding occupied Mn ions. The pre-factor γ_{ep}^1 can depend on the phase – for instance, in the regime of C-type antiferromagnet (C-AFM) in LCMO, γ_{ep}^1 is expected to be large because occupancy of neighboring d_{z^2} orbitals is inhibited in the z-direction; while in the regime of A-AFM (corresponding to undoped LaMnO₃), γ_{ep}^1 is expected to be weaker because of compatible Jahn-Teller distortions on neighboring sites. Here, we will assume for simplicity that γ_{ep}^1 is concentration independent and that $0.1 \leq \gamma_{\text{ep}}^1 \leq 1$. Next, the coefficient $\gamma_{\text{ep}}^2 t^2 / (g^2 \omega_0)$ results from processes involving hopping to nearest-neighbor and back and is present even when we consider the simpler Holstein model [135] or the Hubbard-Holstein model [136]. The pre-factor γ_{ep}^2 varies between 1/2 (for non-cooperative electron-phonon interaction) and 1/4 (since for cooperative breathing mode in one-dimensional chains $\gamma_{\text{ep}}^2 = 1/3$, which should be more than in C-chains) [137]. Now, even within the two-band picture of manganites in Ref. [45, 46], the electrons in the localized polaronic band contribute the term $t^2 / g^2 \omega_0$; the broad band (due to undistorted states that are orthogonal to the polaronic states) is an upper band whose band width is reduced due to the two-dimensional (2D) nature of the system and does not overlap with the polaronic band to produce conduction even at carrier con-

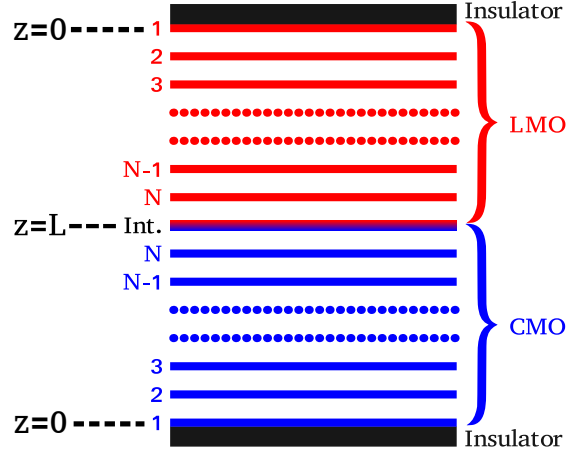


Figure 2.2: Schematic showing the symmetric manganite-manganite heterostructure (Insulator)/(LaMnO₃)_N/Interface/(CaMnO₃)_N/(Insulator). Each of the labeled N layers on both LMO (LaMnO₃) and CMO (CaMnO₃) sides contain manganese-oxide (MO) layers.

centrations corresponding to $0.2 \lesssim x \lesssim 0.5$. Furthermore, although n_j is the total number in both the orbitals at site j , it can only take a maximum value of 1 due to strong on-site electron-electron repulsion and strong Hund's coupling. Next, to make the above Hamiltonian furthermore relevant for manganites, one needs to consider Hund's coupling between core t_{2g} spins and itinerant e_g electrons. This leads to invoking the double exchange mechanism for transport. Then, the hopping term $t_{i,j}$ between sites i and j in Eq. (2.1) is modified to be $t_{i,j} \sqrt{0.5[1 + (\mathbf{S}_i \cdot \mathbf{S}_j / S^2)]} = t_{i,j} \cos(\theta_{ij}/2)$ with \mathbf{S}_i being the core t_{2g} spin at site i and θ_{ij} being the angle between \mathbf{S}_i and \mathbf{S}_j . The term $\gamma_{\text{ep}}^2 t_{j,j+\delta}^2 \cos^2(\theta_{ij}/2) / (g^2 \omega_0)$ in Eq. (2.1) produces a strong ferromagnetic coupling between the spins at site j and site $j + \delta$ and this dominates over any superexchange coupling between the two spins.

2.3.2 Charge Profile

As already stated in Sec. 2.2, the kinetic term is small due to polaronic effects and the q2D nature of the system. While the complete absence of kinetic energy would indeed lead to the electron charge density following the ionic charge, in the presence of a small kinetic term the charge profile will redistribute. We just assume that the kinetic contribution to the energy is small compared to the other terms, not that the charges are fully immobilized.

The following are two competing terms in the potential energy which are the dominant terms that produce charge distribution:

- 1) Due to cooperative electron-phonon interactions, there is a repulsive interaction between electrons on adjacent sites. This pushes electrons from LMO side to CMO side.
- 2) There is attractive interaction between an electron on an Mn site and the positive ionic charge of that unit cell. This attraction holds back the electrons on the LMO side.

Now, when the electrons move from the LMO side to the CMO side, there is a net positive charge on the LMO side and a net negative charge on the CMO side. The separation energy of these net positive and net negative charges can be approximated as the energy of a capacitor $Q^2/2C_{\text{cap}}$ where charge $Q \sim N_{\text{el}}$ (with N_{el} being the transferred electrons) and capacitance $C_{\text{cap}} \propto A_{\text{int}}/d$ with A_{int} being the interface area and d the separation; this energy (i.e., $Q^2/2C_{\text{cap}}$) has to be balanced by the nearest-neighbor repulsion energy ($\sim N_{\text{el}} g^2 \omega_0$) due to electron-phonon interaction. Now, if Q/A_{int} is independent of the system size and d is only a few lattice spacings, then $Q^2/2C_{\text{cap}}$ can be comparable to $\sim N_{\text{el}} g^2 \omega_0$; thus, macroscopic number of charges, from a few layers near the interface, can be transferred across the interface. Hence, ideally the heterostructure should comprise of only a few layers so that a large part of the system can contribute to the multiferroicity and also the magnetoelectric effect.

To obtain the charge distribution, we ignore the effect of superexchange interaction in the starting effective Hamiltonian in Eq. (2.1) because its energy scale is significantly smaller than the polaronic energy term $2g^2\omega_0$. For a localized system, we only need to minimize the interaction energy which is a functional of the electronic density profile. The Coulombic interaction energy resulting from the electrons leaking from the LMO side to the CMO side, is taken into account by ascribing an effective charge $+1$ (hole) to the LMO unit cell (centered at the Mn site) that has donated an e_g electron from the Mn site and an effective charge -1 (electron) to the CMO unit cell (centered at the Mn site) that has accepted an e_g electron at the Mn site. The Coulombic energy that results is due to the interactions between these ± 1 effective charges. The net positive charge on the LMO side and the net negative charge on the CMO side will produce a charge polarization (or inversion asymmetry). Since the ferroelectric dipole is expected to be in the direction perpendicular to the oxide-oxide (LMO-CMO) interface, we assume that the density is uniform in each layer for calculating the density profile as a function of distance z from the insulator-oxide interface. The Coulombic interaction energy per unit area due to leaked charges is the same for both LMO and CMO regions and is given, in the continuum approximation, to be

$$E_{\text{coul}} = \frac{1}{8\pi\epsilon} \int_0^L dz D(z)^2, \quad (2.2)$$

where $D(z)$ is the electric displacement and is given by

$$D(z) = \pm \left[-\epsilon E_{\text{ext}} + \int_0^z dy 4\pi e \rho(y) \right], \quad (2.3)$$

with $+$ ($-$) sign for LMO (CMO) side. Furthermore, $\rho(z)$ is the density of minority charges (i.e., holes on LMO side and electrons on SMO side), e the charge of a hole, ϵ the dielectric

constant, E_{ext} an external electric field along the z -direction, and L the thickness of the LMO (CMO) layers.

The ground state energy per unit area [corresponding to the effective Hamiltonian of Eq. (2.1)] can be written, in the continuum approximation, as a functional of $\rho(z)$ for both LMO and CMO as follows:

$$E_{\text{pol}} = - \left[\gamma_{\text{ep}}^1 g^2 \omega_0 + \frac{\gamma_{\text{ep}}^2 t^2}{g^2 \omega_0} \right] \zeta \int_0^L dz \rho(z) [1 - a^3 \rho(z)], \quad (2.4)$$

where $\zeta = 6$ is the coordination number and a is the lattice constant. In arriving at the above equation we have approximated $n_{i+\delta} + n_{i-\delta} \approx 2n_i$. Furthermore, for the ground state, the minority charges will completely polarize the neighboring majority charges.

We will now minimize the total energy given below

$$E_{\text{Total}} = 2E_{\text{pol}} + 2E_{\text{coul}}, \quad (2.5)$$

by setting the functional derivative $\delta E_{\text{Total}} / \delta \rho(z) = 0$. This leads to the following equation

$$0 = -C_1 [1 - 2a^3 \rho(z)] + 2C_2 \int_z^L dy \left[-\tilde{E}_{\text{ext}} + \int_0^y dx \rho(x) \right], \quad (2.6)$$

where $C_1 \equiv \left[\gamma_{\text{ep}}^1 g^2 \omega_0 + \frac{\gamma_{\text{ep}}^2 t^2}{g^2 \omega_0} \right] \zeta$; $C_2 \equiv 2\pi e^2 / \epsilon$; and $\tilde{E}_{\text{ext}} \equiv \epsilon E_{\text{ext}} / (4\pi e)$. The above equation, upon taking double derivative with respect to z , yields

$$C_1 a^3 \frac{d^2 \rho(z)}{dz^2} - C_2 \rho(z) = 0. \quad (2.7)$$

The above second-order differential Eq. (2.7) and Eq. (2.6) admit the solution

$$\rho(z) = \frac{1}{2a^3} \frac{\cosh(\xi z)}{\cosh(\xi L)} + \xi \tilde{E}_{\text{ext}} \frac{\sinh[\xi(L - z)]}{\cosh(\xi L)}, \quad (2.8)$$

where $\xi = \sqrt{C_2/(C_1 a^3)}$. It is important to note that, for the manganese-oxide (MO) layer at the LMO-CMO interface (i.e., at $z = L$), the density is 0.5 electrons/site and that it is independent of the applied external electric field and the system parameters. Now, since each Mn site in the interface layer belongs to a unit cell that is half LMO and half CMO, one expects the density per site to be 0.5. Additionally, as the distance from the LMO-CMO interface increases, we observe from Eq. (2.8) as well as from Figs. 2.3 and 2.4 that for smaller values of C_1 , the density falls more rapidly while the density change due to electric field rises faster. Furthermore, for realistic values of the parameters, the charge density rapidly changes as we move away from the oxide-oxide interface (i.e., after only a few layers from the interface) and attains values close to the bulk value [as illustrated in Figs. 2.3(a) and 2.4(a)]. Lastly, as required for zero values of the external field E_{ext} , we get $\rho(0) \rightarrow 0$ when $L \rightarrow \infty$. Thus, although we used the continuum approximation, our obtained density profile is qualitatively realistic as it has the desired values at the extremes $z = L$ and $z = 0$ with the density away from the LMO-CMO interface rapidly falling for not too large values of ϵ .

The density profiles for both LMO and CMO sides depend only on ϵ , C_1 and E_{ext} . For our calculations displayed in Fig. 2.3, we used the following values for the parameters: $a = 4$ Å; $\epsilon = 20$; $E_{\text{ext}} = 300$ kV/cm and 400 kV/cm; and $C_1 = 0.24$. For Fig. 2.4, we employed $E_{\text{ext}} = 100$ kV/cm and $C_1 = 0.31$, with the values for a and ϵ being the same as in Fig. 2.3. The values of C_1 in Figs. 2.3 and 2.4 were chosen based on $\omega_0 = 0.07$ eV; $g = 2$; and $t = 0.1$ eV.

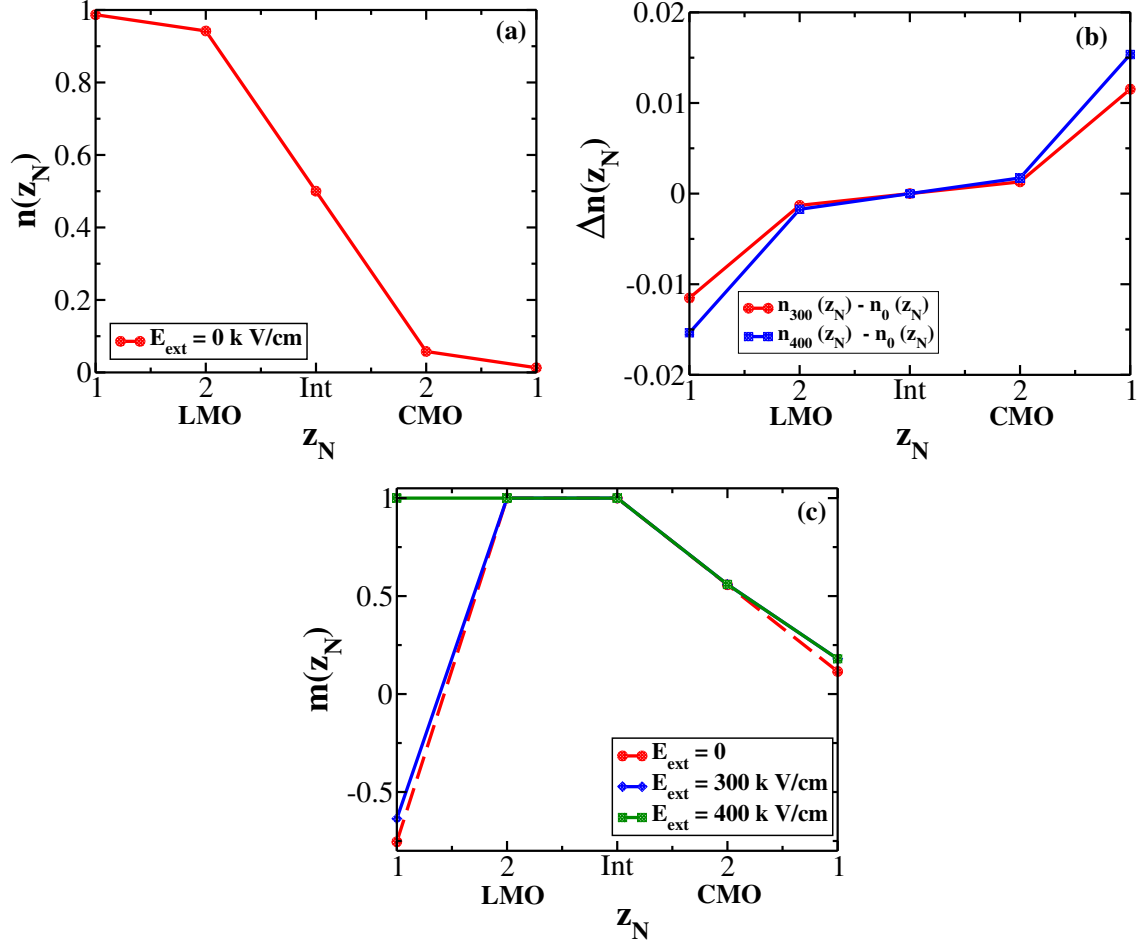


Figure 2.3: Electronic charge density $n(z_N)$ and per-site magnetization $m(z_N)$ (of t_{2g} spins normalized to unity) in various manganese-oxide layers of a (Insulator)/(LaMnO₃)₂/Interface/(CaMnO₃)₂/Insulator heterostructure for $a = 4$ Å, $\epsilon = 20$, and $C_1 = 0.24$. Figures are for (a) $n(E_{\text{ext}} = 0$ kV/cm); (b) $\Delta n = n(E_{\text{ext}} = 300/400$ kV/cm) $- n(E_{\text{ext}} = 0$ kV/cm); and (c) $m(z_N)$ at $E_{\text{ext}} = 0$ kV/cm, 300 kV/cm, and 400 kV/cm. MO layer 1 on the LMO side undergoes spin reversal when $E_{\text{ext}} = 400$ kV/cm is applied.

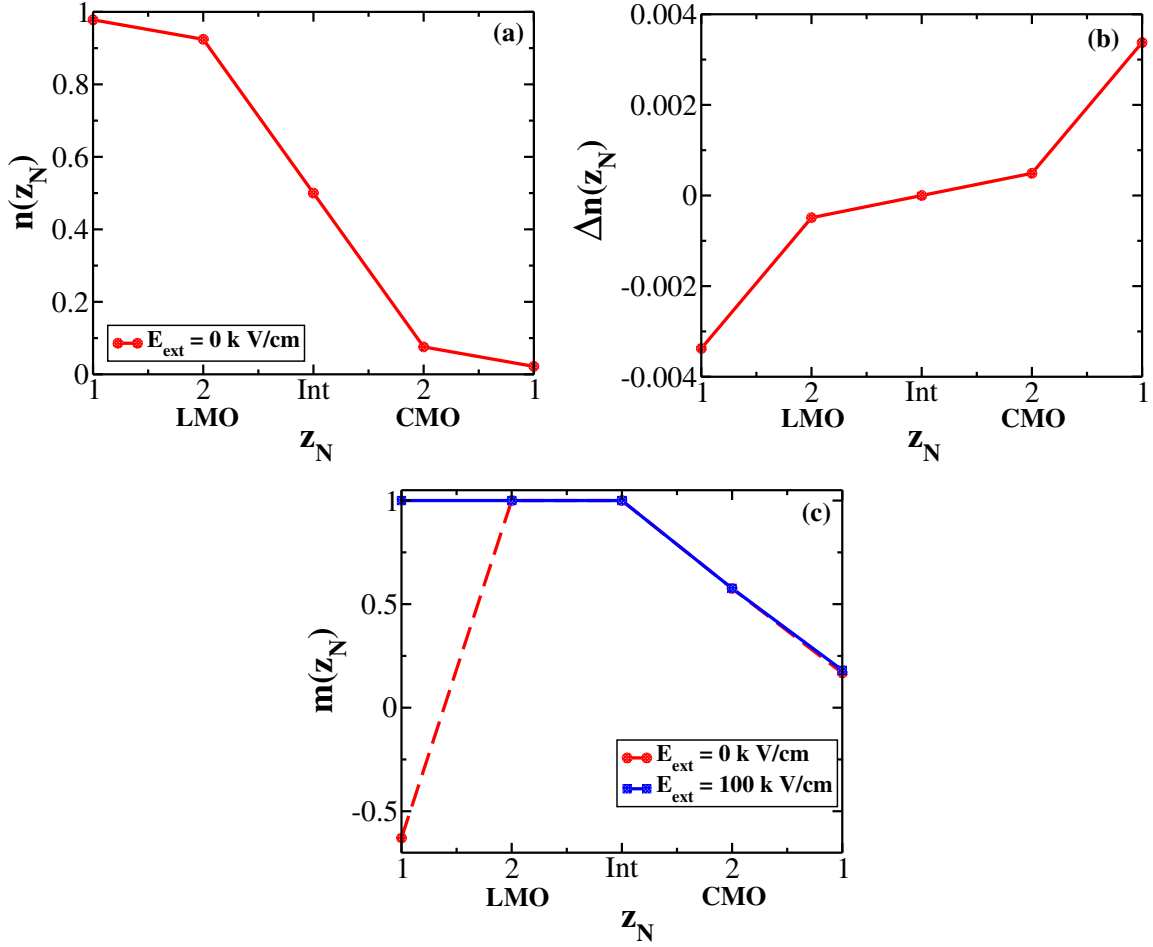


Figure 2.4: Electronic charge density $n(z_N)$ and per-site magnetization $m(z_N)$ (of normalized-to-unity t_{2g} spins) in various manganese-oxide layers of a (Insulator)/(LaMnO₃)₂/Interface/(CaMnO₃)₂/(Insulator) heterostructure for $a = 4 \text{ \AA}$, $\epsilon = 20$, and $C_1 = 0.31$. Plots pertain to (a) $n(E_{\text{ext}} = 0 \text{ kV/cm})$; (b) $\Delta n = n(E_{\text{ext}} = 100 \text{ kV/cm}) - n(E_{\text{ext}} = 0 \text{ kV/cm})$; and (c) $m(z_N)$ at $E_{\text{ext}} = 0 \text{ kV/cm}$ and $E_{\text{ext}} = 100 \text{ kV/cm}$. The LMO side becomes completely ferromagnetic when $E_{\text{ext}} = 100 \text{ kV/cm}$ is applied.

2.3.3 Magnetization distribution

We will now obtain the magnetization for a heterostructure by considering its lattice structure unlike the case for the density profile where a continuum approximation was made.

Thus we can take into account the possibility of antiferromagnetic (AFM) order besides being able to consider ferromagnetic (FM) order.

First, based on Ref. [9], we note that the bulk $\text{La}_{1-x}\text{Ca}_x\text{MnO}_3$ (below the magnetic transition temperatures) is A-AFM for $0 \leq x \lesssim 0.1$ and a ferromagnet for $0.1 \lesssim x \lesssim 0.5$. Hence, we model the LMO side of the heterostructure as an A-AFM when hole concentrations are small; whereas at higher concentrations of holes which is less than 0.5, the holes dictate the magnetic order by forming magnetic polarons that polarize the A-AFM. Next, we note that for $0.5 \lesssim x \lesssim 1.0$, the $\text{La}_{1-x}\text{Ca}_x\text{MnO}_3$ bulk system is always an antiferromagnet. Thus, from a magnetism point-of-view, the magnetic moment on the CMO side of the heterostructure is expected to be zero except in the vicinity of the interface where (due to proximity effect) it will be a ferromagnet and can be modeled using a percolation picture as will be explained in the subsequent section. Given the above scenario, as can be expected, we find that the ferromagnetic region on the LMO side can be drastically enhanced (at the expense of the A-AFM region) by an electric field inducing holes on the LMO side. On the other hand, the electric field has only a small effect on the percolating ferromagnetic cluster that is adjacent to the oxide-oxide interface on the CMO side.

2.3.3.1 CMO side

We will first consider the CMO side and show that the magnetization decays as we move away from the LMO-CMO interface. We derive below the largest FM domain; this domain percolates from the LMO-CMO interface. On account of nearest-neighbor repulsion (as given in Eq. (2.1)), the interface (which is half-filled) has e_g electrons on alternate sites. In fact, to minimize the interaction energy, on the CMO side we take the e_g electrons to be in one sublattice only which will be called e_g -sublattice; the other unoccupied sublattice will be called the u -sublattice. On account of virtual hopping, an e_g electron polarizes all its

neighboring sites that do not contain any e_g electrons and forms a magnetic polaron. Thus we observe that the half-filled interface will be fully polarized and that there will be an FM cluster that begins at the interface and percolates to the layers away from the interface on the CMO side. For instance, in the layer next to the oxide-oxide interface, all the e_g electrons are in the same sublattice (the e_g -sublattice) and are next to the empty sublattice (i.e., sublattice unoccupied by e_g electrons) of the interface and hence are ferromagnetically aligned with the interface. Similarly, again in the layer adjacent to LMO-CMO interface, all the sites in the other sublattice (i.e., the u -sublattice) are empty and have the same polarization as the sites occupied by the e_g electrons at the interface.

We will now identify the equations governing the ferromagnetic cluster percolating from the interface. Let z_N be the z -coordinate of the N^{th} 2D MO layer with N being the index measured from the Insulator-CMO interface (as shown in Fig. 2.2). Furthermore, we define $x_N^{e_g}$ (x_N^u) as the concentration of polarized sites that belong to the spanning cluster and these sites are a subset of the sites in the e_g -sublattice (u -sublattice) in the N^{th} 2D MO layer. Then, the factor $(1 - 2x_N^{e_g}) [(1 - 2x_N^u)]$ represents the probability of a site that belongs to the e_g -sublattice (u -sublattice) in layer N but is not part of the spanning polarized cluster. Now, the probability that a site, occupied (unoccupied) by an e_g electron, contributes to the FM cluster is equal to the probability of finding the site occupied (unoccupied) multiplied by $1-P$ where P is the probability that none of the adjacent sites that are in the u -sublattice (e_g -sublattice) belong to the percolating cluster. Therefore, we obtain the following set of coupled equations for the spanning cluster:

$$x_N^{e_g} = \rho(z_N)[1 - (1 - 2x_{N-1}^u)(1 - 2x_N^u)^4(1 - 2x_{N+1}^u)], \quad (2.9)$$

$$x_N^u = 0.5[1 - (1 - 2x_{N-1}^{e_g})(1 - 2x_N^{e_g})^4(1 - 2x_{N+1}^{e_g})]. \quad (2.10)$$

The boundary conditions involving layer 1 are

$$x_1^{e_g} = \rho(z_1)[1 - (1 - 2x_1^u)^4(1 - 2x_2^u)], \quad (2.11)$$

and

$$x_1^u = 0.5[1 - (1 - 2x_1^{e_g})^4(1 - 2x_2^{e_g})], \quad (2.12)$$

while those for the LMO-CMO interface are $x_{\text{Int}}^{e_g} = x_{\text{Int}}^u = 0.5$.

2.3.3.2 LMO side

Next, we will show that the LMO side with only a few layers, for some realistic values of parameters, can have a sizeable change in the magnetism when a large electric field is applied and thus can be exploited to obtain a giant magneto-electric effect. Similar to the bulk situation in LaMnO_3 [134, 138–140] in our heterostructure as well, we assume that two spins on any adjacent sites in each MO layer have a ferromagnetic coupling $J_{xy} = 1.39$ meV; whereas, any two neighboring spins on adjacent layers have an anti-ferromagnetic coupling $J_z = 1.0$ meV. On the other hand, for an electron and a hole on neighboring sites either in the same MO layer or in adjacent MO layers, (due to virtual hopping of electron between the two sites) there is a strong ferromagnetic coupling $J_{eh} = \gamma_{\text{ep}}^2 t^2 / (g^2 \omega_0) \gg J_{xy}$ [45, 46]. In our calculations, as long as the ratio of J_{xy}/J_z is taken as fixed and J_{eh} is the significantly dominant coupling, we get the same magnetic picture.

In a LMO side with a few MO layers, to demonstrate the possibility of large magnetization change upon the application of a large external field, we assume that the LMO-CMO interface and all MO layers up to layer M are completely polarized. Next, we assume that MO layers M and M-1 have low density of holes so that there is a possibility that spins in

MO layer M-1 are not aligned with the block of MO layers starting from the LMO-CMO interface and up to layer M. We then analyze the polarization of MO layer M-1 by comparing the energies for the following two cases: (i) layers M-1 and M are antiferromagnetically aligned with the holes in layers M and M-1 inducing polarization only on sites that are adjacent to the holes; and (ii) MO layer M-1 is completely polarized and aligned with Layer M.

In a few-layered heterostructure (Ins.)/(LaMnO₃)₂/Int./(CaMnO₃)₂/(Ins.), for $C_1 = 0.24$ eV [as shown in Fig. 2.3(c)] and for $C_1 = 0.31$ [as in Fig. 2.4(c)], we obtain a striking magneto-electric effect. For zero external field, when $M = 2$ is considered, case (i) (mentioned above) has lower energy, i.e., layer 1 is antiferromagnetically coupled to layer 2. On the other hand, when a strong electric field (~ 100 kV/cm for $C_1 = 0.24$ and ~ 400 kV/cm for $C_1 = 0.31$) is applied, MO layer 1 (due to increased density of holes) becomes completely polarized and ferromagnetically aligned with the rest of the layers (i.e., MO layer 2 and the oxide-oxide interface) on the LMO side. Thus, we get a giant magneto-electric effect! We have considered C_1 values ranging from 0.24 to 0.31 and obtained magnetoelectric effect for various threshold electric field values. Changing C_1 is physically equivalent to changing the effective nearest-neighbor electron-hole attraction. Thus a smaller C_1 value of 0.24 indicates a lower effective nearest-neighbor electron-electron repulsion which requires a larger external electric field strength of 400 kV/cm to generate enough holes on the LMO side and, consequently, flip the magnetization of layer 1. Obviously, for the larger value $C_1 = 0.31$, sufficient number of holes are already present in the LMO system and layer 1 becomes ferromagnetic when a smaller E_{ext} ($= 100$ kV/cm) is applied. At still larger values of C_1 , i.e., $C_1 \geq 0.32$, the LMO side is completely ferromagnetic even in the absence of an external field.

2.4 Numerical Approach

Here, in this section, we construct a detailed 2D model Hamiltonian and study it numerically for the charge and magnetic profiles and the coupling between them. Our system $(\text{Ins.})/(\text{LaMnO}_3)_n/\text{Int.}/(\text{CaMnO}_3)_n/(\text{Ins.})$ depicted in Fig. 2.2, for the treatment in this section, involves even number of MnO_2 planes. Here we can have the following arrangement:

$$\text{Ins.}/(\text{LaO-MnO}_2)_n/(\text{La}_{1/2}\text{Ca}_{1/2}\text{O})/(\text{MnO}_2\text{-CaO})_n/\text{Ins.}$$

Here, the Interface is composed of $\text{La}_{1/2}\text{Ca}_{1/2}\text{O}$ (which is non-magnetic) and has 0.5 +ve charge per unit $\text{La}_{1/2}\text{Ca}_{1/2}\text{O}$. There is no polar catastrophe as any excess charge at the $\text{Ins.}/\text{LaO}$ interface can be neutralized by a gate potential. Each unit cell on LMO side, comprising of $[(\text{LaO})_{1/2}\text{MnO}_2(\text{LaO})_{1/2}]$, is charge neutral.

2.4.1 Model Hamiltonian

In a q2D heterostructure (involving only a few 2D layers of both manganites), as mentioned in Sec. 2.3, we expect only a single narrow-width polaronic band to be relevant [141, 142]. For our numerical treatment of a 2D lattice (with l_1 rows and l_2 columns), we employ the following one-band Hamiltonian:

$$H = H_{\text{KE}} + H_{\text{pol}}^{\text{mf}} + H_{\text{SE}} + H_{\text{coul}} + H_{\text{V}}. \quad (2.13)$$

The kinetic energy term H_{KE} is given by

$$H_{\text{KE}} = -te^{-g^2} \sum_{\langle i,j \rangle} \left[\cos\left(\frac{\theta_{ij}}{2}\right) c_i^\dagger c_j + \text{H.c.} \right], \quad (2.14)$$

where t is the hopping amplitude that is attenuated by the electron-phonon coupling g and c_j is the e_g electron destruction operator; furthermore, $\cos(\theta_{ij})$ is the modulation due to infinite Hund's coupling between the itinerant electrons and the localized t_{2g} spins with θ_{ij} being the angle between two localized $S = 3/2$ spins at sites i and j [115, 143]. For more details about the theory of Double exchange, refer Sec. 1.5.1. As mentioned in Ref. [141, 142], in a two-band picture, for intermediate-bandwidth systems such as LCMO, the upper broad band becomes relevant in three dimensions (3D) at lower temperatures. In q2D, the upper band does not overlap with the lower polaronic band where essentially all the electrons are localized; in q2D, width of the upper band is two-thirds the width of the upper band in 3D. In narrow-band systems such as $\text{Pr}_{1-x}\text{Ca}_x\text{MnO}_3$ (PCMO), no metallic nature is observed for $x < 0.5$; we infer that the upper band in PCMO does not overlap with the lower band even at low temperatures. The width of the upper band of PCMO in 3D is about two-thirds that of LCMO in 3D. Thus, we are justified in considering a very narrow single band in our LMO-CMO heterostructure.

The second term $H_{\text{pol}}^{\text{mf}}$ in Eq. (2.13) is the mean-field version of H_{pol} in Eq. (2.1) and is expressed as

$$H_{\text{pol}}^{\text{mf}} = \left[\gamma_{\text{ep}}^1 g^2 \omega_0 + \frac{\gamma_{\text{ep}}^2 t^2 \cos^2 \left(\frac{\theta_{ij}}{2} \right)}{g^2 \omega_0} \right] \times \sum_{i,\delta} [n_i - 2n_i \langle n_{i+\delta} \rangle + \langle n_i \rangle \langle n_{i+\delta} \rangle], \quad (2.15)$$

where $\langle n_i \rangle \equiv \langle c_i^\dagger c_i \rangle$ refers to the mean number density at site i . A derivation of $H_{\text{KE}} + H_{\text{pol}}$ is given in Ref. [137]; however, for simplicity, here we have ignored the effect of next-nearest-neighbor hopping. The next term H_{SE} in Eq. (2.13) pertains to the superexchange [144] term which generates A-AFM in LaMnO_3 and G-AFM in CaMnO_3 ; thus on the

LaMnO₃ side, it is given by

$$H_{\text{SE}}^{\text{lmo}} = -J_{\text{xy}} \sum_{\langle i,j \rangle_{\text{xy}}} \cos(\theta_{ij}) + J_z \sum_{\langle i,j \rangle_z} \cos(\theta_{ij}), \quad (2.16)$$

while on the CaMnO₃ side, we express it as

$$H_{\text{SE}}^{\text{cmo}} = J_z \sum_{\langle i,j \rangle} \cos(\theta_{ij}). \quad (2.17)$$

In the above superexchange expressions, the magnitude of the $S = 3/2$ spins is absorbed in the superexchange coefficients J_{xy} and J_z . Further theoretical background for superexchange can be found in Sec. 1.5.2. Our magnetic picture reproduces the bulk behavior in LMO and CMO in regions away from the holes. In bulk LCMO, at intermediate doping $0.1 < x < 0.5$, the region is ferromagnetic; this can be explained as due to an electron and a hole on adjacent sites being ferromagnetically coupled (see Ref. [141, 142]). Similar to the bulk, in our heterostructure as well, a strong ferromagnetic interaction exists between a NN electron-hole pair; this ferromagnetic interaction is much stronger than the magnetic interactions corresponding to A-AFM and G-AFM. Thus (unlike in Ref. [32], where the boundary conditions are enforced to be A-AFM on LMO side and G-AFM on CMO side), we assume A-AFM on LMO side and G-AFM on CMO side in regions that do not contain any minority carriers (i.e., holes on LMO side and electrons on CMO side).

In Eq. (2.13), the Coulomb interaction is accounted for through the term H_{coul} as follows:

$$H_{\text{coul}} = V_s \sum_i n_i + \alpha t \sum_{i \neq j} \left[n_i \left(\frac{\langle n_j \rangle - Z_j}{|\vec{r}_i - \vec{r}_j|} \right) - \frac{\langle n_i \rangle \langle n_j \rangle}{2|\vec{r}_i - \vec{r}_j|} \right], \quad (2.18)$$

where the first term on the right hand side (RHS) is actually the on-site Coulomb interaction between an electron and a positive ion that yields the binding energy of an electron and is therefore applicable only to the LMO side. The remaining term on the RHS of Eq. (2.18), denotes long-range, mean-field Coulomb interactions between electrons as well as between electrons and positive ions. Here, Z_j represents the positive charge density operator with a value of either 1 or 0 and $|\vec{r}_i - \vec{r}_j|$ is the distance between lattice sites i and j . Furthermore, the dimensionless parameter $\alpha = \frac{e^2}{4\pi\epsilon a t}$ determines the strength of the Coulomb interaction. Lastly, in Eq. (2.13), the term H_V represents the potential felt at various sites due to an externally applied potential difference (V_{ext}) between the two insulator edges (see Fig. 2.2):

$$H_V = V_{\text{ext}} \sum_{I=1}^{l_2} \sum_{K=1}^{l_1} \left[1 - \left(\frac{I-1}{l_2-1} \right) \right] n_{I+(K-1)l_2}, \quad (2.19)$$

where I represents the layer (or column) index with l_2 denoting the number of layers, i.e., the number of sites in the z -direction; K represents the row index with l_1 denoting the number of rows, i.e., the number of sites in a layer.

2.4.2 Calculation procedure

We consider a 2D lattice involving a few layers (columns) of LMO and CMO and study magnetoelectric effect. The lattice does not have periodicity in the direction normal to the interface of the heterostructure (i.e., the z -direction). On the other hand, to mimic infinite extent in the direction parallel to the interface of the heterostructure, we assume periodic boundary condition in that direction. We employ classical Monte Carlo with Metropolis update algorithm to obtain the charge and magnetic profiles for our 2D lattice. To tackle the difficult problem of several local minima that are close in energy, we take recourse

to the simulated annealing technique. To arrive at a reasonable charge profile at energy scales much larger than the superexchange energy scale, we treat the problem classically (i.e., fully electrostatically) by considering only the Coulomb term (H_{coul}), the external-potential term (H_V), and the electron-phonon-interaction term [$H_{\text{pol}}^{\text{mf}}(\theta_{ij} = 0)$] as these are the dominant energy terms in the Hamiltonian. The Coulomb term is subjected to mean-field analysis (as mentioned before) and the system generated potential $\alpha t \sum_{i \neq j} \left\{ \frac{\langle n_j \rangle - Z_j}{|\vec{r}_i - \vec{r}_j|} \right\}$ [145] in Eq. (2.18) is solved self-consistently. This is equivalent to solving the Poisson equation [146].

Next, to arrive at the final charge and magnetic configurations, we treat the system quantum mechanically by starting with an initial configuration comprising of the charge configuration generated classically (by the above procedure) and an initial random spin configuration. We now consider the full Hamiltonian, where hopping term (H_{KE}) and spin interaction energy act as perturbation to the classical dominant energy terms [H_{coul} , H_V , and $H_{\text{pol}}^{\text{mf}}(\theta_{ij} = 0)$], thereby allowing for a small change in the number density profile and determine the concomitant magnetic profile. For the classical t_{2g} spins $\vec{S}_i = (\sin \theta_i \cos \phi_i, \sin \theta_i \sin \phi_i, \cos \theta_i)$ that are normalized to unity, the $\cos(\theta)$ and ϕ values are binned in the intervals $(-1, 1)$ and $(0, 2\pi)$ respectively with equally spaced 40 values of $\cos(\theta)$ and 80 values of ϕ , hence yielding a total of 3200 different possibilities.

In our calculations, we employ the parameter values $t = 0.1$ eV, $g = 2$ & 2.2 , and $\omega_0 = 0.07$ leading to a small parameter value $\frac{t}{\sqrt{2}g\omega_0} < 1$. For our manganite heterostructure, lattice constant $a = 4$ Å, dielectric constant $\epsilon = 20$, magnetic couplings $J_z = 1.00$ meV and $J_{xy}/J_z = 1.39$; we take the pre-factors [in Eq. (2.15)] $\gamma_{ep}^1 = 0.3$ and $\gamma_{ep}^2 = 0.25$. The coefficient in Eq. (2.18) is taken to be $V_s = -3\alpha$ for $\epsilon = 20$; hence the confining

radius for the e_g electron is 1.33 \AA which is less than half the lattice constant.^{1 2} It is important to point out that, since the work function (WF) of CaMnO_3 is larger than the WF of LaMnO_3 (by about 1 eV as given in Table IV of Ref. [149]), we get electrons flowing from LaMnO_3 to CaMnO_3 .³ We approximate $\text{WF}_{\text{CMO}} - \text{WF}_{\text{LMO}}$ to be given by the sum of the nearest-neighbor repulsions due to electron-phonon coupling [which is order of polaron-energy \times coordination-number] and the on-site Coulomb energy V_s . External potential differences V_{ext} , corresponding to external electric fields $E_{\text{ext}} = 300 \text{ kV/cm}$ and $E_{\text{ext}} = 400 \text{ kV/cm}$ (which are less than the breakdown field in LCMO [150]), are applied to study changes in the magnetization profiles.

The simulation (involving the charge and spin degrees of freedom) is carried out using exact diagonalization of the total Hamiltonian in Eq. (2.13). The spins are annealed over 61 values of the dimensionless temperature $[k_B T / (te^{-g^2})]$, in steps of 0.05, starting from 3 and ending at 0.05 with 15000 system sweeps carried out at each temperature. Since hopping energy $te^{-g^2} > J_{xy}$, the inclusion of the spin degrees of freedom certainly commences at temperatures $k_B T > J_{xy}$. Furthermore, the endpoint $k_B T = 0.05te^{-g^2}$ is sufficiently small to correspond to the ground state of the system. Each sweep requires visiting all the lattice sites sequentially and updating the spin configuration at each lattice site by the

¹The on-site Coulomb energy, due to the interaction between an electron on Mn and the positive charge on La, does involve some screening effects due to the oxygen ions surrounding Mn in the perovskite LaMnO_3 ; in fact, the normal modes such as the Jahn-Teller distortions produce screening. Consequently, $V_s \propto -\alpha$ where $V_s/(-\alpha)$ depends on the effective confining radius and the effective dielectric constant. $V_s/(-\alpha)$ could vary between 3 (for $\epsilon = 20$) and 12 (for $\epsilon = 5$ producing weak screening) when confining radius is $a/3$.

²As regards the effective value of the Hubbard U , we know that the occupancy in the d-bands is very largely screened locally either by the change of occupancy in the s-bands (in a metal), or by the oxygen ligands [147]. So while the d-occupancy can change substantially, the actual charge on the positive ion does not. This is what allows the low energies of polaron physics to be relevant in manganites. In an effective one or two band model, all of this screening is subsumed into the interactions [148].

³For electrons to flow from LaMnO_3 to CaMnO_3 , we only need the work function (WF) of LaMnO_3 to be smaller than the WF of CaMnO_3 , i.e., the actual values of the WFs of LaMnO_3 and CaMnO_3 are not relevant for charge transfer.

standard Metropolis Monte Carlo algorithm. We are also allowing the charge degrees of freedom to relax by treating the problem self-consistently. So, at the beginning of each sweep, the Poisson equation is solved additionally to make sure that the number densities have converged and this is achieved with an accuracy of 0.001. Finally, averages of the various measurables in the system are taken over the last 5000 sweeps in the system.

2.4.3 Results and discussion

For numerical simulation, we consider two lattice sizes, namely, 12×6 and 12×8 with number of rows $l_1 = 12$ and number of layers (columns) $l_2 = 6$ or 8 . Here, all the Mn sites in each layer belong solely to either LMO or CMO. This is in contrast to the continuum approximation employed in Sec. 2.3.2 to obtain the charge profile analytically. In Sec. 2.3.2, by exploiting the symmetry of the interactions of the minority carriers on both sides of the LMO-CMO interface, we derived the charge profile with charge density always $\langle n \rangle = 0.5$ at the interface; this corresponds to a system comprising of odd number of MnO_2 layers with the interface MnO_2 layer being shared equally by the LMO and CMO sides.

We consider various situations in our lattices. First, we analyze the case of excluding electron-phonon interaction; consequently, the Hamiltonian of interest is that given by Eq. (2.13), but without the $H_{\text{pol}}^{\text{mf}}$ term. Next, we study the charge and magnetic profiles predicted by the total Hamiltonian of Eq. (2.13) for the symmetric situation (of equal number of LMO and CMO layers) and for different sizeable values of the electron-phonon coupling, i.e., for $g = 2$ & 2.2 . Lastly, we examine the impact on the magnetoelectric effect due to the asymmetry in number of LMO and CMO layers.

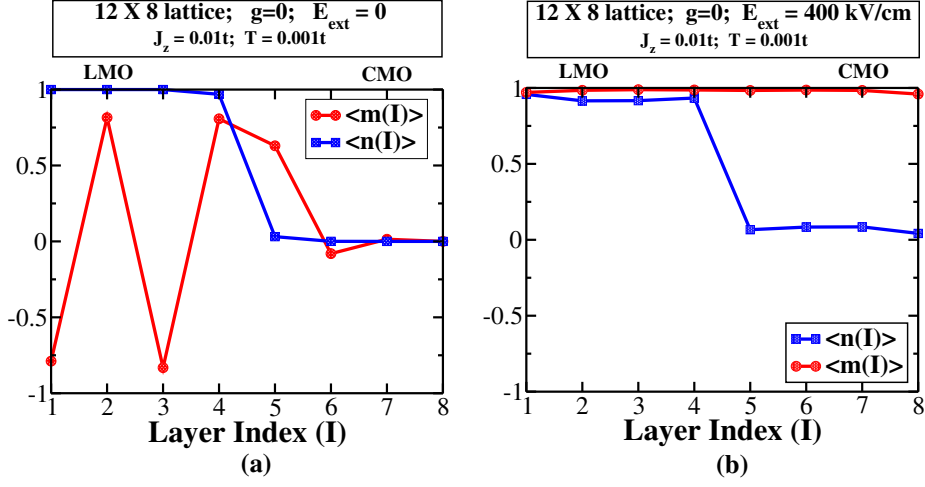


Figure 2.5: Layer-averaged charge density $\langle n(I) \rangle$ and layer-averaged per-site magnetization $\langle m(I) \rangle$ (of t_{2g} spins normalized to unity) for a symmetric 12×8 LMO-CMO lattice when electron-phonon interaction is zero; $J_z = 0.01t$ and $J_{xy}/J_z = 1.39$; $T = 0.001t$; and when (a) external electric field $E_{\text{ext}} = 0$ and (b) $E_{\text{ext}} = 400$ kV/cm.

2.4.3.1 No electron-phonon interaction and $E_{\text{ext}} = 400$ kV/cm

Here, without the electron-phonon interaction, the hopping amplitude t is not attenuated by the factor e^{-g^2} and the ground state is a superposition of various states in the occupation number representation. The electrons are not localized and we do not need to employ simulated annealing; the calculations were performed at a single temperature $k_B T = 0.001t$ on a symmetric heterostructure defined on a lattice with equal number of layers on the LMO side and the CMO side. Furthermore, the charge density profile is essentially dictated by the Coulombic term in Eq. (2.13); the kinetic term and the superexchange term have a negligible effect. Thus, we have density close to 1 on the LMO side and an almost zero density on the CMO side. Now, when a large electric field (400 kV/cm) is applied, a small amount of charge gets pushed across the interface. Then, since the kinetic term is much larger than the superexchange term, double exchange tries to ferromagnetically align the

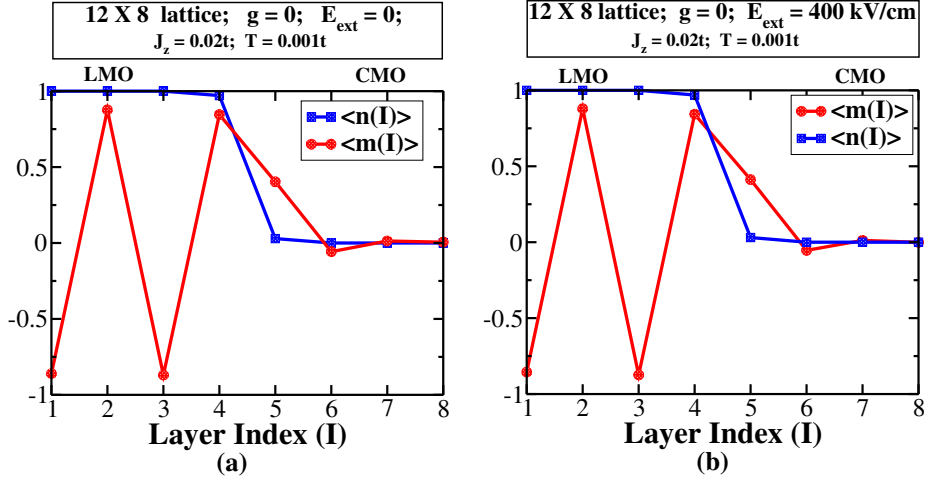


Figure 2.6: Layer-averaged charge density $\langle n(I) \rangle$ and layer-averaged per-site magnetization $\langle m(I) \rangle$ (of t_{2g} spins normalized to unity) for a symmetric 12×8 LMO-CMO lattice when electron-phonon interaction $g = 0$; superexchange $J_z = 0.02t$ and coupling ratio $J_{xy}/J_z = 1.39$; $T = 0.001t$; and when (a) $E_{\text{ext}} = 0$ and (b) $E_{\text{ext}} = 400$ kV/cm.

spins and, as shown in Fig. 2.5, we get a large change in the total magnetization of t_{2g} spins of the system, i.e., 0.91/site for the 12×8 lattice when t_{2g} spins are normalized to unity.

Keeping the temperature fixed at $0.001t$, if we now double the value of J_z to $0.02t$ while retaining the magnetic-coupling ratio $J_{xy}/J_z = 1.39$, it is found that the magnetoelectric effect disappears completely. Owing to the larger superexchange interaction, there is only a small change in the density on the LMO and CMO sides. Consequently, superexchange dominates over double exchange, thereby making the system totally antiferromagnetic (i.e., similar to the bulk, the LMO side is A-AFM and the CMO side is G-AFM). Furthermore, even after the application of a large external electric field (i.e., $E_{\text{ext}} = 400$ kV/cm), there is practically no change in the magnetization as demonstrated in Fig. 2.6.

Next, on retaining the superexchange interaction values of $J_z = 0.01t$ and $J_{xy}/J_z = 1.39$, when the temperature is increased from $0.001t$ to $0.01t$, the disordering effect of the temperature dominates over superexchange making the magnetic profile lose its oscillatory

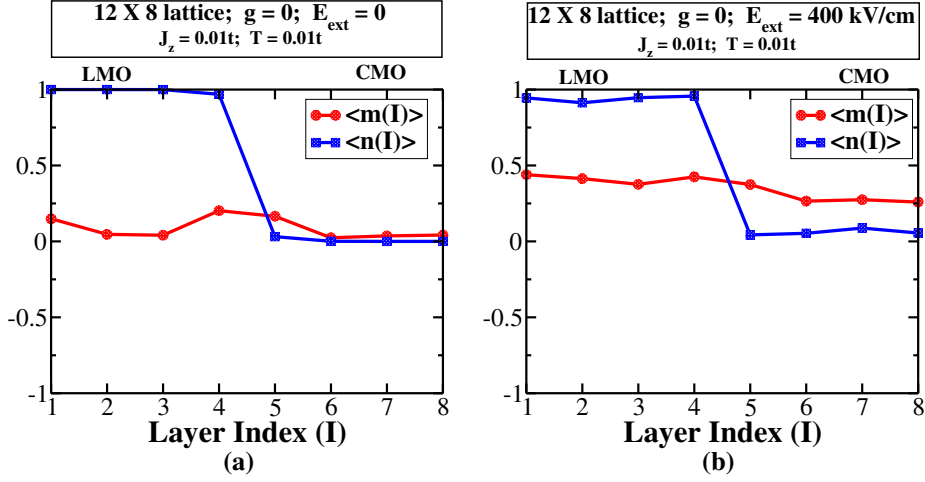


Figure 2.7: Layer-averaged charge density $\langle n(I) \rangle$ and layer-averaged per-site magnetization $\langle m(I) \rangle$ (of normalized-to-unity t_{2g} spins) for a symmetric 12×8 LMO-CMO lattice when $g = 0$; $J_z = 0.01t$ and $J_{xy}/J_z = 1.39$; enhanced temperature $T = 0.01t$; and when (a) $E_{\text{ext}} = 0$ and (b) $E_{\text{ext}} = 400 \text{ kV/cm}$.

nature on the LMO side [as can be seen by comparing Fig. 2.7(a) with Fig. 2.5(a)]. On the application of a sizeable external electric field (i.e., $E_{\text{ext}} = 400 \text{ kV/cm}$), minority carrier density increases on both LMO and CMO sides. However, the disordering effect of the enhanced temperature diminishes the double exchange effect, thereby producing only a modest increase in the magnetization on both the LMO and CMO sides [see Fig. 2.7(b) and Fig. 2.5(b)].

In manganites the electron-phonon interaction is quite strong and leads to sizeable cooperative oxygen octahedra distortions. Hence, to get a more realistic picture, we switch on this interaction and study its effect on the system. Then, the hopping amplitude t is attenuated by the factor e^{-g^2} and the electrons are essentially localized. Consequently, the states are more or less classical in nature with number density at each site close to 1 (i.e., > 0.99 from our calculations) or close to 0 (i.e., < 0.01 from our numerics); the state of the system can be represented by a single state in the occupation number representation. As discussed

in Sec. 3.3, we employ simulated annealing; we arrive at the charge and magnetic profiles reported in the subsequent Secs. 2.4.3.2–2.4.3.6.

2.4.3.2 Symmetric 12×8 lattice with $g = 2.0$ and $E_{\text{ext}} = 300 \text{ kV/cm}$

We now consider a symmetric 12×8 lattice with 4 layers of LMO and another 4 layers of CMO as shown in Fig. 2.8. We find charge modulation in the z -direction on both the sides, with neutral layers (free of minority carriers) sandwiched between charged layers (with minority carriers). The layers at the interface have the largest number of minority carriers with electrons and holes on alternate sites since contributions from both H_{pol} and H_{coul} [given by Eqs. (2.1) and (2.18)] are minimized for this arrangement. Layers 1 and 8, being the farthest from the LMO-CMO interface, are devoid of any minority carriers and retain the expected bulk charge distribution of LMO and CMO.

We will now explain the charge modulation as follows. We compute the energy E_{coul} electrostatically for the one-dimensional chain in Fig. 2.9 using H_{coul} in Eq.(2.18), with lattice constant taken as unity and the number of the neutral layers/sites as x . Then

$$\begin{aligned} E_{\text{coul}} &= \frac{1}{x+1} - \frac{1}{x+2} - \frac{1}{2x+3} - 1 - \frac{1}{x+2} + \frac{1}{x+1} \\ &= \frac{2}{x+1} - \frac{2}{x+2} - \frac{1}{2x+3} - 1. \end{aligned} \quad (2.20)$$

If we plot E_{coul} as a function of x , we find that it drops rapidly till $x = 1$ and attains its minimum value gradually somewhere between $x = 6$ and $x = 7$. Similarly, we expect neutral layers to be present in 2D also and conclude that the charge ordering sets in due to electrostatic Coulomb energy minimization.

In Fig. 2.8, the interface is fairly polarized since the arrangement of electrons and holes on alternate sites produces a strong ferromagnetic coupling between the spins on these

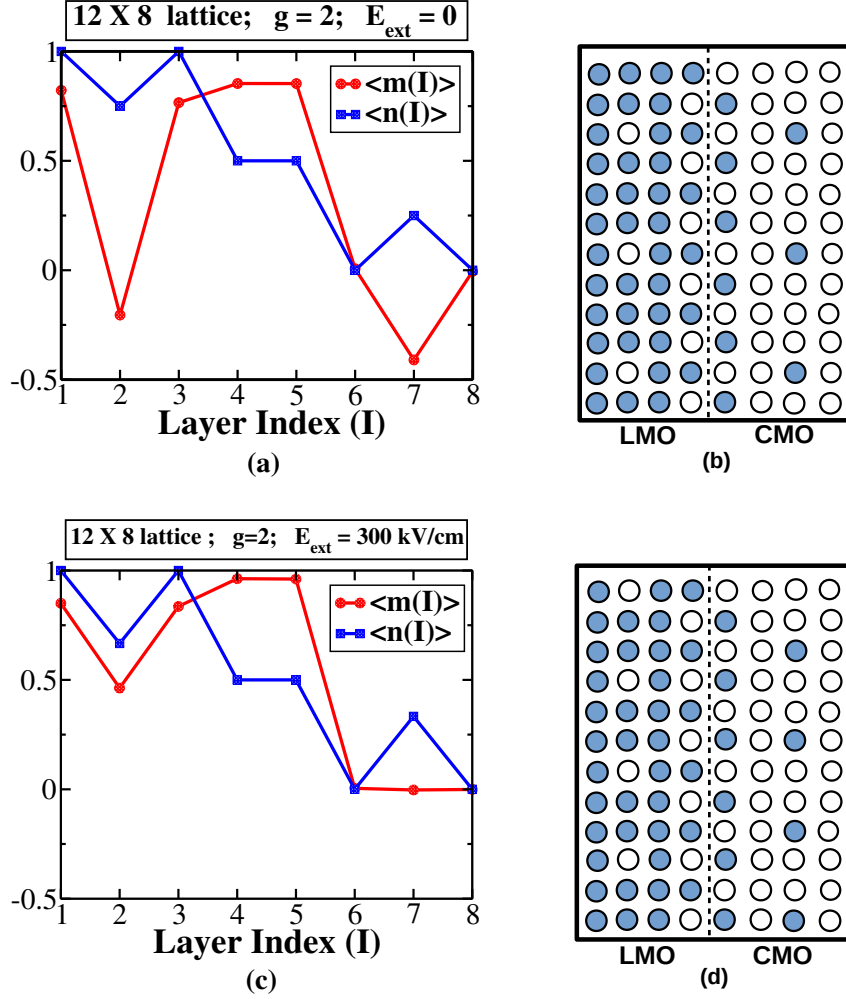


Figure 2.8: In a 12×8 symmetric lattice, when electron-phonon interaction strength $g = 2.0$, (a) when external electric field $E_{\text{ext}} = 0$, layer-averaged profiles of charge density $\langle n(I) \rangle$ and magnetization $\langle m(I) \rangle$ (of the t_{2g} spins normalized to unity); (b) when external electric field $E_{\text{ext}} = 0$, schematic occupation-number representation of ground state charge configuration in the lattice; (c) when a large external electric field $E_{\text{ext}} = 300 \text{ kV/cm}$ is applied, modified layer-averaged charge density $\langle n(I) \rangle$ and layer-averaged magnetization $\langle m(I) \rangle$ (of the t_{2g} spins normalized to unity) for various layers in the lattice; and (d) when $E_{\text{ext}} = 300 \text{ kV/cm}$, reorganized ground state charge configuration.

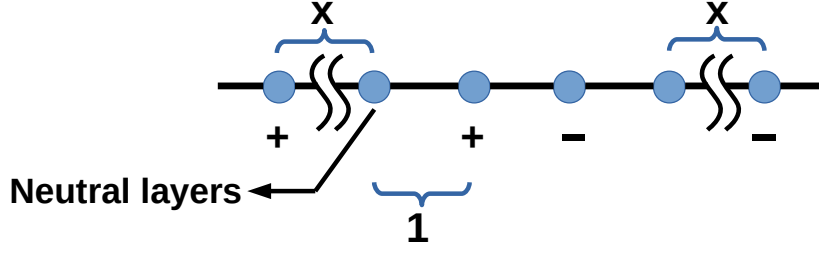


Figure 2.9: Charge modulation due to Coulomb interaction H_{coul} in a one-dimensional symmetric LMO-CMO lattice. The number of neutral layers/sites is x .

sites as $J_{\text{eh}} \gg J_{\text{xy}} > J_z$. Furthermore, again due to ferromagnetic couplings J_{eh} and J_{xy} on the LMO side, the interfacial MnO_2 layer polarizes the neutral layer 3 adjacent to it. Layer 1 is polarized in the direction of layer 3 due to antiferromagnetic coupling J_z . On the CMO side, layer 6 is antiferromagnetic based on the charge configuration; layer 8, as expected, is also fully antiferromagnetic. As regards the case of zero electric field shown in Figs. 2.8(a) and 2.8(b), since layer 3 is antiferromagnetically connected to layer 2, layer 2 shows a small negative magnetization with the magnitude diminished due to the presence of a few (i.e., 3) holes in this layer. On the application of a large electric field $E_{\text{ext}} = 300 \text{ kV/cm}$, as displayed in Figs. 2.8(c) and 2.8(d), number of minority carriers increases in both layer 2 and layer 7. Consequently, the magnetization increases in these layers. On the application of the external electric field, there is an overall increase in the magnetization (of normalized-to-unity t_{2g} spins) by 0.17/site leading to a giant magnetoelectric effect (as can be seen in Fig. 2.10)

A study of the total magnetization with temperature for various external electric fields (i.e., E_{ext} increased in steps of 100 kV/cm from 0), as depicted in Fig. 2.10, reveals that we need a threshold field $\simeq 300 \text{ kV/cm}$ to get a fairly large increase in the total magnetization. Only above the threshold value, the density of minority charges increases and the resulting

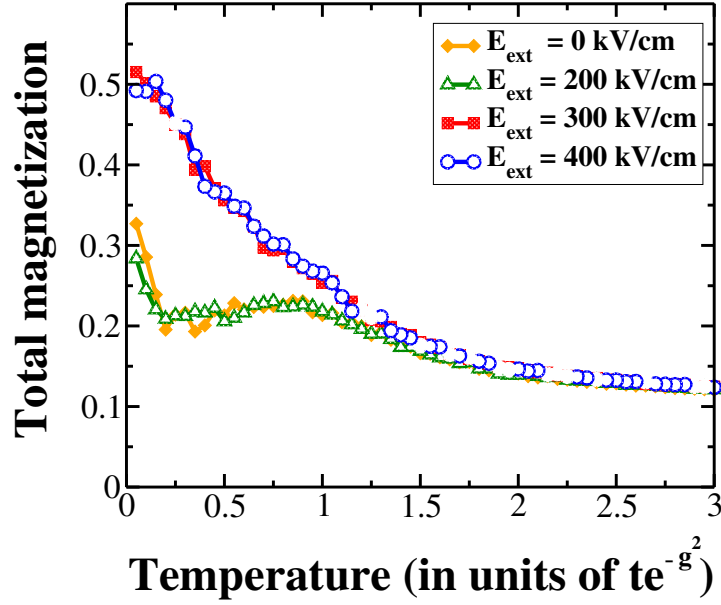


Figure 2.10: Total magnetization as a function of temperature for various E_{ext} in a 12×8 lattice when electron-phonon coupling $g = 2.0$. Figure shows that an enhancement in magnetization occurs for electric fields $E_{\text{ext}} \gtrsim 300$ kV/cm; whereas below this threshold value, total magnetization does not change from its value at $E_{\text{ext}} = 0$ kV/cm. The magnetoelectric effect is reasonably large at temperatures below $0.5te^{-g^2}$ (~ 10 K).

charge configuration is modified; correspondingly, the spin configuration gets altered too. Above 300 kV/cm, the charge configuration gets frozen for consecutive higher electric fields up to 600 kV/cm and no change in the magnetic profile can be expected. Although it may seem that much higher electric fields will further change the magnetization, they will actually produce a breakdown.

2.4.3.3 Symmetric 12×8 lattice with $g = 2.2$ and $E_{\text{ext}} = 0$

Here we would like to point out that charge and magnetic profiles, when electron-phonon coupling g is strong and external electric field is zero, are similar to the profiles when coupling g is weak and external electric field is strong. In fact, as can be seen from Fig. 2.11 and Figs. 2.8(c) and 2.8(d), for $g = 2.2$ and $E_{\text{ext}} = 0$ we get the same charge profile

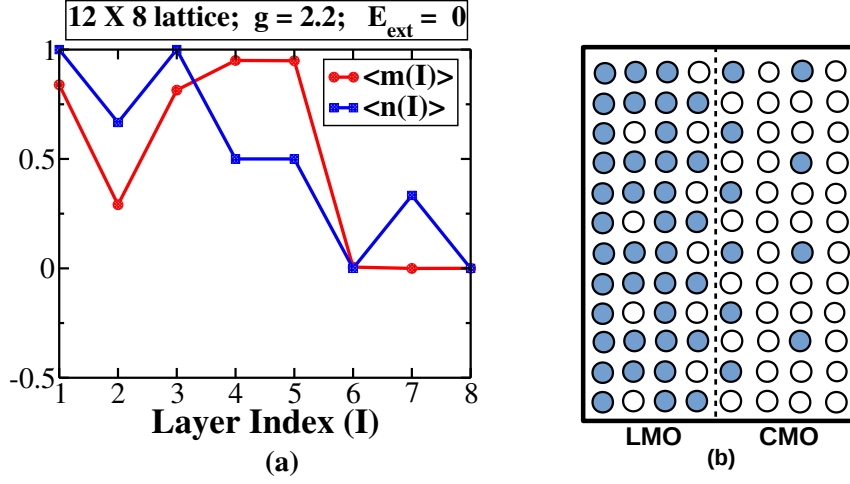


Figure 2.11: Result of enhanced electron-phonon coupling $g = 2.2$ and zero electric field, in a symmetric 12×8 lattice, on (a) layer-averaged charge density $\langle n(I) \rangle$ and layer-averaged magnetization $\langle m(I) \rangle$ (of the t_{2g} spins normalized to unity); and (b) ground state charge configuration.

as when $g = 2.0$ and $E_{\text{ext}} = 300$ kV/cm; the corresponding magnetic profiles in the two cases differ slightly because the ferromagnetic coupling values $J_{\text{eh}} = \gamma_{\text{ep}}^2 t^2 / (g^2 \omega_0)$ are slightly different.

2.4.3.4 Symmetric 12×6 lattice with $g = 2.2$ and $E_{\text{ext}} = 400$ kV/cm

Since the electron-phonon interaction is stronger here (i.e., $g = 2.2$) compared to the situation in Sec. 2.4.3.2, even without the application of an external electric field, the concentration of minority carriers is higher (on both LMO side and CMO side) as can be seen from Figs. 2.12 and 2.8. Again, as depicted in Figs. 2.12(a) and 2.12(b), the interfacial MnO₂ layers (i.e., layers 3 and 4) have electrons and holes on alternate sites resulting in full ferromagnetism. Here, we have fewer layers compared to the case in Sec. 2.4.3.2; there is no charge modulation in the z -direction because shifting the holes from layer 2 to layer 1 increases the number of nearest-neighbor repulsions due to electron-phonon interactions. Layers 2 and 5 also have a sizeable density of minority carriers (i.e., $1/3$). Consequently,

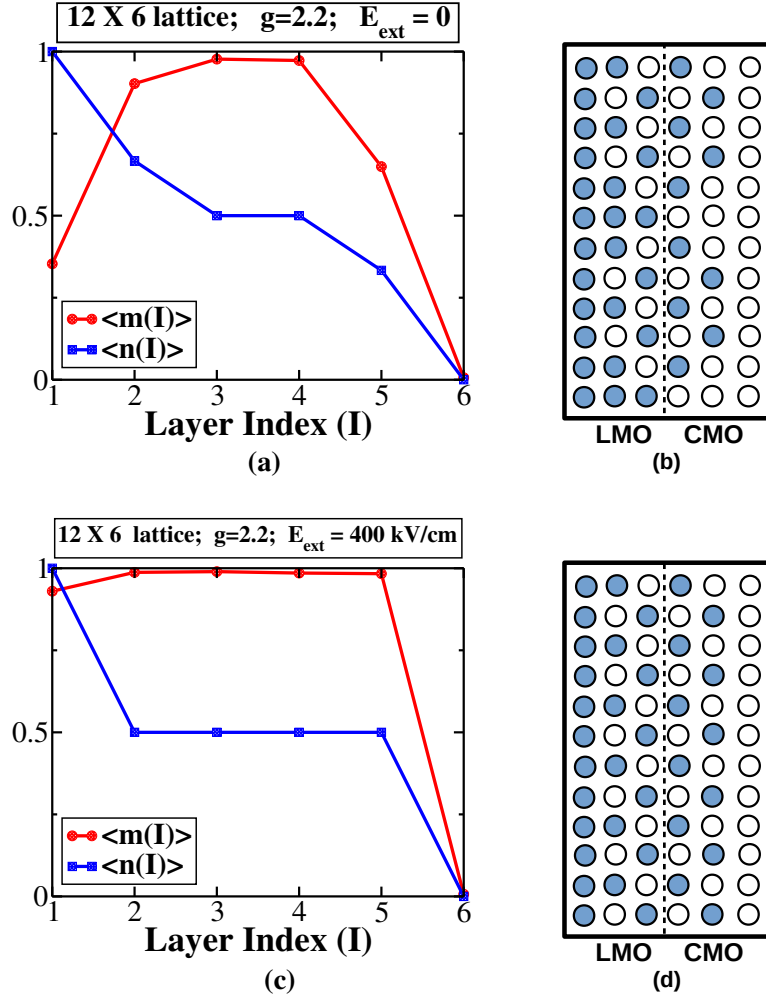


Figure 2.12: In a symmetric 12×6 lattice, for enhanced coupling $g = 2.2$, (a) at zero electric field, layer-averaged charge density $\langle n(I) \rangle$ and layer-averaged magnetization $\langle m(I) \rangle$ of t_{2g} spins normalized to unity; (b) at $E_{\text{ext}} = 0$, ground state configuration; (c) at strong external electric field $E_{\text{ext}} = 400 \text{ kV/cm}$, layer-averaged charge density $\langle n(I) \rangle$ and layer-averaged magnetization $\langle m(I) \rangle$ of t_{2g} spins normalized to unity; and (d) at $E_{\text{ext}} = 400 \text{ kV/cm}$, charge configuration in the ground state.

layer 2 is polarized due to its proximity to layer 3 and the ferromagnetic couplings J_{eh} and J_{xy} ; contrastingly, the combination of J_{eh} and the antiferromagnetic coupling J_z lead to a smaller polarization in layer 5. Layer 1, due to its proximity to layer 2 (with sizeable concentration of holes) is also partially polarized. On the application of a large electric field

($E_{\text{ext}} = 400 \text{ kV/cm}$), as portrayed in Figs. 2.12(c) and 2.12(d), the concentration of holes further increases in layers 2 and 5 leading to fully ferromagnetically aligning these layers with layers 3 and 4. Furthermore, layer 1 also gets more polarized. On the whole, total magnetization (of normalized-to-unity t_{2g} spins) increases by $\sim 0.17/\text{site}$ thus producing a giant magnetoelectric effect.

We will now make an important observation pertaining to the positive charge (Z_j) configuration near the interface. As mentioned before for the heterostructure, we considered the following arrangement with an even number of MnO_2 planes:

$$\text{Ins.}/(\text{LaO-MnO}_2)_n/(\text{La}_{1/2}\text{Ca}_{1/2}\text{O})/(\text{MnO}_2\text{-CaO})_n/\text{Ins.}$$

Here, the Interface is composed of $\text{La}_{1/2}\text{Ca}_{1/2}\text{O}$ and has 0.5 +ve charge per unit $\text{La}_{1/2}\text{Ca}_{1/2}\text{O}$.

In all our calculations we have used $Z_j = 1$ on the LMO side and $Z_j = 0$ on the CMO side. Now, the values of Z_j used are exact for unit cells that are not adjacent to the interface. However, for the unit cell adjacent to the interface on the LMO (CMO) side $Z_j = 1$ ($Z_j = 0$) is an approximation and strictly speaking it should be $Z_j = 0.75$ ($Z_j = 0.25$) as will be explained below. Each unit cell on the LMO side, excluding the unit cell at the interface, comprises of $[(\text{LaO})_{1/2}\text{MnO}_2(\text{LaO})_{1/2}]$ and has 1 +ve charge, i.e., $Z_j = 1$; on the other hand, $[(\text{LaO})_{1/2}\text{MnO}_2(\text{La}_{1/2}\text{Ca}_{1/2}\text{O})_{1/2}]$ is the unit cell at the interface on the LMO side and has 0.75 +ve charge, i.e., $Z_j = 0.75$. Next, on the CMO side, excluding the unit cell at the interface, each unit cell comprises of $[(\text{CaO})_{1/2}\text{MnO}_2(\text{CaO})_{1/2}]$ and has 0 +ve charge, i.e., $Z_j = 0$; contrastingly, $[(\text{La}_{1/2}\text{Ca}_{1/2}\text{O})_{1/2}\text{MnO}_2(\text{CaO})_{1/2}]$ is the unit cell at the interface on the CMO side and has 0.25 +ve charge, i.e., $Z_j = 0.25$. Thus, at the interface we have the situation $Z_j = 0.75|Z_j = 0.25$ instead of $Z_j = 1|Z_j = 0$ as previously assumed.⁴

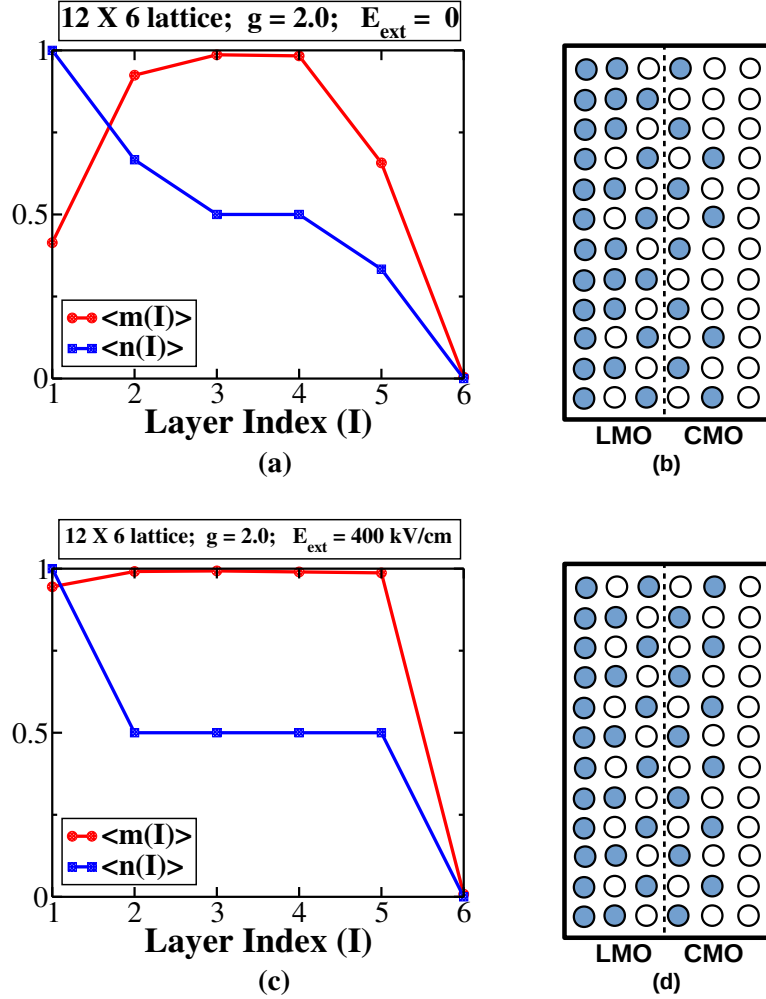


Figure 2.13: In a symmetric 12×6 lattice, for reduced coupling $g = 2.0$ and for the heterostructure $\text{Ins.}/(\text{LaO-MnO}_2)_n/(\text{La}_{1/2}\text{Ca}_{1/2}\text{O})/(\text{MnO}_2\text{-CaO})_n/\text{Ins.}$ with $Z_j = 0.75$ ($Z_j = 0.25$) for the layer adjacent to interface on the LMO (CMO) side, (a) at zero electric field, layer-averaged charge density $\langle n(I) \rangle$ and layer-averaged magnetization $\langle m(I) \rangle$ of t_{2g} spins normalized to unity; (b) at $E_{\text{ext}} = 0$, ground state configuration; (c) at strong external electric field $E_{\text{ext}} = 400$ kV/cm, layer-averaged charge density $\langle n(I) \rangle$ and layer-averaged magnetization $\langle m(I) \rangle$ of t_{2g} spins normalized to unity; and (d) at $E_{\text{ext}} = 400$ kV/cm, charge configuration in the ground state.

We will now demonstrate that, even if intermixing of La and Ca ions is allowed to obtain $Z_j = 0.75|Z_j = 0.25$ at the interface, ground state charge configuration identical to that of the $Z_j = 1|Z_j = 0$ case can be obtained for a slightly lower strength of electron-phonon interaction (i.e., lower nearest-neighbor repulsion) when the same external electric field is employed; this is because the electrons are less confined to the LMO side in the $Z_j = 0.75|Z_j = 0.25$ case. Consequently, as shown in Fig. 2.13, a slightly smaller magnetoelectric effect is observed. We note that V_s is scaled proportional to the values of Z_j in the two lattice layers at the interface. For the $Z_j = 0.75|Z_j = 0.25$ case, we find that there is an overall increase in the magnetization (of normalized-to-unity t_{2g} spins) by 0.16/site (implying a giant magnetoelectric effect) which is only slightly smaller than the previous result of 0.17/site for the $Z_j = 1|Z_j = 0$ case. To get the same ground state charge configuration obtained when $g = 2.2$ for the $Z_j = 1|Z_j = 0$ case, a lower electron-phonon strength of $g = 2$ suffices for the $Z_j = 0.75|Z_j = 0.25$ case.

From the magnetization profile in Fig. 2.13, for the situations when an external electric field is not applied as well as when it is applied, one can clearly see that there is in general a slight increase in the magnetization for all the layers in the $Z_j = 0.75|Z_j = 0.25$ case as compared to the $Z_j = 1|Z_j = 0$ case (see Fig. 2.12). This is because with the lowering of the coupling g for the $Z_j = 0.75|Z_j = 0.25$ case, the strength of the polarizing part of $H_{\text{pol}}^{\text{mf}} \left(\text{i.e., } \frac{\gamma_{\text{ep}}^2 t^2 \cos^2(\frac{\theta_{ij}}{2})}{g^2 \omega_0} \right)$ increases; hence, the magnetizing effect of the electron-phonon interaction also gets enhanced.

⁴Regarding the charge discontinuities at an interface, the polarization (\vec{P}) discontinuity between the LMO side and the CMO side is fixed topologically. Overall difference across the interface does not depend on diffusion of cations near the interface provided the length of diffusion is much smaller than the thickness of the heterostructure and as long as total atoms are conserved. This charge discontinuity is unscreenable in total; the discontinuity produces electric fields (since $\nabla \cdot \vec{P} \neq 0$), though whether or not it is best modeled by a sudden drop from 1 to 0 or an intermediate roll-off (via fractional charges) is a matter of getting detailed atomic relaxations right. The most important point is not the detailed arrangement of charge at the interface, but the total effective charge across the interface (producing polarization discontinuity), which as said above, is topological (see Ref. [151] for details); for our situation the polarization discontinuity is small.

Lastly, it should be noted that (as expected) the magnetic profiles obtained here in Fig. 2.12 are quite similar to those in Figs. 2.3 and 2.4; on the other hand, the agreement between the charge profiles is not as good. On comparing the analytic treatment with the numerical approach, we note that the former makes a continuum approximation to obtain the charge profile. If the number of layers is large compared to the lattice constant, the continuum approximation is valid and the prediction of the analytic approach will agree with the more accurate numerical one. On the other hand, for a small system such as a 12×8 system, charge modulation is generated in the numerical approach unlike the analytic case.

2.4.3.5 Asymmetric 12×8 system of 2 LMO layers and 6 CMO layers with $g = 2.0$ and $E_{\text{ext}} = 300 \text{ kV/cm}$

We have an asymmetry here regarding the number of layers; the LMO side has two layers whereas the CMO side has six layers. For zero external electric field, as shown in Figs. 2.14(a) and 2.14(b), the two interfacial MnO_2 layers 2 and 3 contain perfectly alternate arrangement of electrons and holes; hence, the layers are fully polarized. Layer 1 is also ferromagnetically aligned with layer 2 because of their proximity. Beyond layer 3, similar to the G-AFM order in bulk CMO, the CMO side is antiferromagnetic, resulting in zero magnetization. Turning on the sizeable electric field $E_{\text{ext}} = 300 \text{ kV/cm}$, as depicted in Figs. 2.14(c) and 2.14(d), leads to a few electrons from layer 1 ending up in a farther layer 7; resultantly, the magnetic polarons in layer 7 partially polarize it. It is interesting to note that, here too charge modulation occurs due to the Coulomb term H_{coul} as demonstrated through Eq. (2.20). There is an overall increase in the magnetization (of normalized-to-unity t_{2g} spins) by 0.04/site; thus, the magnetoelectric effect is not huge.

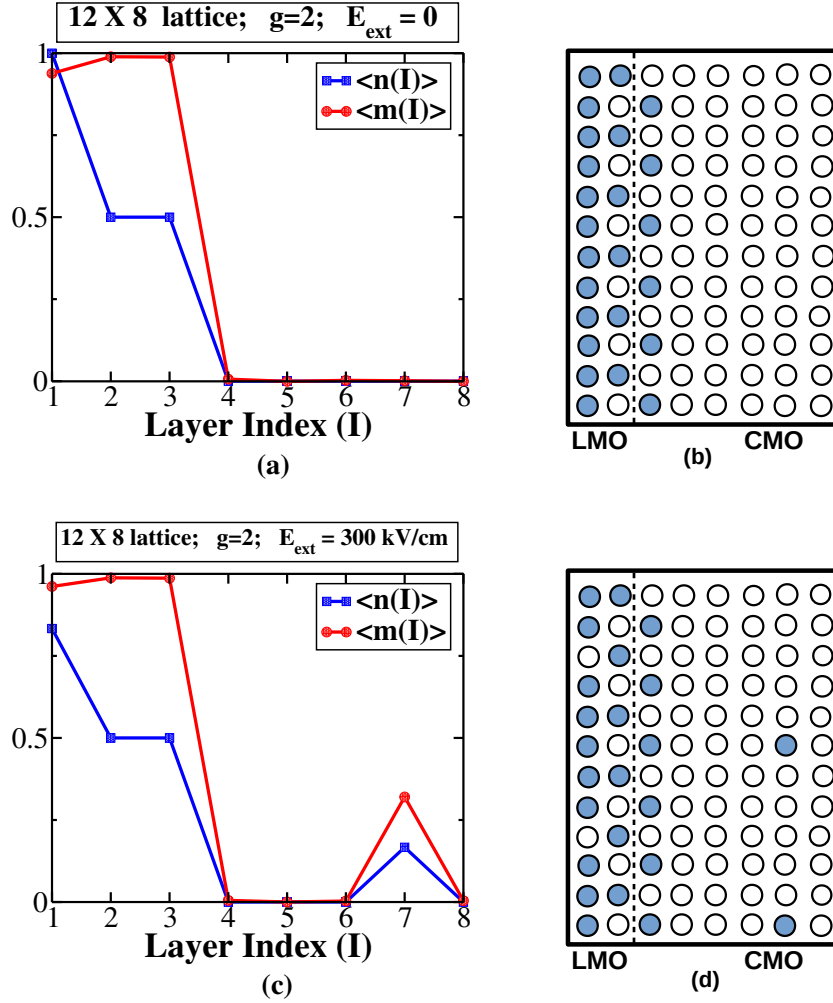


Figure 2.14: In asymmetric heterostructure defined on a 12×8 lattice with 2 layers of LMO and 6 layers of CMO, when coupling $g = 2.0$, (a) at $E_{\text{ext}} = 0$, layer-averaged charge density $\langle n(I) \rangle$ and layer-averaged magnetization $\langle m(I) \rangle$ of normalized-to-unity t_{2g} spins; (b) at $E_{\text{ext}} = 0$, ground state configuration; (c) at $E_{\text{ext}} = 300$ kV/cm, layer-averaged charge profile $\langle n(I) \rangle$ and layer-averaged magnetization profile $\langle m(I) \rangle$ of normalized-to-unity t_{2g} spins; and (d) at $E_{\text{ext}} = 300$ kV/cm, ground state configuration.

2.4.3.6 Asymmetric 12×8 system of 6 LMO layers and 2 CMO layers with $g = 2.0$ and $E_{\text{ext}} = 300$ kV/cm

Here, compared to the previous structure in Fig. 2.14, we have the opposite asymmet-

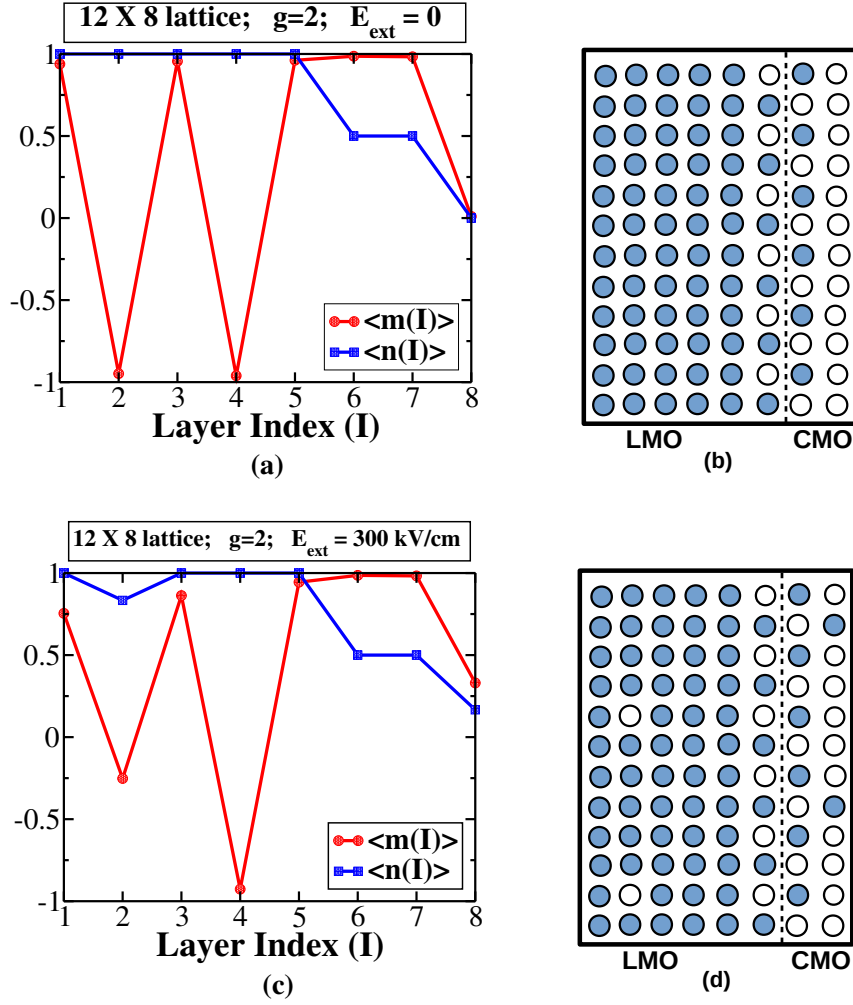


Figure 2.15: In asymmetric 12×8 lattice with 6 layers of LMO and 2 layers of CMO, when electron-phonon interaction $g = 2.0$, (a) at external electric field $E_{\text{ext}} = 0$, layer-averaged electron density $\langle n(I) \rangle$ and layer-averaged magnetization $\langle m(I) \rangle$ of t_{2g} spins normalized to unity; (b) at $E_{\text{ext}} = 0$, ground state electronic configuration; (c) at $E_{\text{ext}} = 300$ kV/cm, layer-averaged electron density $\langle n(I) \rangle$ and layer-averaged magnetization $\langle m(I) \rangle$ of t_{2g} spins normalized to unity; and (d) at $E_{\text{ext}} = 300$ kV/cm, ground state.

ric structure of 6 LMO layers and 2 CMO layers (see Fig. 2.15). Due to the asymmetry connection between these two structures, we obtain a mirror image of the previous charge configuration for both with and without the external electric field. The interfacial MnO_2 layers 6 and 7, as expected, are totally ferromagnetic. Furthermore, layer 5 is also fer-

romagnetically aligned with layers 6 and 7 due to the ferromagnetic couplings J_{eh} and J_{xy} . At zero external field [as shown in Figs. 2.15(a) and 2.15(b)], similar to the bulk situation, we have A-AFM on the LMO side up to layer 5; layer 8, similar to the bulk CMO, is also antiferromagnetic. The minority carriers, generated due to the external electric field $E_{ext} = 300 \text{ kV/cm}$ [as shown in Figs. 2.15(c) and 2.15(d)], produce magnetic polarons which increase the polarization. There is an overall increase in the magnetization (of normalized-to-unity t_{2g} spins) by about 0.1/site implying a large magnetoelectric effect.

From the various symmetric and asymmetric LMO-CMO configurations considered, we conclude that the symmetric arrangement yields the largest magnetoelectric effect.

Lastly, for both symmetric and asymmetric heterostructures, the dominant charge interactions (i.e., Coulombic interaction and CEPI) lead to checkerboard order (i.e., alternating electrons and holes) for the two layers at the interface. At the interface, it is important to note that an electron in one layer is next to a hole in the next layer. This scenario is not true in the bulk $\text{La}_{1/2}\text{Ca}_{1/2}\text{MnO}_3$. In bulk $\text{La}_{1/2}\text{Ca}_{1/2}\text{MnO}_3$, in the z -direction (i.e., direction perpendicular to the planes with zigzag ferromagnetic chains that are coupled antiferromagnetically) an electron in one orbital is above another electron in the same orbital; this can support the experimentally observed CE-AFM ordering. However, for the charge ordering that results at the interface where an electron in one plane is next to a hole in the next plane, CE-type spin order is not possible (because ferromagnetic zigzag chains in one plane cannot lie exactly over ferromagnetic zigzag chains in the next plane). On taking the dominant charge interactions and the dominant magnetic interactions (i.e., electron and hole on adjacent sites being ferromagnetically coupled), we get ferromagnetic layers at the interface.

In Ref. [32], since they ignore CEPI (which produces large nearest-neighbor repulsion), they do not get a charge ordering where an electron in one plane at the interface is next to a

hole in the next plane at the interface. Additionally, it should also be noted that, a hole (in the plane at the interface on the LMO side) prefers to be next to an electron (in the plane at the interface on the CMO side) due to attractive Coulombic interaction.

2.5 Conclusions

We used the heuristic notion that, when the two Mott insulators LMO and CMO are brought together to form a heterostructure, one may realize the entire phase diagram of $\text{La}_{1-x}\text{Ca}_x\text{MnO}_3$ across the heterostructure with the $x = 0$ phase occurring at the LMO surface at one end and evolving to the $x = 0.5$ state at the oxide-oxide interface and finally to the $x = 1$ phase at the other end of CMO. However, owing to the reduced dimensions (namely, quasi two-dimensions), we expect only A-AFM and FMI phases on the LMO side. On enhancing the minority carrier density (on both sides of the interface) by using a sizeable external electric field, we showed that the FMI region can be further expanded at the expense of the A-type AFM region on the LMO side and the G-AFM domain on the CMO side, thereby producing a giant magnetoelectric effect. It is important to note that the system behaves like an anisotropic solid: for a given average density in a layer, the minority charges by and large order periodically and as far apart as possible; the Coulombic interaction and the CEPI dictate how the charge arrangement of one layer adjusts itself with respect to the configuration in another layer. Furthermore, the two layers at the interface are ferromagnetically ordered as they are at half-filling. When electric fields are introduced in the system, the minority charge density away from the interface gets enhanced leading to charge reordering; consequently, the magnetization away from the interface changes layer by layer resulting in an increase in the total ferromagnetic moment. This scenario is key to the understanding of the magnetoelectric effect.

We would like to point out that the model in Sec. 2.4 is not applicable in three dimensions because upper wide band becomes relevant (see Ref. [141, 142]); consequently, states such as the ferromagnetic metal in LCMO cannot be realized using this model. Furthermore, long-range Coulomb interactions are not very important to explain the gross features of the phase diagram in the three-dimensional bulk system.

As a guide to designing magnetoelectric devices, we find that symmetric heterostructures with equal number of LMO and CMO layers yield larger magnetoelectric effect compared to asymmetric heterostructures with unequal number of LMO and CMO layers. It should also be noted that this heterostructure/device can be used near helium liquefaction temperatures; on the other hand, the magnetoelectric function disappears before nitrogen liquefaction temperature is attained.

We also would like to mention that if a superlattice were formed from the heterostructure (Ins.)/(LaMnO₃)_n/Int./(CaMnO₃)_n/(Ins.), then the dipoles from each repeating heterostructure unit will add up to produce a giant electric dipole moment; furthermore, this superlattice will also realize a giant magnetoelectric effect. On the other hand, if the insulator layers were not present, the superlattice formed from the repeating unit (LaMnO₃)_n/(CaMnO₃)_m would not produce a large electric dipole as the charge from LMO can leak to CMO on both sides leading to a small net dipole moment. More importantly, the (LaMnO₃)_n/(CaMnO₃)_m superlattice will also not generate a giant magnetoelectric effect as an applied electric field will not alter much the total amount of charge in LMO or CMO; this is because charge leaked by LMO to CMO on one side is replaced by CMO on the other side.

Based on the above arguments, it should be clear that, compared to experiments involving superlattices where alloy/bulk effect vanishes when the thinner side of the repeating unit has more than two layers, in our heterostructure bulk nature should vanish when the

thinner side has more than 1 layer. Thus, in the superlattice $(\text{LaMnO}_3)_{2n}/(\text{SrMnO}_3)_n$ studied in Ref. [20], the metallic behavior (corresponding to bulk $\text{La}_{0.67}\text{Sr}_{0.33}\text{MnO}_3$) disappears for $n > 2$ and is replaced by insulating behavior; whereas, in the heterostructure $(\text{Ins.})/(\text{LaMnO}_3)_{2n}/\text{Int.}/(\text{SrMnO}_3)_n/(\text{Ins.})$ we expect insulating behavior for $n > 1$. This observation supports our assumption that, in our q2D LMO-CMO heterostructures (corresponding to LCMO that has a narrower band width and a stronger electron-phonon coupling compared to LSMO), only a single narrow-width polaronic band is pertinent. Additionally, interfacial roughness (if considered) will further reduce the band width and suppress metallicity.

Lastly, it should also be pointed out that, in a realistic situation, we have electron-electron repulsion (produced by cooperative electron-phonon interaction) and double-exchange generated ferromagnetic coupling extending to next-nearest-neighbor sites [152] leading to a larger magnetic polaron and thus producing a stronger magnetoelectric effect compared to what our calculations reveal.

STUDY OF THE FERROMAGNETIC-INSULATOR PHASE IN MANGANITES

3.1 Introduction

Perovskite oxides, such as manganites, display a variety of orbital, charge, and spin orders when the parent oxide is doped. While significant progress has been made in characterizing most of the phenomena in bulk doped materials, the understanding pertaining to ferromagnetic insulator is still elusive. The doped alloy $T_{1-x}D_x\text{MnO}_3$ (where T refers to trivalent rare-earth elements such as La, Pr, Nd, etc. and D refers to divalent alkaline elements Sr, Ca, etc.) is an antiferromagnet when $x > 0.5$ with the nature of the antiferromagnet (i.e., A-, C-, CE-, or G-type antiferromagnet) depending on the compound and the dopant value x [15, 153, 154]. Contrastingly, for $x < 0.5$, $T_{1-x}D_x\text{MnO}_3$ is an intriguing ferromagnetic

insulator (FMI) at smaller values of x (i.e., $0.1 \lesssim x \lesssim 0.2$) [9, 10, 18] and is a ferromagnetic metal at higher dopings in the manganite systems $\text{La}_{1-x}\text{Sr}_x\text{MnO}_3$, $\text{La}_{1-x}\text{Ca}_x\text{MnO}_3$, $\text{Pr}_{1-x}\text{Sr}_x\text{MnO}_3$, and $\text{Nd}_{1-x}\text{Sr}_x\text{MnO}_3$.

For modeling the diverse orderings and for exploiting the functionality in these transition-metal oxides, one needs effective Hamiltonians for various types of interactions. Although the importance of strong electron-phonon interaction (EPI) has been pointed much earlier [119] and significant progress has been made some time ago in numerically treating electron-phonon interaction in sizeable systems [155], the treatment of cooperative EPI (involving quantum phonons) was accomplished analytically only more recently in two dimensions (2D) [156]. It has been demonstrated analytically in Ref. [156] that introducing cooperative effects, when EPI is strong, produces nearest-neighbor (NN), next-nearest-neighbor (NNN), and next-to-next-nearest-neighbor (NNNN) interactions. Furthermore, incorporating spin-spin interactions along with cooperative strong EPI is still an unsolved analytic problem.

As regards experiments pertaining to ferromagnetic-insulating regions, while some suggested microscopically homogeneous electronic properties [157–159], others speculate that coexistence of ferromagnetic metallic phases and antiferromagnetic insulating phases leads to an inhomogeneous ferromagnetic insulating state [160, 161].

We will now argue, without considering any specific model, that ferromagnetic insulating phases are possible at low doping in manganites by presenting below general theoretical points based on the essential features of manganites.

1. Kinetic energy (KE) is quite small at low doping because bare hopping is small (caused by lower tolerance factor [123], cation disorder, compatibility of distortions [133]) and the electron-phonon coupling is strong. The electrons are rendered

essentially immobile and site localized due to spatial disorder.

2. Potential energy [from repulsive interactions, due to cooperative EPI, that are intermediate-range, i.e., NN, NNN, NNNN, etc.] is much larger than KE. The ground state is classical and the state of the system can be expressed by a single state in the occupation number basis with number density at each site either 1 or 0.

The fact that electrons are essentially site localized also follows from the treatment in Ref. [45, 46]; then, only a localized polaronic band is relevant and the upper wide band cannot overlap with the lower narrow polaronic band.

Furthermore, a simple type of phase separated state with ferromagnetic droplets (each containing one carrier) in an antiferromagnetic matrix was shown to be possible in Ref. [47]. The mobility of these magnetic polarons is low and they are easily localized by disorder and Coulomb interactions.

Thus the potential energy determines the charge and spin order.

3. Because of cooperative strong EPI, a NN electron-hole pair has a strong ferromagnetic interaction $[t^2 \cos^2(\theta/2)/(2E_{JT})]$ with E_{JT} being the cooperative Jahn-Teller energy, t the hopping term between the NN sites, and θ the angle between the NN core spins]. Hence, a robust ferromagnetic cluster is produced in the vicinity of a hole.
4. Our model for magnetic interaction applies to manganites with low density of localized holes. In regions away from the holes, the cooperative EPI retains essentially the same orbital texture as in the undoped manganite. As a result, in regions without holes, the magnetic interaction is A-AFM just as in the undoped manganite. As regards the regions with holes, since the holes are site localized, the holes only virtually

hop to a NN site and back and thus produce ferromagnetic coupling with NN electrons. This ferromagnetic coupling, between NN electron-hole pair, is much stronger than A-AFM coupling.

5. Presence of site localized holes produces FMI clusters due to formation of magnetic polarons. A hole will polarize NN electrons (and realistically speaking, NNN and NNNN electrons as well) through virtual hopping, thereby producing a magnetic polaron. A collection of interacting magnetic polarons will produce a FMI region. It is interesting to note that FMI regions are present at moderate doping in manganites that are narrow band ($\text{Pr}_{1-x}\text{Ca}_x\text{MnO}_3$), intermediate band ($\text{La}_{1-x}\text{Ca}_x\text{MnO}_3$) and wide band ($\text{La}_{1-x}\text{Sr}_x\text{MnO}_3$).

3.2 Effective Hamiltonian

In this section we focus on the analytical treatment of the effective Hamiltonian which will be used for numerical simulation. We are working with a 2D version of the pervovskite manganite system which has Mn-O-Mn bonds along the x and y directions. We have e_g electrons (or holes) interacting with the oxygen atoms. We have restricted our analysis to a system of fermions interacting with the oxygens in the xy -plane via cooperative breathing mode and with the out-of-plane z -direction oxygens through non-cooperative breathing mode as depicted in Fig. 3.1.

Apart from the itinerant e_g electrons, we also have a t_{2g} localized core-spin background; the large $S = 2$ spin (comprised of contribution from a e_g spin and three t_{2g} spins) at each site is considered classical.

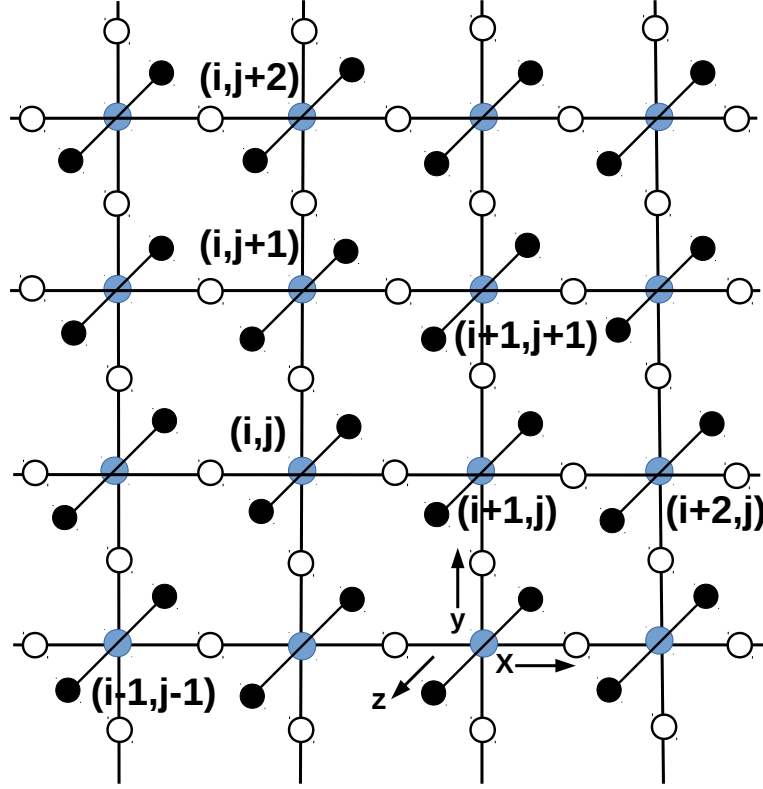


Figure 3.1: Schematic diagram for a 2D cooperative breathing mode (CBM) system. Hopping sites for holes are represented by blue solid circles, in-plane oxygen atoms (participating in the CBM) by black empty circles, and non-cooperative out-of-plane oxygen atoms by solid black circles.

Thus the Hamiltonian of such a system has five interactions: the kinetic energy of the fermions, the fermion-lattice coupling energy, the lattice energy, the spin-spin interaction energy, and the fermion-disorder interaction energy.

$$H = H_{\text{KE}} + H_{\text{int}} + H_{\text{lat}} + H_{\text{SE}} + H_{\text{dis}}. \quad (3.1)$$

Here,

$$H_{\text{KE}} = -t \sum_{i,j} \left[\cos \left(\frac{\theta_{i,j;i+1,j}}{2} \right) d_{i+1,j}^\dagger d_{i,j} + \cos \left(\frac{\theta_{i,j;i,j+1}}{2} \right) d_{i,j+1}^\dagger d_{i,j} + \text{H.C.} \right], \quad (3.2)$$

and $d_{i,j}(d_{i,j}^\dagger)$ represents the annihilation (creation) operator for the fermion at site (i, j) ; t is the hopping amplitude for the fermion; the hopping process is modified by θ , the angle between two spins at NN sites [115, 143]. See Sec. 1.5.1 for a background on Double Exchange process. The second term represents the interaction between the fermions and the quantum phonons in the system and is expressed as [156]

$$H_{\text{int}} = -g\omega_0 \sum_{i,j} \left\{ (a_{x;i,j}^\dagger + a_{x;i,j})(n_{i,j} - n_{i+1,j}) + (b_{y;i,j}^\dagger + b_{y;i,j})(n_{i,j} - n_{i,j+1}) + \gamma(c_{z;i,j}^\dagger + c_{z;i,j})n_{i,j} \right\}, \quad (3.3)$$

where $\gamma = \sqrt{2}$, g is the electron-fermion coupling constant, ω_0 is the optical-phonon frequency, and $n_{i,j} = d_{i,j}^\dagger d_{i,j}$. The displacement of the oxygen atom that is adjacent to the site (i, j) in the positive x [y] direction is given by $\frac{(a_{x;i,j}^\dagger + a_{x;i,j})}{\sqrt{2m\omega_0}} \left[\frac{(b_{y;i,j}^\dagger + b_{y;i,j})}{\sqrt{2m\omega_0}} \right]$. In the z direction, the relative displacement of the two oxygen atoms next to site (i, j) is denoted by $\frac{(c_{z;i,j}^\dagger + c_{z;i,j})}{\sqrt{2m\omega_0/2}}$ with $m/2$ being the reduced mass of the oxygen pair. Next, the lattice energy due to quantum harmonic oscillators is given by

$$H_{\text{lat}} = \sum_{i,j} \left(a_{x;i,j}^\dagger a_{x;i,j} + b_{y;i,j}^\dagger b_{y;i,j} + \eta c_{z;i,j}^\dagger c_{z;i,j} \right), \quad (3.4)$$

with η being set to be 1. The last term represents the interaction with disorder and is

expressed as

$$H_{\text{dis}} = \sum_{i,j} V_{i,j} n_{i,j}, \quad (3.5)$$

where $V_{i,j}$ is the potential due to spatial disorder.

Now, to arrive at an effective Hamiltonian which can be expressed solely in terms of fermionic operators, we take resort to an analytic approach similar to that described in [156]. For large electron-phonon coupling and restricting the system to the non-adiabatic regime, $t/\omega_0 \lesssim 1$, the above Hamiltonian H is subject to a canonical transformation (i.e., modified Lang-Firsov transformation) to produce an unperturbed part H_0 and the perturbation term H_1 . To obtain an effective Hamiltonian, we perform second-order perturbation theory (as in Refs. [137, 156]) and obtain

$$\begin{aligned} H_{\text{eff}} = & -E_p \sum_{i,j} n_{i,j} + 2V_p \sum_{i,j} \left(n_{i,j} n_{i+1,j} + n_{i,j} n_{i,j+1} \right) \\ & + t e^{-(E_p+V_p)/\omega_0} \sum_{i,j} \left[\cos \left(\frac{\theta_{i,j;i+1,j}}{2} \right) d_{i+1,j}^\dagger d_{i,j} \right. \\ & \left. + \cos \left(\frac{\theta_{i,j;i,j+1}}{2} \right) d_{i,j+1}^\dagger d_{i,j} + \text{H.c.} \right] \\ & + H^{(2)} + H_{\text{SE}} + \sum_{i,j} V_{i,j} n_{i,j}, \end{aligned} \quad (3.6)$$

where the polaronic energy $E_p = (4+\gamma^2)g^2\omega_0 = 6g^2\omega_0$ and the nearest-neighbor repulsion energy $V_p = g^2\omega_0$; the second order perturbation theory yields the term $H^{(2)}$. The small parameter of the perturbation theory is $\sim \left[\frac{t^2}{2(E_p+V_p)\omega_0} \right]^{\frac{1}{2}}$ as derived in Ref. [162]. Now, the effective hopping term $t e^{-(E_p+V_p)/\omega_0} \ll \omega_0$ and $V_{i,j} \ll E_p$. For large g , the effective hopping term will be very small compared to the other terms in $H_{\text{eff}} - H_{\text{SE}}$. Hence, we ignore the kinetic energy of the system and treat the system as made up of carriers that

are localized due to weak spatial disorder. Then, we are justified in treating the problem entirely classically with physics being governed by the dominant potential energy terms in the effective Hamiltonian. The second term of H_{eff} can as well be represented in terms of electron-hole attraction instead of fermion-fermion repulsion. In general

$$V_p \sum_{i,j,\delta} n_{i,j} n_{i+\delta,j} = -V_p \sum_{i,j,\delta} n_{i,j} (1 - n_{i+\delta,j}) + V_p \sum_{i,j,\delta} n_{i,j}. \quad (3.7)$$

This formalism adds a constant energy term $V_p \sum_{i,j,\delta} n_{i,j}$ to the Hamiltonian and thus does not change the physics of the problem. Then, using Eq. (3.7) we can rewrite Eq. (3.6) as

$$H_{\text{eff}} = -E_p \sum_{i,j} n_{i,j} - 2V_p \sum_{i,j} \left\{ n_{i,j} (1 - n_{i+1,j}) + n_{i,j} (1 - n_{i,j+1}) \right\} + 4V_p \sum_{i,j} n_{i,j} + H^{(2)} + H_{\text{SE}}. \quad (3.8)$$

The convention we will use throughout the chapter is that $n_{i,j}$ will represent number density of a hole at the lattice site (i, j) of the system. To calculate $H^{(2)}$, we go through an algebra similar to that mentioned in Appendix A of Ref. [156] and arrive at a nearest-neighbor repulsion term corresponding to the process where a particle in 2D virtually hops to its NN and comes back. When a hole at site (i, j) hops to its NN site, such as $(i+1, j)$, and comes back, we need to keep track of the occupancy of the three relevant nearest-neighbor sites of the intermediate site $(i+1, j)$, i.e., the occupancy of the three sites $(i+2, j)$, $(i+1, j+1)$ and $(i+1, j-1)$. Depending on how many of these three sites are filled, the coefficient for the hopping-and-returning process will be modified.

Clearly, there are four such possibilities for the coefficients and they will be considered below.

3.2.1 Three NN sites of the intermediate site are filled by electrons.

In Fig. 3.2, when the intermediate site containing an electron is surrounded by a hole and three electrons, we depict the hole at site (i, j) hopping to its NN site (the intermediate site) and returning back. The intermediate site can be any of the four NNs of the originating site (i, j) . A schematic view of the four possibilities is shown in Fig. 3.2.

When a hole is at (i, j) , its energy is equal to $-E_p$. The oxygen atoms on both the sides of the initial site are attracted by the hole on the initial site and hence are pulled towards the hole. When the hole virtually hops to the intermediate site, its energy is equal to $E_p + 2V_p$ because the oxygen distortions remain unchanged; in the energy of the intermediate state, E_p arises due to the distortion without the hole whereas the extra energy $2V_p$ (equal in magnitude to the NN repulsion energy between two holes) results due to displacing the oxygen atoms towards the initial site and away from the hole. Hence, change in the energy when the hole jumps from the originating site to the intermediate site is equal to $2E_p + 2V_p$. Thus, the coefficient of the second order perturbation term turns out to be $\frac{t^2}{2E_p + 2V_p}$ and the

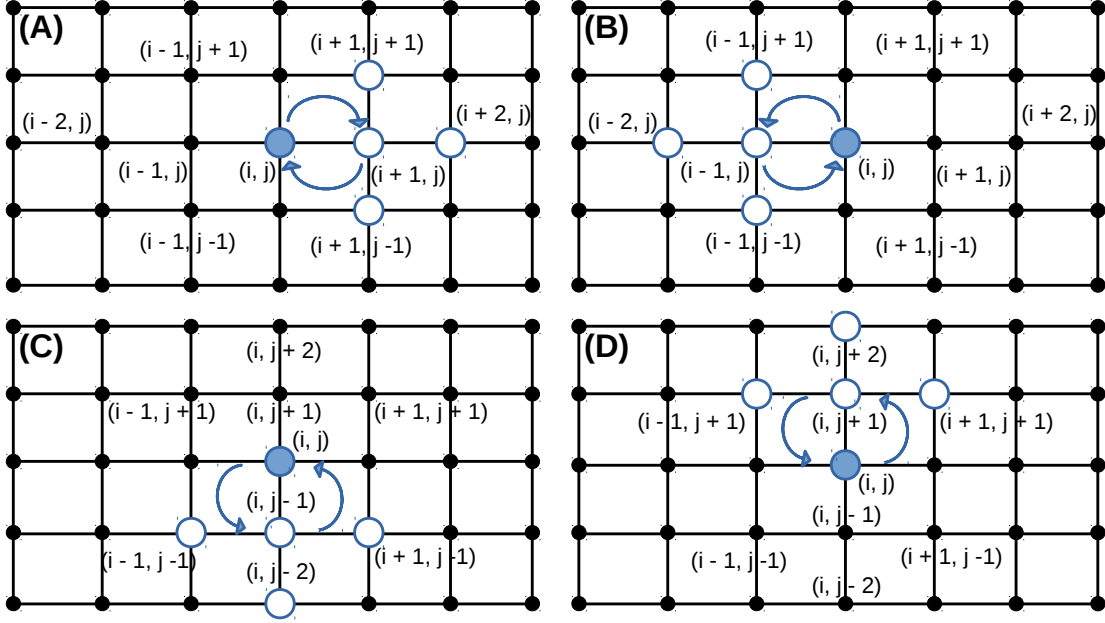


Figure 3.2: Schematic diagram for the four possibilities of a hole, at an originating site (i, j) , hopping to its NN site (the intermediate site) and coming back (when three NN sites of the intermediate site are occupied by electrons): (A) hole at (i, j) hops to its right NN at $(i + 1, j)$ and comes back; (B) hole at (i, j) jumps to its left NN at $(i - 1, j)$ and returns back; (C) hole at (i, j) jumps to its downward NN at $(i, j - 1)$ and comes back; (D) hole at (i, j) hops to its upper NN at $(i, j + 1)$ and returns. A hole is represented by a blue solid circle and a particle (i.e., electron) by a blue empty circle. All lattice sites that are not relevant to the consideration are represented by black solid circles.

contribution to $H^{(2)}$ from all the possibilities corresponding to Fig. 3.2 is given by

$$\begin{aligned}
 H_1^{(2)} = & \frac{-t^2}{(2E_p + 2V_p)} \sum_{i,j} \left[\cos^2 \left(\frac{\theta_{i,j;i+1,j}}{2} \right) \left\{ n_{i,j} (1 - n_{i+1,j}) (1 - n_{i+2,j}) (1 - n_{i+1,j+1}) (1 - n_{i+1,j-1}) \right\} \right. \\
 & + \cos^2 \left(\frac{\theta_{i,j;i-1,j}}{2} \right) \left\{ n_{i,j} (1 - n_{i-1,j}) (1 - n_{i-2,j}) (1 - n_{i-1,j+1}) (1 - n_{i-1,j-1}) \right\} \\
 & + \cos^2 \left(\frac{\theta_{i,j;i,j+1}}{2} \right) \left\{ n_{i,j} (1 - n_{i,j+1}) (1 - n_{i,j+2}) (1 - n_{i-1,j+1}) (1 - n_{i+1,j+1}) \right\} \\
 & \left. + \cos^2 \left(\frac{\theta_{i,j;i,j-1}}{2} \right) \left\{ n_{i,j} (1 - n_{i,j-1}) (1 - n_{i,j-2}) (1 - n_{i-1,j-1}) (1 - n_{i+1,j-1}) \right\} \right]. \quad (3.9)
 \end{aligned}$$

3.2.2 Any two of NN sites of the intermediate site is filled.

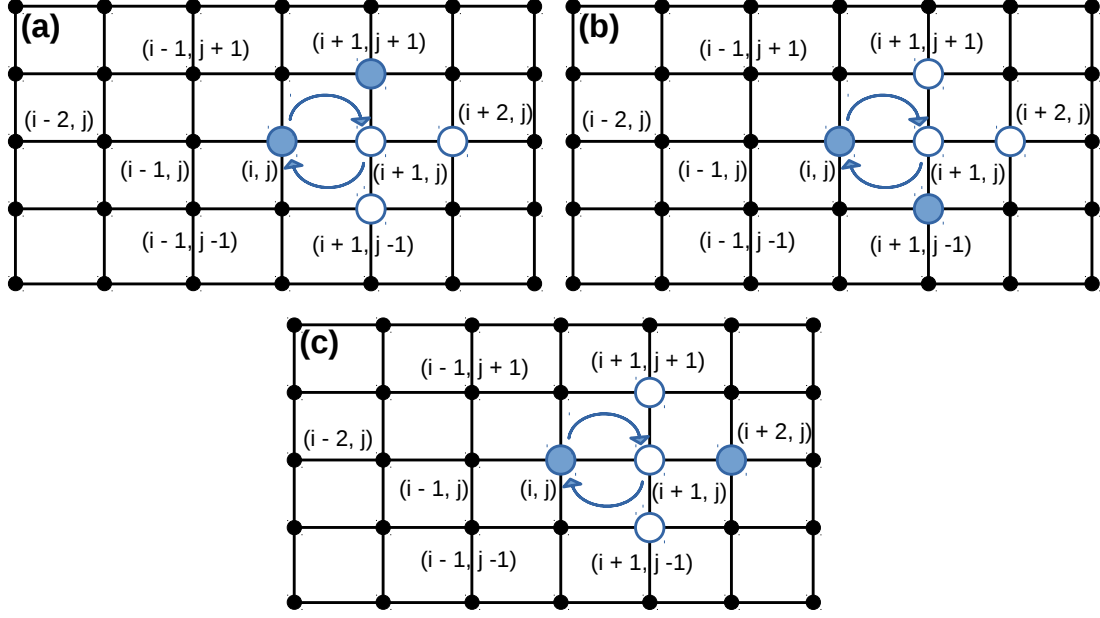


Figure 3.3: Schematic diagram for a hole at an originating site (i, j) hopping to its NN site (the intermediate site) and returning back (when any two of the NN sites of the intermediate site are occupied by electrons). Representation of a hole at (i, j) jumping to its right NN at $(i + 1, j)$ and coming back when holes occupy (a) right and downward NNs of the intermediate site; (b) right and upward NNs of the intermediate site; (c) upward and downward NNs of the intermediate site. A hole is depicted by a blue solid circle and a particle by a blue empty circle. All lattice sites that are not relevant to the consideration are represented by black solid circles.

In Fig. 3.3, we depict the three possibilities corresponding to a hole at a site (i, j) hopping to its NN site (the intermediate site) and returning; here, any two of the NN sites of the intermediate site are occupied by electrons. Henceforth, we will show all the counterpart processes of Fig. 3.2(A) (considering these as representative diagrams) for various possibilities. Similar processes, which will not be shown here, also occur for Fig. 3.2(B), Fig. 3.2(C), and Fig. 3.2(D).

When the hole virtually hops to the intermediate site, its energy is equal to $E_p + 4V_p$; here, an extra repulsion of $2V_p$ is generated due to the occupancy of any one of the NN site of the intermediate site by a hole. Then, the coefficient of the second order perturbation term is $\frac{t^2}{2E_p+4V_p}$ and the contribution to $H^{(2)}$ from all the possibilities, similar to and corresponding to Fig. 3.3, is given by

$$\begin{aligned}
H_2^{(2)} = & -\frac{t^2}{(2E_p + 4V_p)} \sum_{i,j} \left[\cos^2 \left(\frac{\theta_{i,j;i+1,j}}{2} \right) \times \right. \\
& \left\{ n_{i,j}(1 - n_{i+1,j})n_{i+2,j}(1 - n_{i+1,j+1})(1 - n_{i+1,j-1}) \right. \\
& + n_{i,j}(1 - n_{i+1,j})(1 - n_{i+2,j})n_{i+1,j+1}(1 - n_{i+1,j-1}) \\
& + n_{i,j}(1 - n_{i+1,j})(1 - n_{i+2,j})(1 - n_{i+1,j+1})n_{i+1,j-1} \Big\} \\
& + \cos^2 \left(\frac{\theta_{i,j;i-1,j}}{2} \right) \left\{ n_{i,j}(1 - n_{i-1,j})n_{i-2,j}(1 - n_{i-1,j+1})(1 - n_{i-1,j-1}) \right. \\
& + n_{i,j}(1 - n_{i-1,j})(1 - n_{i-2,j})n_{i-1,j+1}(1 - n_{i-1,j-1}) \\
& + n_{i,j}(1 - n_{i-1,j})(1 - n_{i-2,j})(1 - n_{i-1,j+1})n_{i-1,j-1} \Big\} \\
& + \cos^2 \left(\frac{\theta_{i,j;i,j+1}}{2} \right) \left\{ n_{i,j}(1 - n_{i,j+1})n_{i,j+2}(1 - n_{i-1,j+1})(1 - n_{i+1,j+1}) \right. \\
& + n_{i,j}(1 - n_{i,j+1})(1 - n_{i,j+2})n_{i-1,j+1}(1 - n_{i+1,j+1}) \\
& + n_{i,j}(1 - n_{i,j+1})(1 - n_{i,j+2})(1 - n_{i-1,j+1})n_{i+1,j+1} \Big\} \\
& + \cos^2 \left(\frac{\theta_{i,j;i,j-1}}{2} \right) \left\{ n_{i,j}(1 - n_{i,j-1})n_{i,j-2}(1 - n_{i-1,j-1})(1 - n_{i+1,j-1}) \right. \\
& + n_{i,j}(1 - n_{i,j-1})(1 - n_{i,j-2})n_{i-1,j-1}(1 - n_{i+1,j-1}) \\
& + n_{i,j}(1 - n_{i,j-1})(1 - n_{i,j-2})(1 - n_{i-1,j-1})n_{i+1,j-1} \Big\} \Big]. \tag{3.10}
\end{aligned}$$

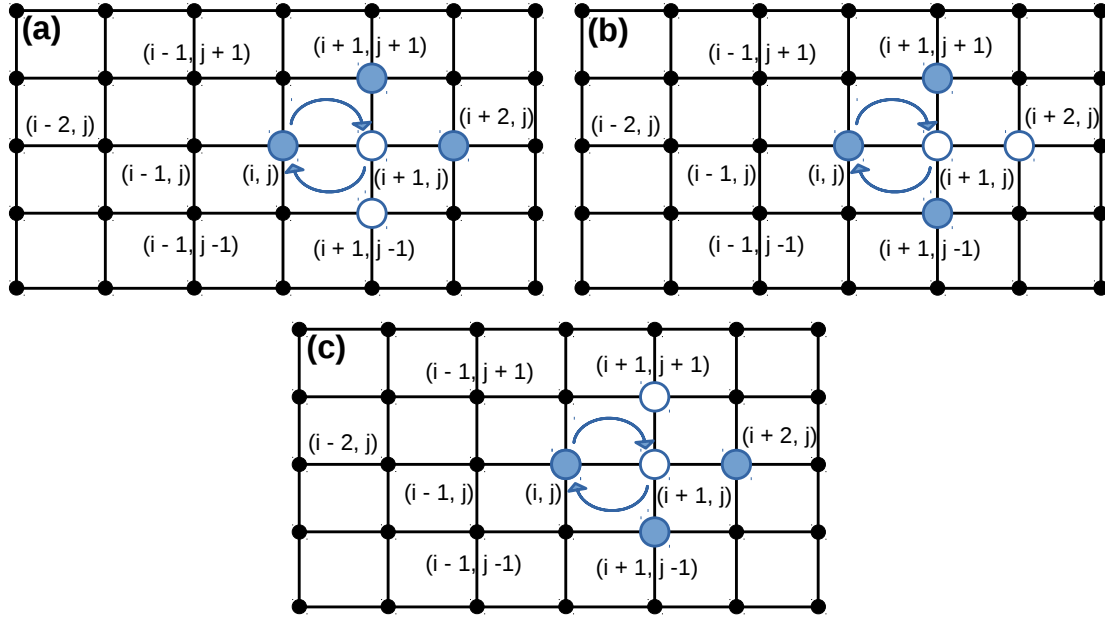


Figure 3.4: Schematic diagram for a hole at an originating site (i, j) hopping to its NN site (the intermediate site) and coming back (when any one of the NN sites of the intermediate site is occupied by an electron). Depiction of a hole at (i, j) jumping to its right NN at $(i+1, j)$ and coming back when a particle occupies (a) downward NN of the intermediate site; (b) right NN of the intermediate site; (c) upward NN of the intermediate site. A hole is represented by a blue solid circle whereas a particle by a blue empty circle. All lattice sites that are not relevant to the consideration are indicated by black solid circles.

3.2.3 Any one of NN sites of the intermediate site has an electron.

In Fig. 3.4, three possibilities have been shown for the process where a hole jumps to an intermediate site and comes back; here, any one of the NNs of the intermediate site is filled by an electron. Extending the logic given above to the present case, the coefficient of the second order perturbation term is $\frac{t^2}{2E_p+6V_p}$ and the contribution to $H^{(2)}$ from all the

possibilities, similar to and corresponding to Fig. 3.4, is given by

$$\begin{aligned}
H_3^{(2)} = & -\frac{t^2}{(2E_p + 6V_p)} \sum_{i,j} \left[\cos^2 \left(\frac{\theta_{i,j;i+1,j}}{2} \right) \left\{ n_{i,j}(1 - n_{i+1,j})n_{i+2,j}n_{i+1,j+1}(1 - n_{i+1,j-1}) \right. \right. \\
& + n_{i,j}(1 - n_{i+1,j})(1 - n_{i+2,j})n_{i+1,j+1}n_{i+1,j-1} \\
& + n_{i,j}(1 - n_{i+1,j})n_{i+2,j}(1 - n_{i+1,j+1})n_{i+1,j-1} \left. \right\} \\
& + \cos^2 \left(\frac{\theta_{i,j;i-1,j}}{2} \right) \left\{ n_{i,j}(1 - n_{i-1,j})n_{i-2,j}n_{i-1,j+1}(1 - n_{i-1,j-1}) \right. \\
& + n_{i,j}(1 - n_{i-1,j})(1 - n_{i-2,j})n_{i-1,j+1}n_{i-1,j-1} \\
& + n_{i,j}(1 - n_{i-1,j})n_{i-2,j}(1 - n_{i-1,j+1})n_{i-1,j-1} \left. \right\} \\
& + \cos^2 \left(\frac{\theta_{i,j;i,j+1}}{2} \right) \left\{ n_{i,j}(1 - n_{i,j+1})n_{i,j+2}(1 - n_{i-1,j+1})n_{i+1,j+1} \right. \\
& + n_{i,j}(1 - n_{i,j+1})(1 - n_{i,j+2})n_{i-1,j+1}n_{i+1,j+1} \\
& + n_{i,j}(1 - n_{i,j+1})n_{i,j+2}n_{i-1,j+1}(1 - n_{i+1,j+1}) \left. \right\} \\
& + \cos^2 \left(\frac{\theta_{i,j;i,j-1}}{2} \right) \left\{ n_{i,j}(1 - n_{i,j-1})n_{i,j-2}n_{i-1,j-1}(1 - n_{i+1,j-1}) \right. \\
& + n_{i,j}(1 - n_{i,j-1})(1 - n_{i,j-2})n_{i-1,j-1}n_{i+1,j-1} \\
& + n_{i,j}(1 - n_{i,j-1})n_{i,j-2}(1 - n_{i-1,j-1})n_{i+1,j-1} \left. \right\} \Bigg]. \tag{3.11}
\end{aligned}$$

3.2.4 All the NN sites of the intermediate site have holes.

Here, for the situation where all the NN sites of the intermediate site have holes, we depict in Fig. 3.5 a hole hopping to an intermediate site and coming back.

Here, the coefficient of the second order perturbation term is $\frac{t^2}{2E_p+8V_p}$ and the contribution to $H^{(2)}$ from all the possibilities, similar to and corresponding to Fig. 3.5, is given by

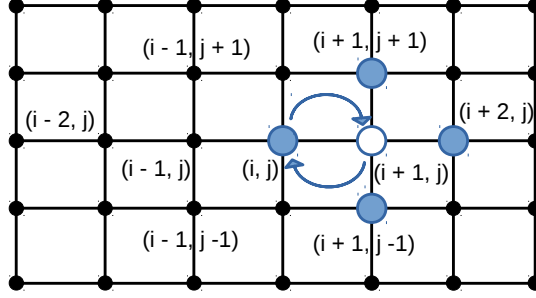


Figure 3.5: Schematic diagram for a hole at an originating site (i, j) hopping to its NN site (the intermediate site) and coming back (when all the other three NN sites of the intermediate site are occupied by electrons). Representation of a hole at (i, j) jumping to its right NN at $(i + 1, j)$ and coming back. A hole is represented by a blue solid circle and a particle by a blue empty circle. All lattice sites irrelevant to the analysis are represented by black solid circles.

$$\begin{aligned}
H_4^{(2)} = & -\frac{t^2}{(2E_p + 8V_p)} \sum_{i,j} \left[\cos^2 \left(\frac{\theta_{i,j;i+1,j}}{2} \right) \left\{ n_{i,j} (1 - n_{i+1,j}) n_{i+2,j} n_{i+1,j+1} n_{i+1,j-1} \right\} \right. \\
& + \cos^2 \left(\frac{\theta_{i,j;i-1,j}}{2} \right) \left\{ n_{i,j} (1 - n_{i-1,j}) n_{i-2,j} n_{i-1,j+1} n_{i-1,j-1} \right\} \\
& + \cos^2 \left(\frac{\theta_{i,j;i,j+1}}{2} \right) \left\{ n_{i,j} (1 - n_{i,j+1}) n_{i,j+2} n_{i-1,j+1} n_{i+1,j+1} \right\} \\
& \left. + \cos^2 \left(\frac{\theta_{i,j;i,j-1}}{2} \right) \left\{ n_{i,j} (1 - n_{i,j-1}) n_{i,j-2} n_{i-1,j-1} n_{i+1,j-1} \right\} \right]. \quad (3.12)
\end{aligned}$$

From the contributions $H_1^{(2)}$, $H_2^{(2)}$, $H_3^{(2)}$, and $H_4^{(2)}$ obtained above, we express $H^{(2)}$ as

$$H^{(2)} = H_1^{(2)} + H_2^{(2)} + H_3^{(2)} + H_4^{(2)}. \quad (3.13)$$

Lastly, the superexchange [144] term H_{SE} generates A-AFM spin-spin exchange in

manganites such as LaMnO_3 and is given by

$$H_{\text{SE}} = -J_{\text{xy}} \sum_{\langle i,j \rangle_{\text{xy}}} \cos(\theta_{ij}) + J_z \sum_{\langle i,j \rangle_z} \cos(\theta_{ij}). \quad (3.14)$$

It is important to note that, while the range of charge-charge interaction is as far as NNNN, the range of spin-spin interaction is only NN.

3.3 Calculation procedure

For a numerical study, we consider a 2D lattice with periodic boundary conditions in both directions. We treat the problem fully classically using the effective Hamiltonian, comprised of the effective electron-phonon interaction (the charge-spin-coupled term) and the superexchange interaction (the spin-spin interaction term), as given by Eq. (3.8). We use classical Monte Carlo technique and make use of the standard Metropolis algorithm to update the charge configuration as well as the spin configuration of the system. We follow a two-step procedure to arrive at the final charge and spin configurations.

Firstly, to deal with problem of charge configurations that correspond to local minima which are close in energy, we take resort to simulated annealing for the charge degrees of freedom only. The spin variables are kept frozen since the energy scale for the charge interactions is much higher than the energy scale for superexchange interactions. Since we are working with low hole densities (i.e., between 0.1 and 0.3), a large number of degenerate states will appear in the charge spectrum. In order to obtain maximum number of such degenerate configurations, we employ a three-step procedure at each temperature of the simulated annealing process to obtain the optimized charge configurations. The primary step is a “single-particle-exchange” process where we choose any two sites at a

time—one sequentially and the other randomly—and exchange their number density values provided they differ by 1. Physically we exchange a particle at a site with a hole at any other site. The secondary step is a “general-two-particle-exchange” process where any two random sites are selected with both being occupied by particles and then their occupants are exchanged with another pair of randomly chosen sites both containing holes. Thus we actually exchange two particles with two holes at a time. The final step—a “plaquette-exchange” process—is a special case of the “general-two-particle-exchange” mechanism. Here plaquette are chosen sequentially; if the difference in number densities between the two diagonal pairs is 2, then the number densities of the diagonals are exchanged. At a particular temperature, to arrive at the final lowest energy charge configuration at that temperature using Monte Carlo technique, an initial random charge configuration (with a fixed number of particles) first goes through 4×10^5 steps of “single-particle-exchange”; then an equal number of steps involving “general-two-particle-exchange”; followed by 30 times the system size number “plaquette-exchange” steps.

Secondly, using the charge profile generated by the three-step process, we now optimize spin variables by taking an initial random spin configuration and updating through the Metropolis algorithm. The spins being large in magnitude, with $S = 2$, are essentially classical spins with $\vec{S}_i = (\sin \theta_i \cos \phi_i, \sin \theta_i \sin \phi_i, \cos \theta_i)$. While updating the spins, we consider the full Hamiltonian H_{eff} and consider both the charge and spin interaction energies. The $\cos(\theta)$ and ϕ values are binned to fix the orientation of the classical spin vector. We have allowed equally spaced 40 values of $\cos(\theta)$ in the interval $(-1, 1)$ and 80 values of ϕ in the usual range of $(0, 2\pi)$, thus totaling to 3200 different possibilities. A sweep involves visiting all the lattice sites sequentially and updating the spin orientation at each lattice site by the Metropolis algorithm. The equilibrium number of sweeps required for medium (higher) temperatures is around 15×10^5 (6×10^5), while another 15×10^5

(6×10^5) sweeps are required for the thermal averaging of the total magnetization of the system. It is to be noted that for low hole concentrations, we have many degenerate states. We calculate the magnetization for typically 10 degenerate configurations. The degenerate states are chosen based on the charge optimization process only, fed to the full Hamiltonian H_{eff} containing both charge and spin variables, and then energy is optimized to obtain the total magnetization of all such states. The magnetization/site of the system, that has been plotted, is the magnetization/site averaged over all the degenerate states for a particular filling of holes when spins normalized to unity.

We study the system for the bare hopping parameter values $t = 0.2$ eV and $t = 0.3$ eV. Our calculations take the polaronic energy to be $E_p = 0.43$ eV and the nearest-neighbor repulsion energy to be $V_p = 0.07$ eV. Thus, we are in the regime of strong electron-phonon coupling characterized by $(E_p + V_p)/\omega_0 \gg 1$ with the optical phonon frequency ω_0 value being given as $0.05 \text{ eV} < \omega_0 < 0.1 \text{ eV}$. The superexchange energy coefficient $J_z = 4.8$ meV [134, 138–140]; thus the superexchange energy is much smaller than the electron-hole pair ferromagnetic interaction coupling $[t^2/(2E_p + 2V_p)]$. Furthermore, the ferromagnetic coupling $J_{xy} = 1.4 \times J_z$. Thus, the charge configuration can be assumed to remain constant as the spins are optimized. The total magnetization of the system is computed at various temperatures, with the highest temperature being $T = 0.1t/k_B$ (i.e., about 330K for $t = 0.3$ eV). Henceforth, k_B will be set to unity for convenience.. The lowest temperature on the other hand is $T = 0.001t$ (i.e., about 3K for $t = 0.3$ eV) which is much smaller than J_z ; thus, the system can be assumed to be in its ground state at $T = 0.001t$. Here, we should comment that above $T = 0.03t$, the excited-state charge configurations also begin to contribute to the magnetization.

3.4 Results and discussion

We consider a 2D lattice of dimensions 6×12 , (i.e., with a total of 72 sites) with periodic boundary conditions in both directions; the number of rows being $l_x = 6$ and the number of columns being $l_y = 12$. Each site represents an Mn ion consisting of an electron and a positive charge center. We study the interplay between the electron-phonon interaction and the magnetic interaction of the spins [see Eq. (3.8)]. As stated earlier (in Sec. 3.1), due to the smallness of the kinetic energy in comparison to the potential energy, the problem is treated fully classically. Thus the holes are site-localized and the system can be represented by a single state in the occupation number basis with the number density at each site being either 1 or 0. Hence, for strong electron-phonon interaction, we have a fully insulating system resembling a charge solid as shown in Fig. 3.7. Using effective Hamiltonian in Eq. (3.8), we can simulate different observables in the system. We study the variation of the total magnetization of the system as a function of hole doping in the pure manganite sample.

3.4.1 A-AFM background

The hopping value t is varied to study the interplay between the electron-phonon interactions and the superexchange interactions in the system. The hole doping x is varied as $0.1 \leq x \leq 0.3$. The magnetic profile still resembles that of an A-AFM system away from the holes; in the NN vicinity of a hole, the spins get polarized in the direction of the spin of the hole thereby forming a magnetic polaron. For different hopping cases, the temperature variation of the total magnetization of the system is studied. We have also considered a 2D lattice with system size 12×12 and carried out the magnetization measurements. It shows

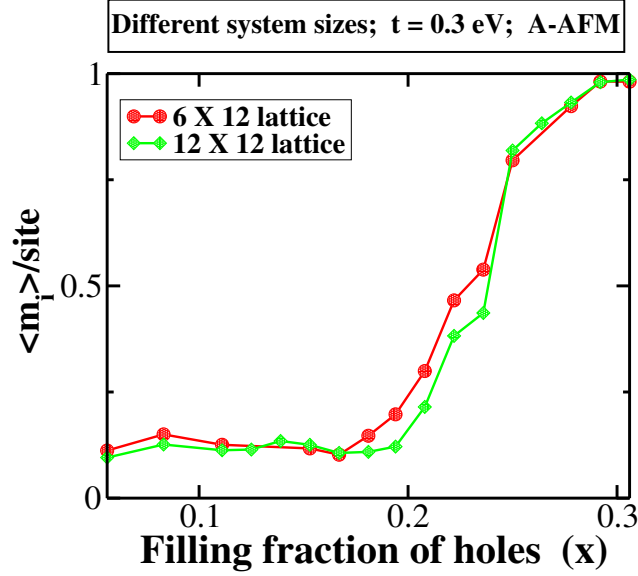


Figure 3.6: Averaged per-site magnetization $\langle m_i \rangle$ (of spins normalized to unity) as a function of hole doping x for two different lattices (6×12 and 12×12) and for a fixed $T = 0.001t$.

qualitatively similar results as that of the 6×12 lattice as depicted in Fig. 3.6. However, the 12×12 system requires a running time which is $\simeq 5$ times that of the 6×12 case; also, the number of degenerate states for the 12×12 system is much more. Thus, dealing with the 12×12 case is computationally expensive. So, we conclude that 6×12 lattice can be considered to be representative for the 12×12 lattice and will be used for investigating the ferromagnet-insulator properties of the system.

At a very low-hole concentration $\simeq 0.1$ (i.e., 8 particles on a 72-site lattice), 8 holes get distributed among 12 columns such that NN as well as NNN and NNNN interactions are avoided. In most of the degenerate states, no two holes occupy the same column. Hence we have site-localized holes in the system, polarizing their NN spins, giving rise to magnetic polarons that remain disconnected in the lattice. Due to the NN interaction J_{xy} , spins in a column try to align ferromagnetically. Thus, the ferromagnetic polarons and the ferro-

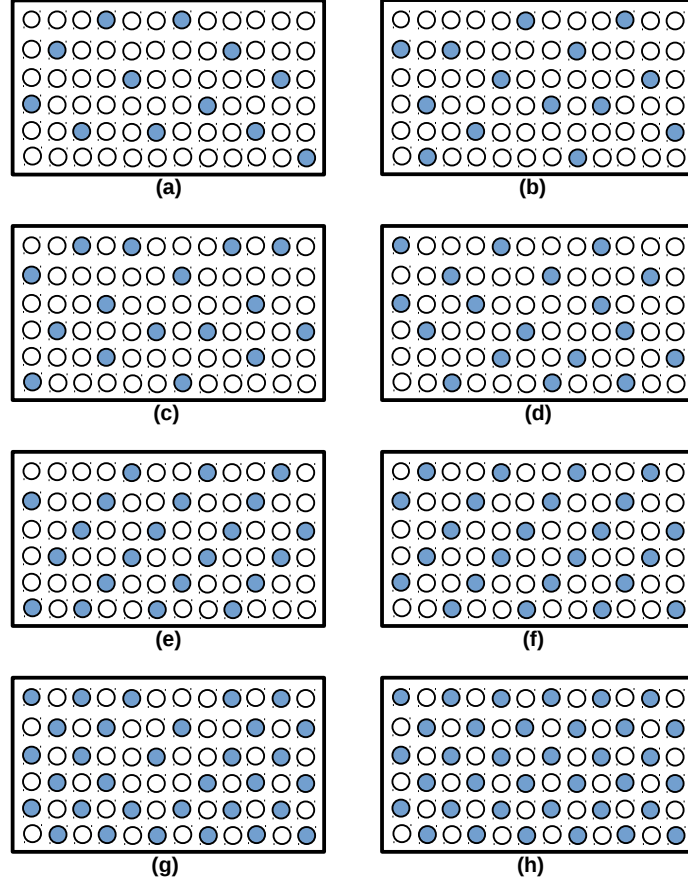


Figure 3.7: Charge configurations in the ground state of a 6×12 lattice. An arbitrarily chosen degenerate ground state, involving 72 sites, for (a) 12 holes, (b) 14 holes, (c) 16 holes, (d) 18 holes, (e) 22 holes, (f) 24 holes (diagonal stripe order), (g) 32 holes, and (h) 36 holes.

magnetic interaction in columns together give rise to an effective low magnetization value (with a sizeable fluctuation) .

At each temperature, the value of magnetization is essentially unchanged between hole densities $8/72$ and $12/72$ ($\simeq 0.167$); this is because up to the filling $12/72$, holes can still maintain to be non-interacting (on ignoring the superexchange) as can be seen in Fig. 3.7 (a).

At temperatures $T < J_z$ ($= 0.016t$ for $t = 0.3$ eV and $= 0.024t$ for $t = 0.2$ eV), antiferromagnetic coupling between columns is effective and the system has low magnetization at low concentrations (i.e., $x \leq 12/72$). On increasing the temperature up to $T = J_z$, the effect of J_z diminishes while the effect of ferromagnetic coupling $J_{xy} = 1.4J_z$ is more dominant; thus, magnetism in the system increases with increasing temperature. For higher temperatures $T > J_{xy}$ and again at low concentrations (i.e., $x \leq 12/72$), the effect of the ferromagnetic coupling J_{xy} also diminishes, and the magnetism decreases with increasing temperature.

3.4.1.1 $t=0.3$ eV case

As the concentration of holes increases, initially NNNN interactions and later NNN interactions become relevant; the NN interactions being the strongest are still avoided. Thus longer ferromagnetic chains are formed, thereby increasing the total magnetization of the system. So by $x = 14/72 \simeq 0.194$ [see Fig. 3.7 (b)], magnetization for lower temperatures such as $T = 0.001t$ starts rising sizeably; the peak magnetization value is now at a reduced temperature of $T = 0.01t$. By $x = 18/72 = 0.25$ [see Fig. 3.7 (d)] NNN interactions also appear, the different local magnetic polarons start interacting with one another and hence form larger magnetic polarons and the peak magnetization temperature reduces to $T=0.001t$; here, starting from $T = 0.1t$, the magnetization increases with decreasing temperature. It is to be noted that there occurs a narrow crossing region ($14/72 \leq x \leq 17/72$) where magnetization curves for different temperatures intersect. In the crossing regime, there is a complex interplay of various competing effects: 1) aligning of different magnetic polarons due to dominance of J_{xy} over J_z ; 2) reduction of electron-hole spin interactions due to appearance of NNNN and NNN interactions (of strength $\frac{t^2}{2E_p+4V_p}$); 3) commencing of percolation effects of magnetic polarons due to large hole concentrations; and 4) disor-

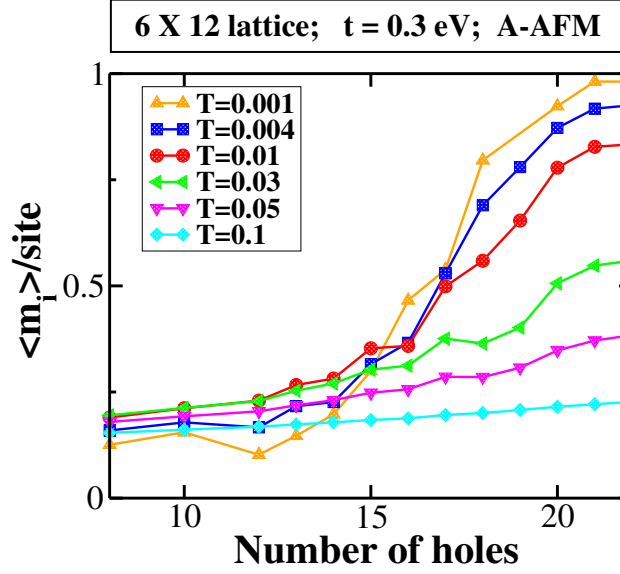


Figure 3.8: Averaged per-site total magnetization $\langle m_i \rangle$ (of spins normalized to unity) as a function of the number of holes doped for a 6×12 lattice and for various temperatures (expressed in units of hopping parameter t). The background spin configuration is A-AFM type and hopping $t = 0.3$ eV.

dering effects of the temperature. At $x = 18/72$ ($= 0.25$), percolation effect of magnetic polarons is largely dominant over antiferromagnetic interactions. At even higher hole concentrations, this effect is even more pronounced; magnetization rises faster with lowering of temperature. As can be seen from Fig. 3.8, at lower temperatures and for $x > 15/72$, the magnetization increases faster with increasing hole concentration. At $T = 0.001t$, we get an almost fully ferromagnetic large cluster for $x = 22/72 \simeq 0.3$ [see Fig. 3.7 (e)], with averaged magnetization values close to the maximum possible.

3.4.1.2 $t=0.2$ eV case

For the $t = 0.2$ eV situation, the crossing region (i.e., $13/72 \leq x \leq 19/72$) is wider than it is for the $t = 0.3$ eV case. The peak-magnetization temperature oscillates in the crossing regime (see Fig. 3.9); furthermore, the curves corresponding to $T \lesssim J_z = 0.024t$

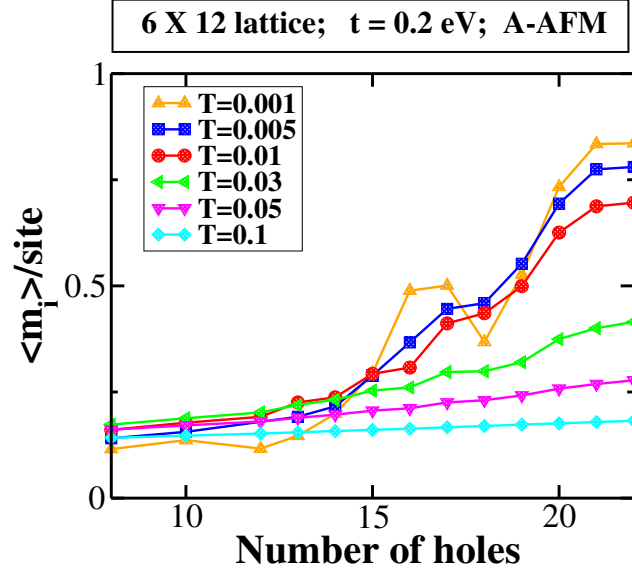


Figure 3.9: Averaged per-site total magnetization $\langle m_i \rangle$ (of spins normalized to unity) as a function of the number of holes doped for a 6×12 lattice and for various temperatures (in units of hopping t). The background spin configuration is A-AFM and $t = 0.2$ eV.

intersect more than once in the crossing region. A plausible explanation for this can be given as follows. The ratio of electron-hole spin interaction and antiferromagnetic coupling $\left[\left(\frac{t^2}{2E_p + 2V_p} \right) / J_z \right]$ is only 8; when NNN and NNNN interactions are relevant, the ratio reduces to $\left(\frac{t^2}{2E_p + 4V_p} \right) / J_z = 7$. Thus antiferromagnetic coupling becomes more prominent than for the $t = 0.3$ eV case and frustration effects become relevant.

It could be due to frustration that, at lower temperatures (such as $T = 0.001t$), the magnetization curve drops at the higher carrier concentration $x = 18/72 = 0.25$. This also could be an indication of the superspin glass phase claimed in experiments [49]; here, “superspin” refers to a spin cluster (i.e., a large magnetic polaron). At $x \geq 20/72 (\simeq 0.28)$, percolation effect of magnetic polarons dominates over antiferromagnetic interactions; magnetization rises with lowering of temperature. Finally, for the higher hole concentration $x = 22/72 \simeq 0.3$ and at $T = 0.001t$, we get a reasonably high magnetization value of 0.85.

3.4.2 G-AFM background, $t = 0.3$ eV case

To gain further insight, we study the interplay between the strong ferromagnetic electron-hole interaction that polarizes the NN spins of a hole and the superexchange NN antiferromagnetic interaction J_z . The magnetic profile, away from the holes, resembles that of a G-AFM system; the holes form ferromagnetic polarons involving the hole spin and the NN spins. At temperatures $T \lesssim J_z = 0.016t$ and hole fillings up to $x = 24/72$, due to the effect of antiferromagnetic J_z coupling on all sides, the polarizations of the magnetic polarons oppose each other leading to a low magnetization as shown in Fig. 3.10. For higher temperatures, due to the dominance of the disordering effect of the temperature over the superexchange interaction, there is a probability for the clusters to get less misaligned. Hence we notice an increase in the magnetization for $T > J_z$. For $x = 24/72 = 1/3$, we have a diagonal stripe order as depicted in Fig. 3.7 (f); each column has two holes. For this arrangement, diagonals containing holes are ferromagnetic, but every such diagonal (with holes) is antiferromagnetically coupled to its neighboring diagonal. In each column, half the spins are in one direction while the other half are in the opposite direction leading to a very small total magnetization.

Here too, very similar to the case of $t = 0.2$ eV with A-AFM background, there is a crossing region; the crossing occurs in the region $24/72 < x < 32/72$. In the crossing regime, the peak-magnetization temperature oscillates and the curves for $T \lesssim Jz$ intersect thrice in the crossing region. Since all the background spins interact antiferromagnetically (which is in contrast to the A-AFM case), percolation of magnetic polarons dominates over antiferromagnetic interactions at an even larger filling; around $x \geq 32/72 = 0.44$ [refer Fig. 3.7 (g)], magnetization increases with lowering of temperature.. It is to be noted that,

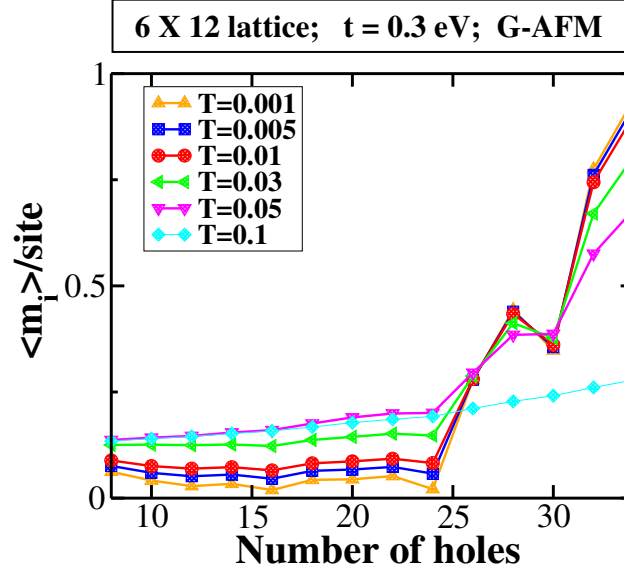


Figure 3.10: Averaged per-site total magnetization $\langle m_i \rangle$ (of spins normalized to unity) as a function of the number of holes doped for a 6×12 lattice and for various fixed temperatures (in units of hopping parameter t). The background spin configuration is G-AFM type and $t = 0.3$ eV.

for half-filling [see Fig. 3.7 (h)], we should expect a fully ferromagnetic spin profile with a checkerboard charge structure. [37]

3.4.3 Fully FM background, $t = 0.3$ eV

Lastly, to better appreciate subtleties pertaining to FMI, we also study the case where the superexchange interaction is fully ferromagnetic (FM) with coupling $J_z = 0.016t$ when $t = 0.3$ eV. Here, while in the NN vicinity of a hole the spins get strongly polarized thereby forming a ferromagnetic magnetic polaron, the magnetic profile is that of a weaker FM system away from the holes. Hence, for temperatures much smaller than J_z (such as $T = 0.001t$), we have an almost fully ferromagnetic system as shown in Fig. 3.11, On increasing the temperature, the spins get more misaligned and the magnetization reduces.

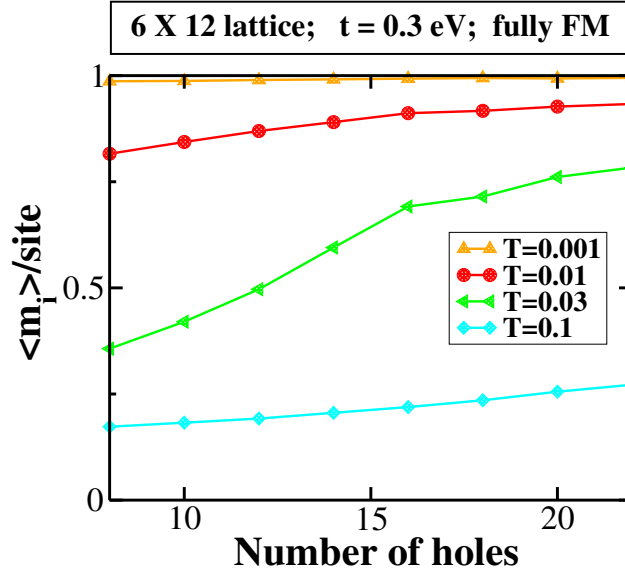


Figure 3.11: Averaged per-site total magnetization $\langle m_i \rangle$ (of spins normalized to unity) as a function of the number of holes doped for a 6×12 lattice and for various fixed temperatures (in units of hopping parameter t). The background spin configuration is fully FM and $t = 0.3 \text{ eV}$.

At lower fillings, as the temperature increases to the value $0.03t$ (i.e., $T \approx 2J_z$), the disordering effect is large enough so that the magnetization drops considerably as shown in Fig. 3.11; On the other hand, at higher fillings and again at $T = 0.03t$, percolation of magnetic polarons counters the disordering effect and generates higher magnetization values. For still higher temperatures (such as $T = 0.1t$), the magnetic polarons tend to orient in random directions because the superexchange coupling is ineffective, thereby reducing the magnetization significantly. It is interesting to note that, in all the three Figs. 3.8, 3.10, and 3.11 plotted at $t = 0.3 \text{ eV}$, the magnetization curves are similar because the superexchange is ineffective and hence the nature of superexchange coupling is irrelevant.

3.5 Conclusions and perspectives

We studied the nature of ferromagnetic insulator in the experimentally relevant doping regime of $0.1 \leq x \leq 0.3$ in bulk manganites. The magnetic interaction considered here applies to manganites with low density of localized holes. In regions without holes, as in the undoped manganites, the magnetic interaction is A-AFM; in a region with a hole, the site-localized hole produces strong ferromagnetic coupling between its spin and its NN electron spins. We find that near the doping $x = 0.3$, the insulator is almost fully ferromagnetic. Now, the critical doping at which the system becomes fully ferromagnetic depends on the dimension; in 2D it is expected to be around twice the value of the critical doping in three dimensions (3D) for the following reason. In a conducting-site percolation problem, the critical concentration for conduction in a simple cubic lattice is 0.31 and in a square lattice it is 0.59 [see Ref. [163]]; hence, the critical doping to produce a percolating cluster that is a checkerboard charge-ordered region is 0.5×0.31 in 3D and at 0.5×0.59 in 2D [see Ref. [48]].

It was experimentally observed that a FMI phase is manifested in the wide-band manganite $\text{La}_{1-x}\text{Sr}_x\text{MnO}_3$ in the doping region $0.1 \lesssim x \lesssim 0.18$ [43], in the intermediate-bandwidth $\text{La}_{1-x}\text{Ca}_x\text{MnO}_3$ in the doping range $0.1 \leq x \leq 0.225$ [43, 44], and in the narrow-bandwidth $\text{Pr}_{1-x}\text{Ca}_x\text{MnO}_3$ in the region $0.1 \leq x \leq 0.3$ [43]. The fact that the FMI region persists till a higher doping when bandwidth decreases (and concomitantly electron-phonon coupling increases [123]) is consistent with the fact that the tendency to localize increases as bandwidth decreases [45–47]. The hopping values considered in this work are pertinent to wide-bandwidth and intermediate-bandwidth manganites. While our one-band model (involving site-localized holes) is relevant to understand manganites in the FMI region, it is certainly not valid to study the ferromagnet metallic (FMM) phase that

occurs at higher doping in manganites; to understand the FMM region, we need to invoke a two-band model and/or analyze the effect of disorder on localization.

The experimental managanite phase diagram reported in Ref. [164] reveals increasing T_c values at higher dopings for the FMI phase in $\text{La}_{1-x}\text{Sr}_x\text{MnO}_3$. Based on this phase diagram, for a fixed $T < T_c(x = 0.1)$, we expect the magnetization to increase when the doping increases in the FMI region; this is consistent with the curves in Fig. 3.8.

Lastly, comparing the $t = 0.2$ eV, A-AFM case with the $t = 0.3$ eV, G-AFM case, we conclude that the antiferromagnetic coupling J_z plays the important role of causing frustrations in the system. We also point out the possible occurance of glassiness in the system to explain the multiple intersections of the curves in the crossing regime at $T \lesssim J_z$ (see Figs. 3.9 and 3.10). Such a picture is supported by the observed superspin glass phase in $\text{La}_{0.82}\text{Ca}_{0.18}\text{MnO}_3$ ferromagnetic insulator at $T \lesssim 70$ K [49]. Further theoretical analysis is required to clearly identify and characterize a superspin glass phase at lower temperatures.

CHAPTER 4

SUMMARY

A property of heterostructures is the transfer of charge across the interface that brings about changes in collective phases at the interface and affects electronic and transport behaviors. The goal is to tune the different degrees of freedom so that the interface can reconstruct itself electronically and magnetically and generate novel phenomena such as the occurrence of a 2DEG, metal-insulator phase transitions, multiferroicity, magnetoelectricity, etc. Starting from this broader perspective about the potential of oxide heterostructures, this thesis demonstrates the importance of cooperative electron-phonon interaction in the transfer of electrons across the interface of manganite-manganite heterostructures. This work principally concentrates on two, out of many, of the prototypical characteristics of manganites: (1) the coupling between the diverse degrees of freedom (such as spin, charge, orbital and lattice) and (2) the expansion of one magnetic phase at the expense of another magnetic phase by tuning the charge degrees of freedom. The thesis also offers a mechanism for the not-well-understood ferromagnetic insulating phase that is realized in bulk manganites and plays a central role in our predicted magnetoelectric effect in manganite-manganite

heterostructures. The FMI phase is explained by incorporating cooperative electron-phonon interaction physics as a necessary ingredient.

In *Chapter 2*, a demonstration of a giant magnetoelectric effect (at temperatures comparable to the boiling point of liquid helium) is done on the manganite heterostructure (Insulator)/(LaMnO₃)_n/Interface/(CaMnO₃)_n/(Insulator) [37]. We study the pure manganite-manganite heterostructure using both a simple analytic picture and a more detailed numerical approach. We show that a sizable fraction of charges, from a few layers near the interface, can be transferred across the interface. In the analytic approach, a continuum approximation is invoked and the charge distribution is obtained by considering only the potential energy involving electron-phonon physics and Coulombic interaction. On the other hand, the numerical treatment involves a more realistic lattice model and due attention is paid to the kinetic energy term as well. We employ classical Monte Carlo along with simulated annealing to arrive at the charge and magnetic profiles. By transferring electrons from the LaMnO₃ side to the CaMnO₃ side, using a sizable external electric field, we realize a giant magnetoelectric effect by enhancing the ferromagnetic insulating region at the expense of the A-AFM region on the LMO side and the G-AFM region on the CMO side. It is of interest to note that the giant magnetoelectric effect (predicted by us) was missed by the authors of Ref. [32]. In future, we would like to identify which oxide heterostructures can give the best magnetoelectric effect at elevated temperatures as close to room temperature as possible. Also, employing the CEPI framework developed in this work, we would like to study other oxide heterostructures (with different geometries) for new interesting phenomena.

Ferromagnetic insulators are highly needed for many novel magnetic devices, such as dissipationless quantum-spintronic devices, magnetic tunneling junctions, etc. *Chapter 3* offers a mechanism for the enigmatic FMI region [42] that occurs in phase diagrams of

intermediate- and narrow-bandwidth manganites at low-hole concentrations (varying between 0.1 and 0.3). Invoking cooperative electron-phonon-interaction physics and double exchange and superexchange processes in a localized system, an effective Hamiltonian is obtained involving charge and spin degrees of freedom. We get an effective intermediate-range electron-electron repulsion due to cooperative breathing mode distortions; incorporating double exchange mechanism produces a strong ferromagnetic interaction between a hole and its neighboring electrons leading to magnetic polarons. When the magnetic polarons increase in number due to doping, they coalesce and generate a ferromagnetic insulator. An exciting revelation is that, at intermediate dopings, magnetization curves (calculated at various temperatures using Monte Carlo simulations) intersect. Before the crossing, non-interacting holes produce isolated ferromagnetic clusters; after the crossing, percolation fully commences making the system highly ferromagnetic. In the crossing regime, there is a complex interplay of ferromagnetic and antiferromagnetic components of the superexchange interaction; density dependence of electron-hole ferromagnetic interaction; percolation of magnetic polarons; and disordering effects of temperature. Ferromagnetism in the system gets enhanced at higher dopings or when the ratio hopping/polaronic-energy dominates over the ratio superexchange-coupling/hopping. In future, the crossing regime (disclosed by our calculations) needs to be analyzed for a possible spin-glass phase (see Ref. [49]).

BIBLIOGRAPHY

- [1] M.-K. Lee and S. M. Sze, *Semiconductor Devices: Physics and Technology*, 3rd Edition. John Wiley & Sons, (2012). [i](#)
- [2] J. Mannhart and D. G. Schlom, *Oxide interfaces—an opportunity for electronics*, *Science* **327** (2010) 1607–1611. [i](#)
- [3] H. Boschker and J. Mannhart, *Quantum-Matter Heterostructures*, *Annual Review of Condensed Matter Physics* **8** (2017) 145–164. [i](#)
- [4] H. Takagi and H. Y. Hwang, *An Emergent Change of Phase for Electronics*, *Science* **327** (2010) 1601–1602. [i](#)
- [5] G. Hammerl and N. Spaldin, *Shedding Light on Oxide Interfaces*, *Science* **332** (2011) 922–923. [i](#)
- [6] Hwang H. Y., Iwasa Y., Kawasaki M., Keimer B., Nagaosa N. and Tokura Y., *Emergent phenomena at oxide interfaces*, *Nature Materials* **11** (Jan, 2012) 103. [i](#), [3](#), [6](#), [7](#)
- [7] E. Dagotto, *When Oxides Meet Face to Face*, *Science* **318** (2007) 1076–1077. [i](#)

- [8] L. Martin and R. Ramesh, *Multiferroic and magnetoelectric heterostructures*, *Acta Materialia* **60** (2012) 2449–2470. [i](#)
- [9] T. Chatterji, *Colossal Magnetoresistive Manganites*. Springer, Dordrecht, 2004, <https://doi.org/10.1007/978-94-015-1244-2>. [i](#), [iv](#), [51](#), [82](#)
- [10] C. Martin, A. Maignan, M. Hervieu and B. Raveau, *Magnetic phase diagrams of $L_{1-x}A_xMnO_3$ manganites ($L = Pr, Sm$; $A = Ca, Sr$)*, *Phys. Rev. B* **60** (Nov, 1999) 12191–12199. [i](#), [iv](#), [26](#), [28](#), [82](#)
- [11] N. F. Mott and R. Peierls, *Discussion of the paper by de Boer and Verwey*, *Proceedings of the Physical Society* **49** (1937) 72. [ii](#)
- [12] N. F. Mott, *The Basis of the Electron Theory of Metals, with Special Reference to the Transition Metals*, *Proceedings of the Physical Society. Section A* **62** 416. [ii](#)
- [13] N. F. Mott, *Metal-insulator transitions / N. F. Mott*. Taylor & Francis ; Barnes & Noble Books London : New York, 1974. [ii](#)
- [14] D. I. Khomskii, *Transition Metal Compounds*. Cambridge University Press, 2014, [10.1017/CBO9781139096782](https://doi.org/10.1017/CBO9781139096782). [iii](#)
- [15] C. N. R. Rao and B. Raveau, *Colossal Magnetoresistance, Charge Ordering and Related Properties of Manganese Oxides*. WORLD SCIENTIFIC, 1998, [10.1142/3605](https://doi.org/10.1142/3605). [iv](#), [81](#)
- [16] M. B. Salamon and M. Jaime, *The physics of manganites: Structure and transport*, *Rev. Mod. Phys.* **73** (Aug, 2001) 583–628. [iv](#)
- [17] E. Dagotto, T. Hotta and A. Moreo, *Colossal magnetoresistant materials: the key role of phase separation*, *Physics Reports* **344** (2001) 1 – 153. [iv](#), [25](#)

- [18] Y. Tokura, *Critical features of colossal magnetoresistive manganites*, *Reports on Progress in Physics* **69** (2006) 797. [iv](#), [82](#)
- [19] J. P. Velev, S. S. Jaswal and E. Y. Tsymbal, *Multi-ferroic and magnetoelectric materials and interfaces*, *Philosophical Transactions of the Royal Society of London A: Mathematical, Physical and Engineering Sciences* **369** (2011) 3069–3097. [iv](#), [36](#)
- [20] A. Bhattacharya, S. J. May, S. G. E. te Velhuis, M. Warusawithana, X. Zhai, B. Jiang et al., *Metal-Insulator Transition and Its Relation to Magnetic Structure in $(LaMnO_3)_{2n}/(SrMnO_3)_n$ superlattices*, *Phys. Rev. Lett.* **100** (Jun, 2008) 257203. [iv](#), [8](#), [39](#), [80](#)
- [21] S. Smadici, P. Abbamonte, A. Bhattacharya, X. Zhai, B. Jiang, A. Rusydi et al., *Electronic reconstruction at $SrMnO_3$ – $LaMnO_3$ Superlattice Interfaces*, *Phys. Rev. Lett.* **99** (Nov, 2007) 196404. [iv](#)
- [22] S. J. May, A. B. Shah, S. G. E. te Velhuis, M. R. Fitzsimmons, J. M. Zuo, X. Zhai et al., *Magnetically asymmetric interfaces in a $(LaMnO_3)_m/(SrMnO_3)_{2m}$ superlattice due to structural asymmetries*, *Phys. Rev. B* **77** (May, 2008) 174409. [iv](#)
- [23] A. Bhattacharya, X. Zhai, M. Warusawithana, J. N. Eckstein and S. D. Bader, *Signatures of enhanced ordering temperatures in digital superlattices of $(LaMnO_3)_m/(SrMnO_3)_{2m}$* , *Applied Physics Letters* **90** (2007) 222503. [iv](#)
- [24] C. Adamo, X. Ke, P. Schiffer, A. Soukiassian, M. Warusawithana, L. Maritato et al., *Electrical and magnetic properties of $(SrMnO_3)_n/(LaMnO_3)_{2n}$ superlattices*, *Applied Physics Letters* **92** (2008) 112508. [iv](#)

- [25] T. Koida, M. Lippmaa, T. Fukumura, K. Itaka, Y. Matsumoto, M. Kawasaki et al., *Effect of a-site cation ordering on the magnetoelectric properties in $[LaMnO_3]_m/(SrMnO_3)_n$ artificial superlattices*, *Phys. Rev. B* **66** (Oct, 2002) 144418. [iv](#)

- [26] H. Yamada, M. Kawasaki, T. Lottermoser, T. Arima and Y. Tokura, *$LaMnO_3/SrMnO_3$ interfaces with coupled charge-spin-orbital modulation*, *Applied Physics Letters* **89** (2006) 052506. [iv](#)

- [27] Monkman Eric J., Adamo Carolina, Mundy Julia A., Shai Daniel E., Harter John W., Shen Dawei et al., *Quantum many-body interactions in digital oxide superlattices*, *Nature Materials* **11** (aug, 2012) 855. [iv](#)

- [28] C. Lin, S. Okamoto and A. J. Millis, *Dynamical mean-field study of model double-exchange superlattices*, *Phys. Rev. B* **73** (Jan, 2006) 041104. [iv](#)

- [29] C. Lin and A. J. Millis, *Theory of manganite superlattices*, *Phys. Rev. B* **78** (Nov, 2008) 184405. [iv](#)

- [30] B. R. K. Nanda and S. Satpathy, *Effects of strain on orbital ordering and magnetism at perovskite oxide interfaces: $LaMnO_3/SrMnO_3$* , *Phys. Rev. B* **78** (Aug, 2008) 054427. [iv](#), [8](#)

- [31] S. Dong, R. Yu, S. Yunoki, G. Alvarez, J.-M. Liu and E. Dagotto, *Magnetism, conductivity, and orbital order in $(LaMnO_3)_{2n}/(SrMnO_3)_n$ superlattices*, *Phys. Rev. B* **78** (Nov, 2008) 201102. [iv](#)

- [32] R. Yu, S. Yunoki, S. Dong and E. Dagotto, *Electronic and magnetic properties of $RMnO_3/AMnO_3$ heterostructures*, *Phys. Rev. B* **80** (Sep, 2009) 125115. [iv](#), [vii](#), [40](#), [41](#), [57](#), [77](#), [111](#)
- [33] C. Adamo, C. A. Perroni, V. Cataudella, G. De Filippis, P. Orgiani and L. Maritato, *Tuning the metal-insulator transitions of $(SrMnO_3)_n/(LaMnO_3)_{2n}$ superlattices: Role of interfaces*, *Phys. Rev. B* **79** (Jan, 2009) 045125. [iv](#)
- [34] K. Pradhan and A. P. Kampf, *Interfacial magnetism in manganite superlattices*, *Phys. Rev. B* **88** (Sep, 2013) 115136. [iv](#)
- [35] J. Salafranca, M. J. Calderón and L. Brey, *Magnetoresistance of an all-manganite spin valve: A thin antiferromagnetic insulator sandwiched between two ferromagnetic metallic electrodes*, *Phys. Rev. B* **77** (Jan, 2008) 014441. [iv](#)
- [36] D. Niebieskikwiat, L. E. Hueso, J. A. Borchers, N. D. Mathur and M. B. Salamon, *Nanoscale magnetic structure of ferromagnet/antiferromagnet manganite multilayers*, *Phys. Rev. Lett.* **99** (Dec, 2007) 247207. [iv](#)
- [37] S. Paul, R. Pankaj, S. Yarlagadda, P. Majumdar and P. B. Littlewood, *Giant magnetoelectric effect in pure manganite-manganite heterostructures*, *Phys. Rev. B* **96** (Nov, 2017) 195130. [v](#), [106](#), [111](#)
- [38] D. Khomskii, *Classifying multiferroics: Mechanisms and effects*, *Physics Online Journal* **2** (Mar, 2009) 20. [v](#), [37](#)
- [39] K. Wang, J.-M. Liu and Z. Ren, *Multiferroicity: the coupling between magnetic and polarization orders*, *Advances in Physics* **58** (2009) 321–448. [v](#), [37](#)

- [40] M. Fiebig and N. A. Spaldin, *Current trends of the magnetoelectric effect*, *The European Physical Journal B* **71** (Oct, 2009) 293. v, 37
- [41] P. Yu, Y.-H. Chu and R. Ramesh, *Oxide interfaces: pathways to novel phenomena*, *Materials Today* **15** (2012) 320–327. v, 37
- [42] S. Paul and S. Yarlagadda, *Study of the ferromagnetic-insulator phase in manganites*, [arXiv:1805.05172](#). vii, 111
- [43] V. Markovich, A. Wisniewski and H. Szymczak, *Chapter One - Magnetic Properties of Perovskite Manganites and Their Modifications*, vol. 22 of *Handbook of Magnetic Materials*. Elsevier, 2014, [10.1016/B978-0-444-63291-3.00001-5](#). vii, 108
- [44] P. Schiffer, A. P. Ramirez, W. Bao and S.-W. Cheong, *Low temperature magnetoresistance and the magnetic phase diagram of $La_{1-x}Ca_xMnO_3$* , *Phys. Rev. Lett.* **75** (Oct, 1995) 3336–3339. vii, 108
- [45] Venkateswara Pai, G., Hassan, S. R., Krishnamurthy, H. R. and Ramakrishnan, T. V., *Zero-temperature insulator-metal transition in doped manganites*, *Europhys. Lett.* **64** (2003) 696–702. vii, 39, 41, 43, 53, 83, 108
- [46] T. V. Ramakrishnan, H. R. Krishnamurthy, S. R. Hassan and G. V. Pai, *Theory of insulator metal transition and colossal magnetoresistance in doped manganites*, *Phys. Rev. Lett.* **92** (Apr, 2004) 157203. vii, 39, 41, 43, 53, 83, 108
- [47] M. Kagan, D. Khomskii and M. Mostovoy, *Double-exchange model: phase separation versus canted spins*, *The European Physical Journal B - Condensed Matter and Complex Systems* **12** (Nov, 1999) 217–223. viii, 31, 83, 108

- [48] S. Datta and S. Yarlagadda, *Quantum Phase Transition in the Holstein model*, *Proceedings of the DAE Solid State Physics Symposium (Golden Jubilee)* **50** (2005) 605. [viii](#), [108](#)
- [49] P. A. Kumar, R. Mathieu, P. Nordblad, S. Ray, O. Karis, G. Andersson et al., *Reentrant Superspin Glass Phase in a $\text{La}_{0.82}\text{Ca}_{0.18}\text{MnO}_3$ ferromagnetic insulator*, *Phys. Rev. X* **4** (Mar, 2014) 011037. [ix](#), [104](#), [109](#), [112](#)
- [50] J. G. Bednorz and K. A. Müller, *Perovskite-type oxides—the new approach to high- T_c superconductivity*, *Rev. Mod. Phys.* **60** (Jul, 1988) 585–600. [2](#)
- [51] J. Bardeen, L. N. Cooper and J. R. Schrieffer, *Theory of superconductivity*, *Phys. Rev.* **108** (Dec, 1957) 1175–1204. [2](#)
- [52] A. TARAPHDER, R. PANDIT, H. R. KRISHNAMURTHY and T. V. RAMAKRISHNAN, *The exotic barium bismuthates*, *International Journal of Modern Physics B* **10** (1996) 863–955. [2](#)
- [53] J. Shi, S. D. Ha, Y. Zhou, F. Schoofs and S. Ramanathan, *A correlated nickelate synaptic transistor*, *Nature Communications* **4** (Oct, 2013) 2676. [2](#)
- [54] K. Haule and G. L. Pascut, *Mott Transition and Magnetism in Rare Earth Nickelates and its Fingerprint on the X-ray Scattering*, *Scientific Reports* **7** (Sep, 2017) 10375. [2](#)
- [55] G. H. Kwei, A. C. Lawson, S. J. L. Billinge and S. W. Cheong, *Structures of the ferroelectric phases of barium titanate*, *J. Phys. Chem* **97** (Mar, 1993) 2368–2377. [2](#)

- [56] D. Hennings, *Barium titanate based ceramic materials for dielectric use*, *International Journal of High Technology Ceramics* **3** (1987) 91 – 111. 3
- [57] G. Thornton, F. C. Morrison, S. Partington, B. C. Tofield and D. E. Williams, *The rare earth cobaltates: localised or collective electron behaviour?*, *Journal of Physics C: Solid State Physics* **21** (1988) 2871. 3
- [58] Z. W. Li, Y. Drees, C. Y. Kuo, H. Guo, A. Ricci, D. Lamago et al., *Incommensurate spin correlations in highly oxidized cobaltates $La_{2-x}Sr_xCoO_4$* , *Scientific Reports* **6** (Apr, 2016) 25117. 3
- [59] P. Zubko, S. Gariglio, M. Gabay, P. Ghosez and J.-M. Triscone, *Interface physics in complex oxide heterostructures*, *Annual Review of Condensed Matter Physics* **2** (2011) 141–165. 3, 6
- [60] K. v. Klitzing, G. Dorda and M. Pepper, *New Method for High-Accuracy Determination of the Fine-Structure Constant Based on Quantized Hall Resistance*, *Phys. Rev. Lett.* **45** (Aug, 1980) 494–497. 3
- [61] D. C. Tsui, H. L. Stormer and A. C. Gossard, *Two-dimensional magnetotransport in the extreme quantum limit*, *Phys. Rev. Lett.* **48** (May, 1982) 1559–1562. 3
- [62] Y. K. Kato, R. C. Myers, A. C. Gossard and D. D. Awschalom, *Observation of the Spin Hall Effect in Semiconductors*, *Science* **306** (2004) 1910–1913. 3
- [63] C. H. Ahn, J.-M. Triscone and J. Mannhart, *Electric field effect in correlated oxide systems*, *Nature* **424** (Aug, 2003) 1015. 3

- [64] C. H. Ahn, A. Bhattacharya, M. Di Ventra, J. N. Eckstein, C. D. Frisbie, M. E. Gershenson et al., *Electrostatic modification of novel materials*, *Rev. Mod. Phys.* **78** (Nov, 2006) 1185–1212. [3](#)
- [65] M. Golalikhani, Q. Lei, R. U. Chandrasena, L. Kasaei, H. Park, J. Bai et al., *Nature of the metal-insulator transition in few-unit-cell-thick LaNiO_3 films*, *Nature Communications* **9** (Jun, 2018) 2206. [5](#)
- [66] D. I. Khomskii and K. I. Kugel, *Elastic interactions and superstructures in manganites and other Jahn-Teller systems*, *Phys. Rev. B* **67** (Apr, 2003) 134401. [5](#)
- [67] J. Liu, M. Kareev, B. Gray, J. W. Kim, P. Ryan, B. Dabrowski et al., *Strain-mediated metal-insulator transition in epitaxial ultrathin films of NdNiO_3* , *Applied Physics Letters* **96** (2010) 233110. [5](#)
- [68] J. Liu, M. Kargarian, M. Kareev, B. Gray, P. J. Ryan, A. Cruz et al., *Heterointerface engineered electronic and magnetic phases of NdNiO_3 thin films*, *Nature Communications* **4** (2010) 2714. [5](#)
- [69] J. Liu, M. Kareev, D. Meyers, B. Gray, P. Ryan, J. W. Freeland et al., *Metal-insulator transition and orbital reconstruction in mott-type quantum wells made of NdNiO_3* , *Phys. Rev. Lett.* **109** (Sep, 2012) 107402. [5](#)
- [70] N. B. Aetukuri, A. X. Gray, M. Drouard, M. Cossale, L. Gao, A. H. Reid et al., *Control of the metal - insulator transition in vanadium dioxide by modifying orbital occupancy*, *Nature Physics* **9** (Apr, 2006) 661. [5](#)

- [71] J. Chakhalian, J. W. Freeland, H.-U. Habermeier, G. Cristiani, G. Khaliullin, M. van Veenendaal et al., *Orbital reconstruction and covalent bonding at an oxide interface*, *Science* **318** (2007) 1114–1117. [5](#)
- [72] J. Chakhalian, J. W. Freeland, G. Srajer, J. Strempfer, G. Khaliullin, J. C. Cezar et al., *Magnetism at the interface between ferromagnetic and superconducting oxides*, *Nature Physics* **2** (Apr, 2006) 244. [5](#)
- [73] Z. Sefrioui, D. Arias, V. Peña, J. E. Villegas, M. Varela, P. Prieto et al., *Ferromagnetic/superconducting proximity effect in $\text{La}_{0.7}\text{Ca}_{0.3}\text{MnO}_3/\text{YBa}_2\text{Cu}_3\text{O}_{7-\delta}$ superlattices*, *Phys. Rev. B* **67** (Jun, 2003) 214511. [5](#)
- [74] T. Holden, H.-U. Habermeier, G. Cristiani, A. Golnik, A. Boris, A. Pimenov et al., *Proximity induced metal-insulator transition in $\text{YBa}_2\text{Cu}_3\text{O}_7/\text{La}_{2/3}\text{Ca}_{1/3}\text{MnO}_3$ superlattices*, *Phys. Rev. B* **69** (Feb, 2004) 064505. [5](#)
- [75] D. K. Satapathy, M. A. Uribe-Laverde, I. Marozau, V. K. Malik, S. Das, T. Wagner et al., *Magnetic proximity effect in $\text{YBa}_2\text{Cu}_3\text{O}_7/\text{La}_{2/3}\text{Ca}_{1/3}\text{MnO}_3$ and $\text{YBa}_2\text{Cu}_3\text{O}_7/\text{LaMnO}_{3+\delta}$ superlattices*, *Phys. Rev. Lett.* **108** (May, 2012) 197201. [5](#)
- [76] N. M. Nemes, M. García-Hernández, S. G. E. te Velthuis, A. Hoffmann, C. Visani, J. Garcia-Barriocanal et al., *Origin of the inverse spin-switch behavior in manganite/cuprate/manganite trilayers*, *Phys. Rev. B* **78** (Sep, 2008) 094515. [5](#)
- [77] A. Ohtomo and H. Y. Hwang, *A high-mobility electron gas at the $\text{LaAlO}_3/\text{SrTiO}_3$ heterointerface*, *Nature* **427** (Jan, 2004) 423. [6](#)

- [78] J. Mannhart and D. G. Schlom, *Oxide Interfaces—An Opportunity for Electronics*, *Science* **327** (2010) 1607–1611. 6
- [79] N. Reyren, S. Thiel, A. D. Caviglia, L. F. Kourkoutis, G. Hammerl, C. Richter et al., *Superconducting Interfaces Between Insulating Oxides*, *Science* **317** (2007) 1196–1199. 6
- [80] D. A. Dikin, M. Mehta, C. W. Bark, C. M. Folkman, C. B. Eom and V. Chandrasekhar, *Coexistence of superconductivity and ferromagnetism in two dimensions*, *Phys. Rev. Lett.* **107** (Jul, 2011) 056802. 6
- [81] L. Li, C. Richter, J. Mannhart and R. C. Ashoori, *Coexistence of magnetic order and two-dimensional superconductivity at $\text{LaAlO}_3/\text{SrTiO}_3$ interfaces*, *Nature Physics* **7** (Sep, 2011) 762. 6
- [82] K. S. Takahashi, M. Kawasaki and Y. Tokura, *Interface ferromagnetism in oxide superlattices of $\text{CaMnO}_3/\text{CaRuO}_3$* , *Applied Physics Letters* **79** (2001) 1324–1326. 6
- [83] J. W. Freeland, J. Chakhalian, A. V. Boris, J.-M. Tonnerre, J. J. Kavich, P. Yordanov et al., *Charge transport and magnetization profile at the interface between the correlated metal CaRuO_3 and the antiferromagnetic insulator CaMnO_3* , *Phys. Rev. B* **81** (Mar, 2010) 094414. 6
- [84] B. R. K. Nanda, S. Satpathy and M. S. Springborg, *Electron Leakage and Double-Exchange Ferromagnetism at the Interface between a Metal and an Antiferromagnetic Insulator: $\text{CaRuO}_3/\text{CaMnO}_3$* , *Phys. Rev. Lett.* **98** (May, 2007) 216804. 6

- [85] P. Moetakef, C. A. Jackson, J. Hwang, L. Balents, S. J. Allen and S. Stemmer, *Toward an artificial mott insulator: Correlations in confined high-density electron liquids in $SrTiO_3$* , *Phys. Rev. B* **86** (Nov, 2012) 201102. [7](#)
- [86] R. Chen, S. Lee and L. Balents, *Dimer mott insulator in an oxide heterostructure*, *Phys. Rev. B* **87** (Apr, 2013) 161119. [7](#)
- [87] A. Tsukazaki, A. Ohtomo, T. Kita, Y. Ohno, H. Ohno and M. Kawasaki, *Quantum Hall Effect in Polar Oxide Heterostructures*, *Science* **315** (2007) 1388–1391. [7](#)
- [88] A. Tsukazaki, S. Akasaka, K. Nakahara, Y. Ohno, H. Ohno, D. Maryenko et al., *Observation of the fractional quantum Hall effect in an oxide*, *Nature Materials* **9** (Oct, 2010) 889. [7](#)
- [89] D. G. Schlom and L. N. Pfeiffer, *Upward mobility rocks!*, *Nature Materials* **9** (Oct, 2010) 881. [7](#)
- [90] J. Chakhalian, J. W. Freeland, A. J. Millis, C. Panagopoulos and J. M. Rondinelli, *Colloquium: Emergent properties in plane view: Strong correlations at oxide interfaces*, *Rev. Mod. Phys.* **86** (Oct, 2014) 1189–1202. [7](#)
- [91] H. Yamada, M. Kawasaki, T. Lottermoser, T. Arima and Y. Tokura, *$LaMnO_3/SrMnO_3$ interfaces with coupled charge-spin-orbital modulation*, *Applied Physics Letters* **89** (2006) 052506. [8](#)
- [92] A. J. Millis, T. Darling and A. Migliori, *Quantifying strain dependence in “colossal” magnetoresistance manganites*, *Journal of Applied Physics* **83** (1998) 1588–1591. [8](#)

- [93] H. Yamada, Y. Ogawa, Y. Ishii, H. Sato, M. Kawasaki, H. Akoh et al., *Engineered interface of Magnetic Oxides*, *Science* **305** (2004) 646–648. 8
- [94] G. H. Jonker and J. H. Van Santen, *Ferromagnetic compounds of manganese with perovskite structure*, *Physica* **16** (Mar., 1950) 337–349. 8
- [95] J. H. Van Santen and G. H. Jonker, *Electrical conductivity of ferromagnetic compounds of manganese with perovskite structure*, *Physica* **16** (July, 1950) 599–600. 8
- [96] G. Jonker, *Magnetic compounds with perovskite structure IV Conducting and non-conducting compounds*, *Physica* **22** (1956) 707 – 722. 9
- [97] J. Volger, *Further experimental investigations on some ferromagnetic oxidic compounds of manganese with perovskite structure*, *Physica* **20** (1954) 49 – 66. 9
- [98] E. O. Wollan and W. C. Koehler, *Neutron diffraction study of the magnetic properties of the series of perovskite-type compounds $[(1 - x)\text{La}, x\text{Ca}]\text{MnO}_3$* , *Phys. Rev.* **100** (Oct, 1955) 545–563. 9
- [99] J. Z., V. S. and Z. J., *The magnetic structure of $\text{Pr}_{0.9}\text{Ca}_{0.1}\text{MnO}_3$* , *physica status solidi (a)* **52** K39–K43. 9
- [100] E. Pollert, S. Krupika and E. Kuzmiov, *Structural study of $\text{Pr}_{1-x}\text{Ca}_x\text{MnO}_3$ and $\text{Y}_{1-x}\text{Ca}_x\text{MnO}_3$ perovskites*, *Journal of Physics and Chemistry of Solids* **43** (1982) 1137 – 1145. 9
- [101] R. Kusters, J. Singleton, D. Keen, R. McGreevy and W. Hayes, *Magnetoresistance measurements on the magnetic semiconductor $\text{Nd}_{0.5}\text{Pb}_{0.5}\text{MnO}_3$* , *Physica B: Condensed Matter* **155** (1989) 362 – 365. 10

- [102] R. von Helmolt, J. Wecker, B. Holzapfel, L. Schultz and K. Samwer, *Giant negative magnetoresistance in perovskitelike $\text{La}_{2/3}\text{Ba}_{1/3}\text{MnO}_x$ ferromagnetic films*, *Phys. Rev. Lett.* **71** (Oct, 1993) 2331–2333. [10](#)
- [103] K. Chahara, T. Ohno, M. Kasai and Y. Kozono, *Magnetoresistance in magnetic manganese oxide with intrinsic antiferromagnetic spin structure*, *Applied Physics Letters* **63** (1993) 1990–1992. [10](#)
- [104] H. L. Ju, C. Kwon, Q. Li, R. L. Greene and T. Venkatesan, *Giant magnetoresistance in $\text{La}_{1-x}\text{Sr}_x\text{MnO}_z$ films near room temperature*, *Applied Physics Letters* **65** (1994) 2108–2110. [10](#)
- [105] S. Jin, T. H. Tiefel, M. McCormack, R. A. Fastnacht, R. Ramesh and L. H. Chen, *Thousandfold change in resistivity in magnetoresistive $\text{La} - \text{Ca} - \text{Mn} - \text{O}$ films*, *Science* **264** (1994) 413–415. [10](#)
- [106] G. C. Xiong, Q. Li, H. L. Ju, S. M. Bhagat, S. E. Lofland, R. L. Greene et al., *Giant magnetoresistive memory effect in $\text{Nd}_{0.7}\text{Sr}_{0.3}\text{MnO}_z$ films*, *Applied Physics Letters* **67** (1995) 3031–3033. [10](#)
- [107] E. Dagotto, *Nanoscale Phase separation and Colossal Magnetoresistance*, vol. 136 of *Springer Series in Solid-State Sciences*. Springer, Berlin, Heidelberg, 2003, <https://doi.org/10.1007/978-3-662-05244-0>. [11](#)
- [108] H. Jahn and E. Teller, *Stability of polyatomic molecules in degenerate electronic states - I—orbital degeneracy*, *Proceedings of the Royal Society of London A: Mathematical, Physical and Engineering Sciences* **161** (1937) 220–235. [16](#)

- [109] K. I. Kugel' and D. I. Khomski, *The Jahn-Teller effect and magnetism: transition metal compounds*, *Soviet Physics Uspekhi* **25** 231. 16
- [110] D. Khomskii and G. Sawatzky, *Interplay between spin, charge and orbital degrees of freedom in magnetic oxides*, *Solid State Communications* **102** (1997) 87 – 99. 16
- [111] C. Zener, *Interaction between the d shells in the transition metals*, *Phys. Rev.* **81** (Feb, 1951) 440–444. 18, 26
- [112] C. Zener, *Interaction between the d-shells in the transition metals. II. Ferromagnetic compounds of manganese with perovskite structure*, *Phys. Rev.* **82** (May, 1951) 403–405. 18
- [113] C. Zener, *Interaction between the d-shells in the transition metals. III. Calculation of the weiss factors in Fe, Co, and Ni*, *Phys. Rev.* **83** (Jul, 1951) 299–301. 18
- [114] P. W. Anderson and H. Hasegawa, *Considerations on Double Exchange*, *Phys. Rev.* **100** (Oct, 1955) 675–681. 19, 26
- [115] P. G. de Gennes, *Effects of Double Exchange in Magnetic Crystals*, *Phys. Rev.* **118** (Apr, 1960) 141–154. 19, 56, 86
- [116] P. W. Anderson, *New approach to the theory of superexchange interactions*, *Phys. Rev.* **115** (Jul, 1959) 2–13. 22
- [117] A. Altland and B. D. Simons, *Condensed Matter Field Theory*. Mar., 2010, 10.1017/CBO9780511789984. 23
- [118] N. Furukawa, *Transport properties of the kondo lattice model in the limit $s = \infty$ and $d = \infty$* , *Journal of the Physical Society of Japan* **63** (1994) 3214–3217. 26

- [119] A. J. Millis, P. B. Littlewood and B. I. Shraiman, *Double exchange alone does not explain the resistivity of $La_{1-x}Sr_xMnO_3$* , *Phys. Rev. Lett.* **74** (Jun, 1995) 5144–5147. 26, 82
- [120] M. J. Calderón, J. A. Vergés and L. Brey, *Conductance as a function of temperature in the double-exchange model*, *Phys. Rev. B* **59** (Feb, 1999) 4170–4175. 26
- [121] J. Kanamori, *Crystal distortion in magnetic compounds*, *Journal of Applied Physics* **31** (1960) S14–S23. 26
- [122] S. M. Dunaevskii, *Magnetic phase diagrams of manganites in the electron doping region*, *Physics of the Solid State* **46** (Feb, 2004) 193–212. 28
- [123] T. F. Seman, K. H. Ahn, T. Lookman, A. Saxena, A. R. Bishop and P. B. Littlewood, *Effects of rare-earth ion size on the stability of the coherent Jahn-Teller distortions in undoped perovskite manganites*, *Phys. Rev. B* **86** (Nov, 2012) 184106. 29, 39, 82, 108
- [124] T. Hotta, S. Yunoki, M. Mayr and E. Dagotto, *A-type antiferromagnetic and C-type orbital-ordered states in $LaMnO_3$ using cooperative Jahn-Teller phonons*, *Phys. Rev. B* **60** (Dec, 1999) R15009–R15012. 30
- [125] I. Dzyaloshinsky, *A thermodynamic theory of “weak” ferromagnetism of antiferromagnetics*, *Journal of Physics and Chemistry of Solids* **4** (1958) 241–255. 35
- [126] T. Moriya, *Anisotropic Superexchange Interaction and Weak Ferromagnetism*, *Phys. Rev.* **120** (Oct, 1960) 91–98. 35

- [127] D. Khomskii, *Multiferroics: Different ways to combine magnetism and ferroelectricity*, *Journal of Magnetism and Magnetic Materials* **306** (2006) 1–8. [36](#)
- [128] L. W. Martin, S. P. Crane, Y.-H. Chu, M. B. Holcomb, M. Gajek, M. Huijben et al., *Multiferroics and magnetoelectrics: thinfilms and nanostructures*, *Journal of Physics: Condensed Matter* **20** (2008) 434220. [37](#)
- [129] X. Huang and S. Dong, *Ferroelectric control of magnetism and transport in oxide heterostructures*, *Modern Physics Letters B* **28** (2014) 1430010. [37](#)
- [130] Rondinelli James M., Stengel Massimiliano and Spaldin Nicola A., *Carrier-mediated magnetoelectricity in complex oxide heterostructures*, *Nature Nanotechnology* **3** (dec, 2007) 46. [37](#)
- [131] M. K. Niranjan, J. D. Burton, J. P. Velev, S. S. Jaswal and E. Y. Tsymbal, *Magnetoelectric effect at the $SrRuO_3/BaTiO_3$ (001) interface: An ab initio study*, *Applied Physics Letters* **95** (2009) 052501. [37](#)
- [132] J. D. Burton and E. Y. Tsymbal, *Prediction of electrically induced magnetic reconstruction at the manganite/ferroelectric interface*, *Phys. Rev. B* **80** (Nov, 2009) 174406. [37](#)
- [133] G. G. Guzmán-Verri, R. T. Brierley and P. B. Littlewood, *Elastic interactions and control of the Mott transition*, *arXiv:1701.02318*. [39](#), [82](#)
- [134] N. N. Kovaleva, A. M. Oleś, A. M. Balbashov, A. Maljuk, D. N. Argyriou, G. Khaliullin et al., *Low-energy Mott-Hubbard excitations in $LaMnO_3$ probed by optical ellipsometry*, *Phys. Rev. B* **81** (Jun, 2010) 235130. [40](#), [53](#), [98](#)

- [135] S. Datta, A. Das and S. Yarlagadda, *Many-polaron effects in the Holstein model*, *Phys. Rev. B* **71** (Jun, 2005) 235118. 43
- [136] S. Reja, S. Yarlagadda and P. B. Littlewood, *Phase diagram of the one-dimensional Hubbard-Holstein model at quarter filling*, *Phys. Rev. B* **84** (Aug, 2011) 085127. 43
- [137] R. Pankaj and S. Yarlagadda, *Study of cooperative breathing-mode in molecular chains*, *Phys. Rev. B* **86** (Jul, 2012) 035453. 43, 56, 87
- [138] K. Hirota, N. Kaneko, A. Nishizawa and Y. Endoh, *Two-Dimensional Planar Ferromagnetic Coupling in LaMnO_3* , *Journal of the Physical Society of Japan* **65** (1996) 3736–3739. 53, 98
- [139] F. Moussa, M. Hennion, J. Rodriguez-Carvajal, H. Moudden, L. Pinsard and A. Revcolevschi, *Spin waves in the antiferromagnet perovskite LaMnO_3 : A neutron-scattering study*, *Phys. Rev. B* **54** (Dec, 1996) 15149–15155. 53, 98
- [140] G. Biotteau, M. Hennion, F. Moussa, J. Rodríguez-Carvajal, L. Pinsard, A. Revcolevschi et al., *Approach to the metal-insulator transition in $\text{La}_{1-x}\text{Ca}_x\text{MnO}_3$ ($0 < x < 0.2$) Magnetic inhomogeneity and spin- wave anomaly*, *Phys. Rev. B* **64** (Aug, 2001) 104421. 53, 98
- [141] G. V. Pai, S. R. Hassan, H. R. Krishnamurthy and T. V. Ramakrishnan, *Zero-temperature insulator-metal transition in doped manganites*, *EPL (Europhysics Letters)* **64** (2003) 696. 55, 56, 57, 79
- [142] T. V. Ramakrishnan, H. R. Krishnamurthy, S. R. Hassan and G. V. Pai, *Theory of insulator metal transition and colossal magnetoresistance in doped manganites*, *Phys. Rev. Lett.* **92** (Apr, 2004) 157203. 55, 56, 57, 79

- [143] Y. A. Izyumov and Y. N. Skryabin, *Double exchange model and the unique properties of the manganites*, *Physics-Uspekhi* **44** 109. 56, 86
- [144] P. W. Anderson, *New approach to the theory of superexchange interactions*, *Phys. Rev.* **115** (Jul, 1959) 2–13. 56, 95
- [145] S. Okamoto and A. J. Millis, *Theory of mott insulator–band insulator heterostructures*, *Phys. Rev. B* **70** (Aug, 2004) 075101. 59
- [146] S. Yunoki, A. Moreo, E. Dagotto, S. Okamoto, S. S. Kancharla and A. Fujimori, *Electron doping of cuprates via interfaces with manganites*, *Phys. Rev. B* **76** (Aug, 2007) 064532. 59
- [147] C. Herring, G. T. Rado and H. Suhl, *Magnetism*, vol. **IV**. Academic Press, New York London, 1966. 60
- [148] W.-G. Yin, D. Volja and W. Ku, *Orbital Ordering in LaMnO_3 : Electron-Electron versus Electron-Lattice Interactions*, *Phys. Rev. Lett.* **96** (Mar, 2006) 116405. 60
- [149] Z. Zhong and P. Hansmann, *Band alignment and charge transfer in complex oxide interfaces*, *Phys. Rev. X* **7** (Mar, 2017) 011023. 60
- [150] T. Wu, S. B. Ogale, J. E. Garrison, B. Nagaraj, A. Biswas, Z. Chen et al., *Electroresistance and Electronic Phase Separation in Mixed-Valent Manganites*, *Phys. Rev. Lett.* **86** (Jun, 2001) 5998–6001. 60
- [151] N. C. Bristowe, P. B. Littlewood and E. Artacho, *The net charge at interfaces between insulators*, *Journal of Physics: Condensed Matter* **23** (2011) 081001. 73
- [152] R. Pankaj and S. Yarlagadda, *Charge and orbital order due to cooperative Jahn-Teller effect in manganite chains*, *arXiv:1608.06055*. 80

- [153] D. I. Khomskii, *Role of Orbitals in the Physics of Correlated Electron Systems*, *Physica Scripta* **72** CC8. 81
- [154] T. Hotta, *Orbital ordering phenomena in d- and f-electron systems*, *Reports on Progress in Physics* **69** 2061. 81
- [155] S. Kumar and P. Majumdar, *Insulator-Metal Phase Diagram of the Optimally Doped Manganites from the Disordered Holstein-Double Exchange Model*, *Phys. Rev. Lett.* **96** (Jan, 2006) 016602. 82
- [156] A. Ghosh and S. Yarlagadda, *Study of long-range orders of hard-core bosons coupled to cooperative normal modes in two-dimensional lattices*, *Phys. Rev. B* **96** (Sep, 2017) 125108. 82, 86, 87, 88
- [157] P. Dai, J. A. Fernandez-Baca, E. W. Plummer, Y. Tomioka and Y. Tokura, *Magnetic coupling in the insulating and metallic ferromagnetic $La_{1-x}Ca_xMnO_3$* , *Phys. Rev. B* **64** (Nov, 2001) 224429. 82
- [158] P. Dai, J. A. Fernandez-Baca, N. Wakabayashi, E. W. Plummer, Y. Tomioka and Y. Tokura, *Short-Range Polaron Correlations in the Ferromagnetic $La_{1-x}Ca_xMnO_3$* , *Phys. Rev. Lett.* **85** (Sep, 2000) 2553–2556. 82
- [159] W. Jiang, X. Z. Zhou, G. Williams, R. Privezentsev and Y. Mukovskii, *Mechanisms underlying ferromagnetism across the metal-insulator transition in $La_{1-x}Ca_xMnO_3$* , *Phys. Rev. B* **79** (Jun, 2009) 214433. 82
- [160] V. Markovich, E. Rozenberg, A. I. Shames, G. Gorodetsky, I. Fita, K. Suzuki et al., *Magnetic, transport, and electron magnetic resonance properties of $La_{0.82}Ca_{0.18}MnO_3$ single crystals*, *Phys. Rev. B* **65** (Mar, 2002) 144402. 82

- [161] V. Markovich, I. Fita, R. Puzniak, M. I. Tsindlekht, A. Wisniewski and G. Gorodetsky, *Magnetization and ac susceptibility studies of the magnetic phase separation in $La_{0.8}Ca_{0.2}MnO_3$ and $La_{0.78}Ca_{0.22}MnO_3$ single crystals*, *Phys. Rev. B* **66** (Sep, 2002) 094409. [82](#)
- [162] A. Dey, M. Q. Lone and S. Yarlagadda, *Decoherence in models for hard-core bosons coupled to optical phonons*, *Phys. Rev. B* **92** (Sep, 2015) 094302. [87](#)
- [163] A. Efros, *Physics and Geometry of Disorder: Percolation Theory*. Science for everyone. Mir Publishers, 1986, [ark:/13960/t5w70635w](#). [108](#)
- [164] A. Urushibara, Y. Moritomo, T. Arima, A. Asamitsu, G. Kido and Y. Tokura, *Insulator-metal transition and giant magnetoresistance in $La_{1-x}Sr_xMnO_3$* , *Phys. Rev. B* **51** (May, 1995) 14103–14109. [109](#)